

Modeling Solar Eclipses at Extreme Ultra Violet Wavelengths and the Effects of Nonuniform Eclipse Shadow on the Ionosphere-Thermosphere system

Sebastijan Mrak¹, Qingyu Zhu², Yue Deng³, Ingolf Dammasch⁴, Marie Dominique⁵, Marc R. Hairston⁶, Yukitoshi (Toshi) Nishimura⁷, and Joshua L. Semeter⁷

¹University of Colorado boulder

²High Altitude Observatory, National Center of Atmospheric Research

³University of Texas at Arlington

⁴Royal Observatory of Belgium

⁵The Royal Observatory of Belgium

⁶University of Texas at Dallas

⁷Boston University

November 26, 2022

Abstract

The impacts of solar eclipses on the ionosphere-thermosphere system particularly the composition, density, and transport are studied using numerical simulation and subsequent model-data comparison. We introduce a model of a solar eclipse mask (shadow) at Extreme Ultra Violet (EUV) wavelengths that computes the corresponding shadowing as a function of space, time, and wavelength of the input solar image. The current model includes interfaces for Solar Dynamics Observatory (SDO) and Geostationary Operational Environmental Satellites (GOES) EUV telescopes providing solar images at nine different wavelengths. We show the significance of the EUV eclipse shadow spatial variability and that it varies significantly with wavelength owing to the highly variable solar coronal emissions. We demonstrate geometrical differences between the EUV eclipse shadow compared to a geometrically symmetric simplification revealing changes in occultation vary $\pm 20\%$. The EUV eclipse mask is validated with in-situ solar flux measurements by the PROBA2/LYRA instrument suite showing the model captures the morphology and amplitudes of transient variability while the modeled gradients are slower. The effects of spatially EUV eclipse masks are investigated with Global Ionosphere Thermosphere Model (GITM) for the 21 August 2017 eclipse. The results reveal that the modeled EUV eclipse mask, in comparison with the geometrically symmetric approximation, causes changes in the Total Electron Content (TEC) in order of $\pm 20\%$, 5-20% in F-region plasma drift, and 20-30% in F-region neutral winds.

Abstract

The impacts of solar eclipses on the ionosphere-thermosphere system particularly the composition, density, and transport are studied using numerical simulation and subsequent model-data comparison. We introduce a model of a solar eclipse mask (shadow) at Extreme Ultra Violet (EUV) wavelengths that computes the corresponding shadowing as a function of space, time, and wavelength of the input solar image. The current model includes interfaces for Solar Dynamics Observatory (SDO) and Geostationary Operational Environmental Satellites (GOES) EUV telescopes providing solar images at nine different wavelengths. We show the significance of the EUV eclipse shadow spatial variability and that it varies significantly with wavelength owing to the highly variable solar coronal emissions. We demonstrate geometrical differences between the EUV eclipse shadow compared to a geometrically symmetric simplification revealing changes in occultation vary $\pm 20\%$. The EUV eclipse mask is validated with in-situ solar flux measurements by the PROBA2/LYRA instrument suite showing the model captures the morphology and amplitudes of transient variability while the modeled gradients are slower. The effects of spatially EUV eclipse masks are investigated with Global Ionosphere Thermosphere Model (GITM) for the 21 August 2017 eclipse. The results reveal that the modeled EUV eclipse mask, in comparison with the geometrically symmetric approximation, causes changes in the Total Electron Content (TEC) in order of $\pm 20\%$, 5-20% in F-region plasma drift, and 20-30% in F-region neutral winds.

Plain Language Summary

Solar eclipses perturb the upper atmosphere by cooling the region under the eclipse shadow due to abated solar irradiance and rarefy the Earth's ionosphere due to reduced photo-ionization under the eclipse's shadow. Solar eclipses are treated as natural laboratory experiments for ionospheric physics because of their predictive nature. Traditionally, the eclipse shadow has been modeled assuming both the Sun and the Moon are circular objects with the Sun being a uniform source of irradiance. This assumption is not correct because the ionosphere is produced by solar X-ray and EUV radiation which primarily originate in the highly variable solar corona. We introduce a model computing eclipse shadow at the EUV wavelength using high-resolution images of the solar corona. The model is validated using EUV irradiance observations from low earth orbit. The impacts of nonuniform EUV eclipse shadow are then investigated with a physics-based global ionosphere-thermosphere model (GITM).

1 Introduction

Solar eclipses have drawn a lot of interest in ionospheric research because they significantly alter the photochemical and transport processes due to the abatement of solar X-ray and Extreme Ultra Violet (EUV) flux within the eclipse's shadow (penumbra). Observations provide exceptional opportunities for testing global models of the ionosphere-thermosphere (I-T) because numerical simulations can be done in advance by virtue of knowing eclipses' timing, duration, location, and magnitude centuries ahead, making eclipses natural experiments. However, the laboratory experiment notion proved very challenging as nicely summarized by Rishbeth (1968): "The ionospheric physicist might wish that the Sun could be regarded as a constant, uniform source of ionizing radiation; but investigations of the Sun show that it is not." The solar corona, the source of the ionizing X-ray and EUV flux is considerably larger than the photosphere, therefore there exist no total solar eclipses for the I-T. Additionally, the solar corona is a spatially non-uniform source of X-ray and EUV radiation with localized regions of intense irradiance (solar active regions) and regions emanating low fluxes (coronal holes).

Even during a maximum eclipse about 10% of the total EUV flux reaches the thermosphere due to intense radiation sources located near the solar limbs (Rishbeth, 1968).

This residual flux was measured by in-situ rockets (Smith et al., 1965), and estimated from E-region density reduction during eclipses using ionosonde measurements of peak E-region electron density (NmE) (Nestorov & Taubenheim, 1962; Taubenheim & Serafimov, 1969; Marriott et al., 1972). Modeling of I-T responses to solar eclipses encompasses the estimation of eclipse penumbra, which is estimated assuming geometrically symmetric celestial bodies with a chosen maximum eclipse occultation factor (EOF) to reflect the residual EUV flux (Deehr & Rees, 1964; E. C. Ridley et al., 1984; Le et al., 2008; Wu et al., 2018; Lin et al., 2018; Bravo et al., 2020). Recently, the maximum EOF was estimated using a realistic EUV model, using images of the solar corona, to obtain an appropriate scaling factor inflating the solar radius using Solar and Heliospheric Observatory (SOHO) Extreme-ultraviolet Imaging Telescope (EIT) (Davis et al., 2000) and Solar Dynamics Observatory (SDO) Atmospheric Imaging Assembly (AIA) (Huba & Drob, 2017; McInerney et al., 2018; Harding et al., 2018).

The non-uniform corona causes transient gradients within the eclipse shadow that were measured in the NmE time-series profiles and attributed to covering and uncovering of solar active regions (Nestorov & Taubenheim, 1962; Rishbeth, 1968; Marriott et al., 1971; Davis et al., 2000). Marriott et al. (1972) utilized NmE-derived EOF from 4 spatially separated ionosondes to reconstruct the positions of solar active regions in solar corona with great success. The covering and uncovering of solar active regions were identified as a salient density perturbation measured by Global Positioning System (GPS) estimated Total Electron Content (TEC) during the 21 August 2017 eclipse (Mrak et al., 2018). The authors showed four large-scale crescent-shaped TEC perturbations that were co-linear with computed spatial gradients in EUV penumbra unambiguously proving the TEC perturbations were due to modulation of the ionospheric production function. Furthermore, measurements on board the Defense Meteorological Spacecraft Program (DMSP) measured transient fluctuations of electron temperature and ion drifts when traversing the regions of steep EUV gradients (Hairston et al., 2018).

We utilize a 4-D (space and time) model of solar eclipse shadow computed from images of the Sun taken by SDO-AIA and GOES-R Solar Ultra Violet Imager (SUVI) telescopes. The model computes EOF as a function of geographic position (latitude, longitude, altitude) and universal time (UT) at a given wavelength specified by the telescope channel. The proof of concept was demonstrated for the 21 August 2017 eclipse using SDO AIA (Huba & Drob, 2017; Mrak et al., 2018; Hairston et al., 2018) in conjunction with Naval Observatory Vector Astrometry Software (NOVAS) (Kaplan et al., 2011). Here we introduce an updated model of eclipse penumbra that works with SDO AIA, Geostationary Operational Environmental Satellites (GOES)-R SUVI, and SOHO EIT images, computing EOFs based on the pyEphem (<https://pypi.org/project/ephem/>) library with a purely *Pythonic* software framework. The ramifications of using a realistic EUV model of penumbra on the I-T response are modeled with Global Ionosphere Thermosphere Model (GITM). We describe major differences of EUV penumbras compared to the GEO simplification, we validate the computed occultations with in-situ EUV flux measurements and quantify their impacts on the I-T response using GITM.

2 PyEclipse: A computational model of solar eclipses

High-resolution and high-fidelity images of coronal emissions are readily available since the operation of SDO AIA began in May 2010. The SDO AIA provides (4096 x 4096 pixels) images of solar emissions at seven EUV wavelengths (9.4 nm, 13.1 nm, 17.1 nm, 19.3 nm, 21.1 nm, 30.4 nm, and 33.5 nm) at sub-minute resolution per wavelength (Lemen et al., 2012). Another space-based EUV solar telescope is on-board GOES-R series satellites 16 and 17 providing EUV images at 6 EUV wavelengths with the SUVI (9.4 nm, 13.1 nm, 17.1 nm, 19.5 nm, 28.4 nm, and 30.4 nm) with data available since 2016 (GOES-R 16) and 2018 (GOES-R 17) (Darnel et al., 2022). The SUVI images have a resolution of 1280 x 1280 pixels with a 4-minute cadence. GOES-SUVI images have to be taken in

123 as a level-2 data product to avoid noisy background. Solar EUV images before 2010 are
 124 available from the SOHO EIT dating back to 1996. SOHO EIT images have a consid-
 125 erably lower dynamic range compared to AIA or SUVI, so we do not use the images in
 126 this report. The model interfaces with EIT, but additional image processing is neces-
 127 sary to obtain science-grade eclipse penumbra. We access level-1 AIA and EIT data through
 128 the Virtual Solar Observatory (VSO) using `sunpy` (Barnes et al., 2020), while SUVI data
 129 is obtained from National Centers for Environmental Information (NCEI) database. In
 130 general, `PyEclipse` can process any image of the Sun in Flexible Image Transport Sys-
 131 tem (FITS) format with metadata providing the position of the center of the Sun (in pixel
 132 units), a factor converting pixels to arcseconds in both dimensions, and an angular devi-
 133 ation of the Sun’s north pole from the vertical axis.

134 We developed the `PyEclipse` model based around `pyEphem` library. We compute
 135 the positions of the Sun and the Moon using `pyEphem` library that parses astronomical
 136 ephemeris with `XEphem` wrapper. The wrapper returns the positions of the Sun and the
 137 Moon relative to the observer in Topographic coordinates: the right ascension and decli-
 138 nation, and azimuth Φ and elevation ϵ angles. The latter has the same meaning as the
 139 former but is defined relative to the observer’s horizon. We compute the radial distance
 140 between the two bodies using the law of the great circle distance d :

$$d = 2 \arcsin \left(\left[\sin^2 \left(\frac{\Phi_S - \Phi_M}{2} \right) + \cos(\Phi_S) \cos(\Phi_M) \sin^2 \left(\frac{\epsilon_S - \epsilon_M}{2} \right) \right]^{\frac{1}{2}} \right) \quad (1)$$

141 where subscripts S and M denote the Sun and the Moon, respectively. The bearing angle
 142 α between the two objects defined as a clockwise angle from North to East is defined
 143 as:

$$\alpha = \arctan \left(\frac{\sin(\Phi_M - \Phi_S) \cos(\Phi_M - \Phi_S)}{\cos \epsilon_M \cos \epsilon_S - \cos \epsilon_M \sin \epsilon_S \cos(\Phi_M - \Phi_S)} \right) \quad (2)$$

144 For the EUV eclipse occultations using AIA/SUVI/EIT images, we convert the Moon’s
 145 relative position to the Sun (d, α) into the units of pixels using a constant provided by
 146 the EUV image metadata. Lastly, the Sun is rotated for the parallactic angle η based
 147 on the observer’s local time, and geographic location. The parallactic angle adjusts the
 148 position of the apparent Sun’s north pole to the direction of the observed zenith located
 149 in the northern hemisphere (Meadows, 2007):

$$\cos(\eta) = \frac{\sin(glat) - \sin(\delta) \cos(90 - \epsilon_S)}{\cos(\delta) \sin(90 - \epsilon_S)} \quad (3)$$

150 where $glat$ is geographic latitude, and δ is solar declination angle. The local time, ge-
 151 ographic location, and seasonal dependence on the parallactic angle are described in Ap-
 152 pendix Appendix A.

153 We compute the Eclipse Occultation Factor (EOF) as

$$EOF = \frac{\sum_i N_i}{\sum_i M_i} \quad (4)$$

154 where i is the pixel number, N is the occulted (masked) image, and M is the unocculted
 155 (only the Sun) image. EOF is always less or equal to 1, where the unity denotes no eclipse,
 156 and zero is a total eclipse. For the geometrically symmetric eclipse, we compute the EOF
 157 as:

$$EOF = 1 - \frac{A}{\pi(\lambda_S r_S)^2} \quad (5)$$

158 where A is the surface area of the overlapping circles (the Sun and the Moon), with the
 159 derivation in Appendix B. The denominator is the area of the Sun, where λ_S is the so-
 160 lar radius inflating factor.

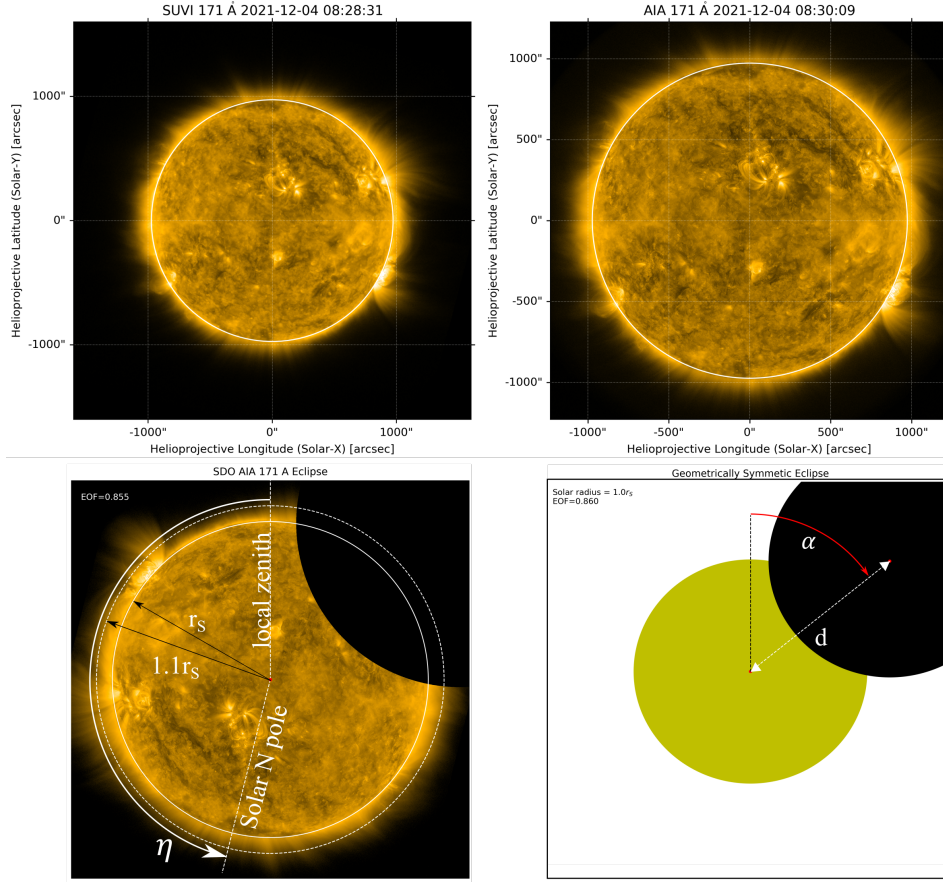


Figure 1. (top) Visualization of the Solar images used to compute high fidelity EUV eclipse using GOES SUVI (left) and SDO AIA (right) during the 4 December 2021 solar eclipse. (bottom) Illustration of eclipse occultation factor (EOF) computation and the depiction of parameters used for the calculations. (left) EOF using SDO AIA 17.1 nm image, rotated for the parallactic angle η . (right) Geometrically symmetric EOF using the distance d , bearing angle α , and the solar radius inflating factor $\lambda_S = 1.1$. The bottom row EOFs were computed from Jang Bogo station in Antarctica (164°E , 74°S).

161 The chief parameters and the illustration of the input solar images used by the PyE-
 162 clipse to compute the EOFs are depicted in Figure 1. This figure shows the GOES SUVI
 163 and SDO AIA images at 17.1 nm wavelength during the 4 December 2021 polar solar
 164 eclipse. Note, that the axes are converted from pixel counts into angular units of arc-
 165 seconds using the conversion factor provided by the metadata. The white fiducial line
 166 depicts the classical solar radius $r_S = 695,700$ kilometers, which is the radius of the pho-
 167 tosphere. The bottom panels depict a computation of the EOF using a EUV image (left)
 168 and the geometrically symmetric configuration (GEO) of the Sun and the Moon (right).
 169 The SDO AIA image is first rotated for the parallactic angle η , then the image is masked
 170 by the Moon. This panel indicates the classical solar radius (thick white line) and an ap-
 171 proximation of the $\sim 10\%$ wider EUV radius (depending on the solar activity), which cor-
 172 responds to the 1,000,000 degrees Kelvin solar corona. Note that the parallactic angle
 173 is close to 180 degrees because this was computed at a location in Antarctica (Jang Bogo
 174 station), where the observer’s zenith is closely aligned to the Sun’s south pole. The bot-

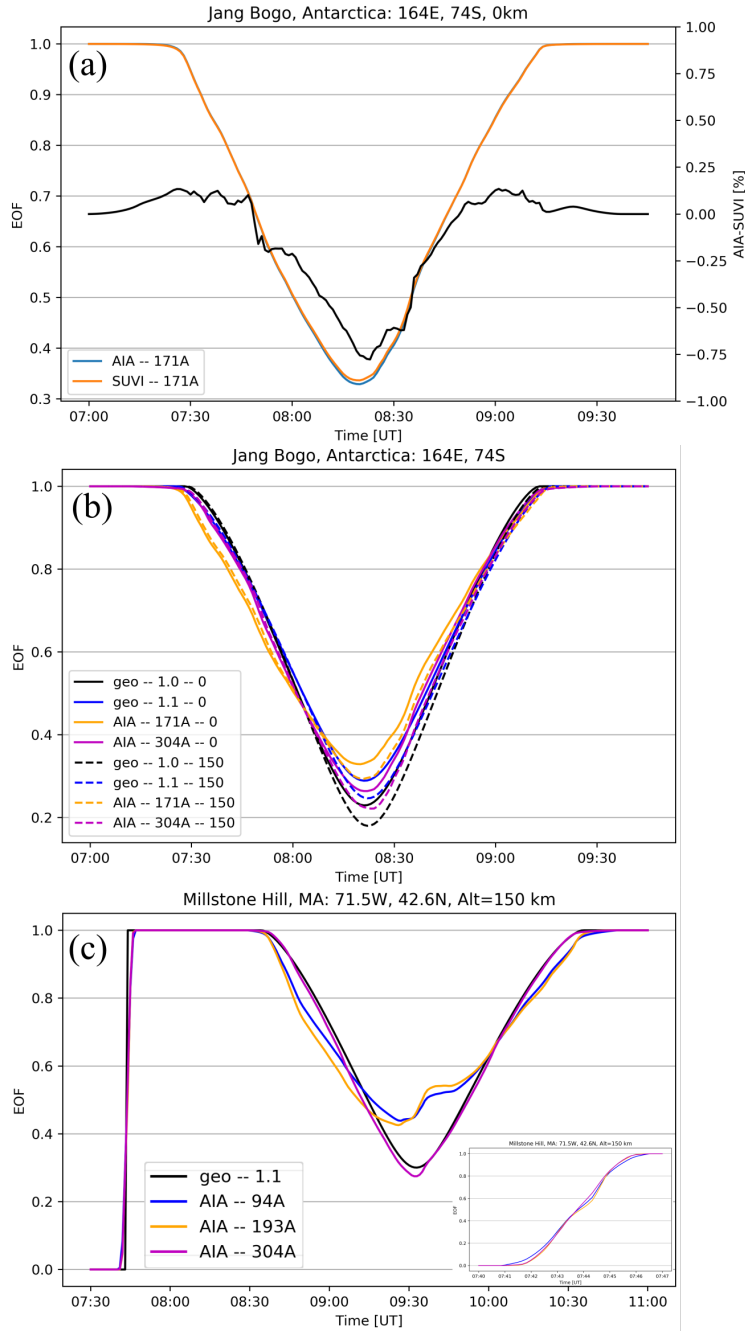


Figure 2. Eclipse Occultation Factors (EOFs) computed using PyEclipse for two eclipses and for a fixed geographic location. (a) EOFs during the 4 December 2021 eclipse are based on SDO AIA (blue) and GOES SUVI (orange) EUV images at 17.1 nm. The black line is the relative difference between the two EOFs. (b) EOFs during the 4 December 2021 eclipse corresponding to different wavelengths and solar radii at two altitudes (solid vs. broken lines). (c) EOFs for the 10 June 2021 eclipse near sunrise, illustrating the horizon effect (zoomed in the bottom right part of the figure) and the wavelength dependence.

175
176

tom right panel depicts the positions of the eclipsed bodies and the parameters α , and d used to compute the EOF.

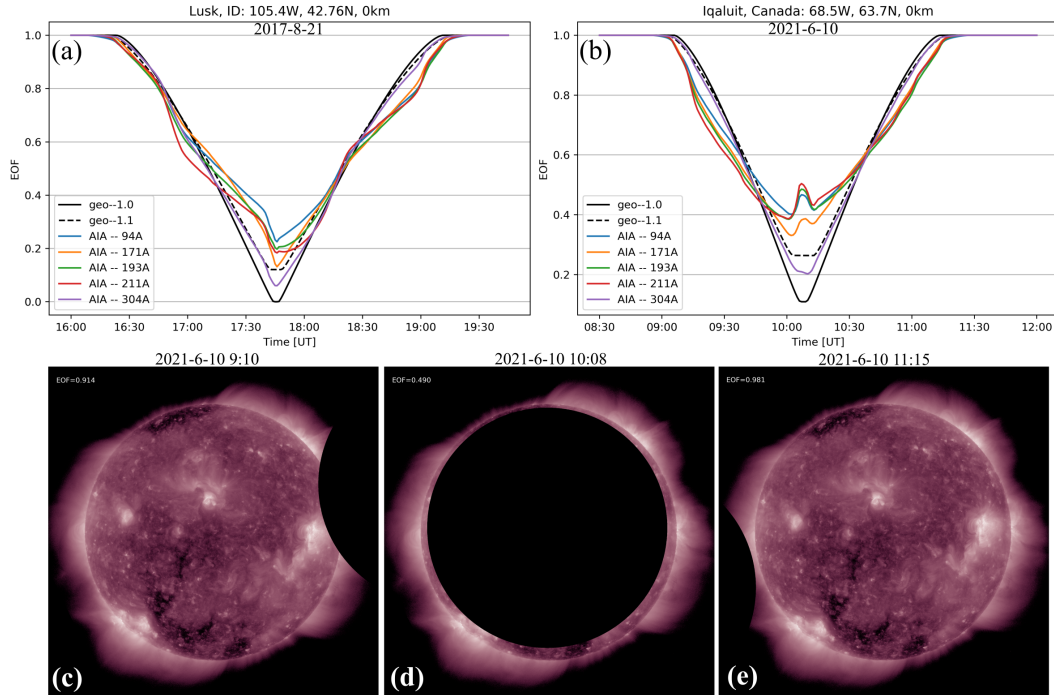


Figure 3. (a–b) Wavelength dependence and the consequences of solar active regions on the EOF. (a) EOFs from SDO AIA EUV telescopes and uniform geometrical eclipses (GEO) at two solar radii during the 21 August 2017 eclipse in Lusk, Idaho. (b) The same as in (a) but for the 10 June 2021 eclipse from Iqaluit, Canada. (c–e) Computed images of the solar eclipse using 21.1 nm SDO AIA telescope at three epochs from the location with depicted EOFs in panel (b).

177 Examples of EOFs computed by the PyEclipse model are depicted in Figure 2. The
 178 top panel (a) depicts the computed EOF at 17.1 nm wavelength for the Jang Bogo Antarc-
 179 tic station for the 4 December 2021 polar eclipse. The orange and blue time-series traces
 180 were computed using GOES-SUVI and SDO-AIA images, respectively. The black line
 181 represents the relative difference between both time-series. The difference never exceeds
 182 1%. The middle panel (b) depicts the wavelength and altitude dependence at the same
 183 geographic (longitude/latitude) location. Solid lines are EOFs computed for different wave-
 184 lengths and a uniform solar radius at the ground level, and the broken lines depict the
 185 corresponding EOFs at 150 km altitude. This particular example shows that, at this lo-
 186 cation, the maximum EOF was smaller at 150 km (greater eclipse), but this does not im-
 187 ply the general pattern. The height dependence is well known due to the solar zenith
 188 angle dependence (T. G. W. Verhulst & Stankov, 2020), and it depends on the relative
 189 position of the observer. This panel furthermore illustrates the wavelength dependence
 190 of the EOF, which was evident even during a solar minimum. The difference in solar radii
 191 between different EUV wavelengths is normally of the order of 10%. Lastly, the PyE-
 192 clipse is computing the position of the horizon, which is superposed on the normal eclipse
 193 mask if the horizon and the solar eclipse are simultaneously in the field of view. Figure 2c
 194 shows the continuous horizon (sunrise) just prior to an arriving eclipse and its wavelength
 195 dependence, as observed from the Millstone Hill Observatory during the 10 June 2021
 196 eclipse.

3 Spatiotemporal variability of the EUV penumbra

Figure 2c image depicts anomalous wavelength-dependent EOF variability near the anticipated maximum eclipse (minimum EOF). The sudden changes in the EOF, which are also visible in Figure 4, are due to covering and uncovering solar active regions. The example from 21 August 2017, was discussed by Mrak et al. (2018) in detail. They have shown that the transient fluctuations of the EOF resulting from covering and uncovering the active region cause large-scale effects that are clearly visible in the GPS-TEC maps. The actual EOF values are highly wavelength dependent as depicted in Figure 3a, with variations exceeding 15% at the most dramatic point just before the maximum eclipse owing to a solar active region at the limb of the Sun (Mrak et al., 2018). Figure 3b shows a wavelength-dependent sudden increase in the order of 5-10%, at a place one expects the maximum eclipse. This is explained in the reconstructed eclipse images in Figure 3c–e. This eclipse took place during the time that the solar EUV emissions predominantly originated in the regions near the solar limb. The sequence of three images shows that during the first half of the eclipse, the main source of the EUV (originated near the western limb) was constantly occulted (panel c). During the time that the Moon covered the biggest area of the Sun (panel d), both limbs were uncovered causing an actual increase in the solar EUV flux. During the second part of the eclipse, when the Moon was transitioning away, the Moon occulted the eastern limb causing the initial decrease in the EOF before it uncovered a sufficient area of the Sun for the EOF to recover.

Time-series line plots in Figure 2b-c and Figure 3a-b furthermore depict the differences between the EOFs computed using the simple geometric (GEO) consideration and the actual eclipse at EUV wavelengths. We already demonstrated that the solar corona extends approximately 10% beyond the standard solar radius. Therefore, the difference in the minimum EOFs (i.e., maximum eclipse) between the EUV EOF and a GEO EOF computed using the standard solar radius (denoted as GEO 1.0) is expected. While the increase in the effective solar radius causes a larger minimum EOF, it might also distort the EOF profile in the vicinity of the maximum eclipse as depicted in Figures 3a-b in black-dashed lines. The radius inflation causes the EOF to flatten over a period of several minutes. This causes an artificially high impact on the ionospheric density reduction as explained in section 5.4. The paradigm of assuming solar eclipses as spherically symmetric and occultation masks with a pre-defined minimum occultation in the order of 10% was established in the 1960s (Rishbeth, 1968). This consideration has persisted until the present day, as eclipse occultation models are still commonly computed assuming geometrically symmetrical celestial bodies.

Another pin-hole projection example occurs when a relatively strong solar active region (compared to the surrounding area) is located on a limb. That solar active region creates a transient perturbation near local noon, at the edge of the penumbra where the Moon skims only over the edges of the solar corona. This effect is presented in Figure 4 time-series accompanied by a sequence of reconstructed images of the eclipse using the SDO AIA telescope. The time series in Figure 4a shows a sudden, wavelength-dependent, drop in the EOF at around 18:45 UT, which lasted just 5 minutes. The total drop was the biggest at 19.3 nm wavelength, reaching $\sim 12\%$ below the baseline set by the 10% inflated GEO mask. The reconstructed eclipse images in panels b–e show the source of this depletion was a sudden occultation of one solar active region located on the limb. The Sun is rotated by the parallactic angle.

The importance of accurate EUV eclipse modeling at large scales is presented in 2D maps. Figure 5 shows geographic projections of two solar eclipse masks, 21 August 2017 in the top and 10 June 2021 in the bottom row, at one epoch computed using 10% inflated geometrically symmetric approximation (GEO 1.1 - left column), and 9.4 nm SDO AIA (middle column). The right column is the difference between the GEO and EUV masks. The difference maps show that (1) GEO approximation overestimates and underestimates by $\pm 15\text{-}25\%$ the EUV eclipse occultation depending on the position within

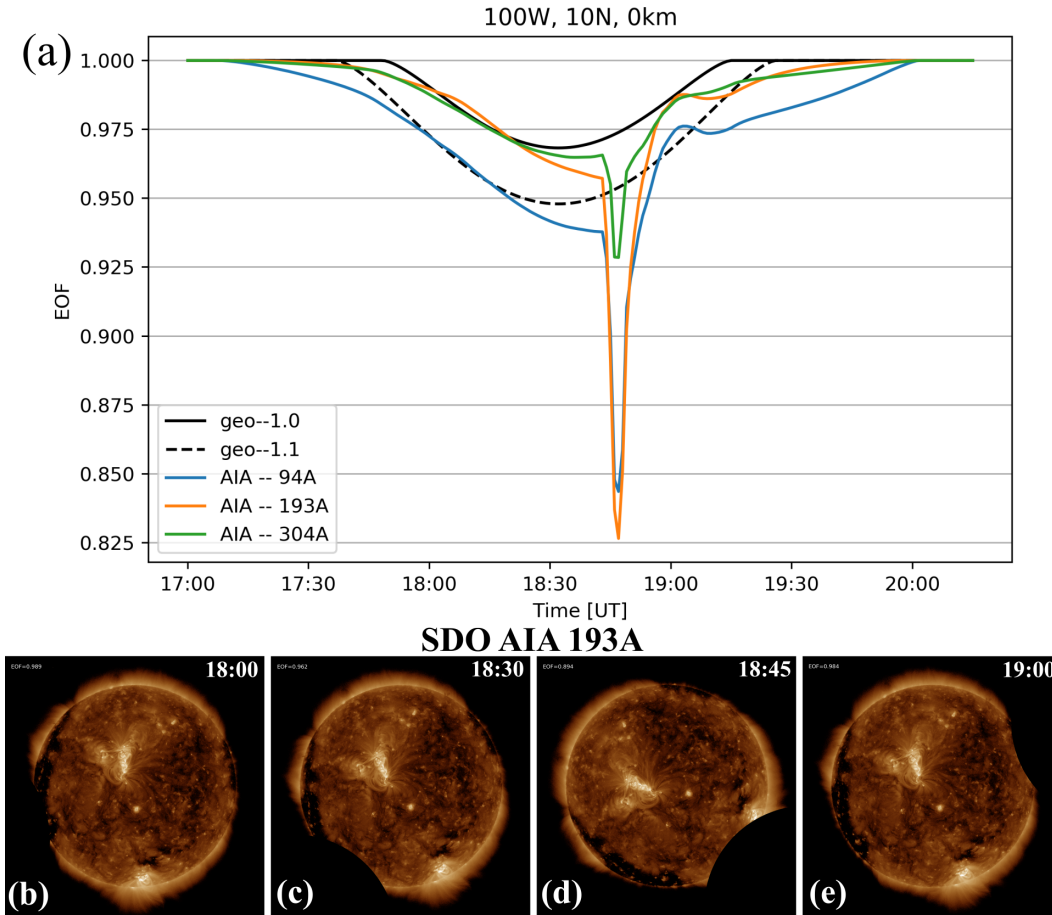


Figure 4. (Eclipse Occultation function (EOF) during the 21 August 2017 eclipse at 100°W , 10°N . (a) Shows EOF time-series at different wavelengths and 2 different solar radii factors. The EUV EOFs from SDO AIA images depict a transient reduction of EOF near 18:45 UT. (b–e) The sequence of reconstructed eclipse images shows the transition of the Moon skimming over one solar active region located on the solar limb.

250 the penumbra, (2) EUV masks feature regional transient feature discussed with Figure 4,
 251 and (3) the positions of the maximum eclipse (i.e., minimum EOF) differ and the dif-
 252 ference changes with time.

253 The solar eclipse mask varies in altitude as described in detail by T. G. W. Ver-
 254 hulst and Stankov (2020). We bolster their findings by expending the height dependence
 255 analysis using solar EUV emissions. Figure 6 shows the same eclipses and the exemplary
 256 eclipse masks as in Figure 5 in the latitude-altitude projection. The figure shows signif-
 257 icant position-dependent differences between the uniform and the EUV masks in the last
 258 column. The differences in the order of $\pm 15\%$ alternate as a function of latitude every
 259 5-10 degrees (i.e., 500 - 1,000 km). The 10 June 2021 eclipse EUV panel in Figure 6e shows
 260 the altitude-dependent projection of solar active regions near 60°N which was identified
 261 in Figures 3, and 5e-f. The altitude dependence, especially for eclipses similar to the 10
 262 June 2021 eclipse mask emphasizes the importance of using a 3-D eclipse mask in global
 263 modeling. However, the latter task is not trivial because the eclipse masks are specified
 264 at the upper boundary conditions together with the incoming EUV irradiance flux in a
 265 global circulation model. This also raises the question of what is the most appropriate

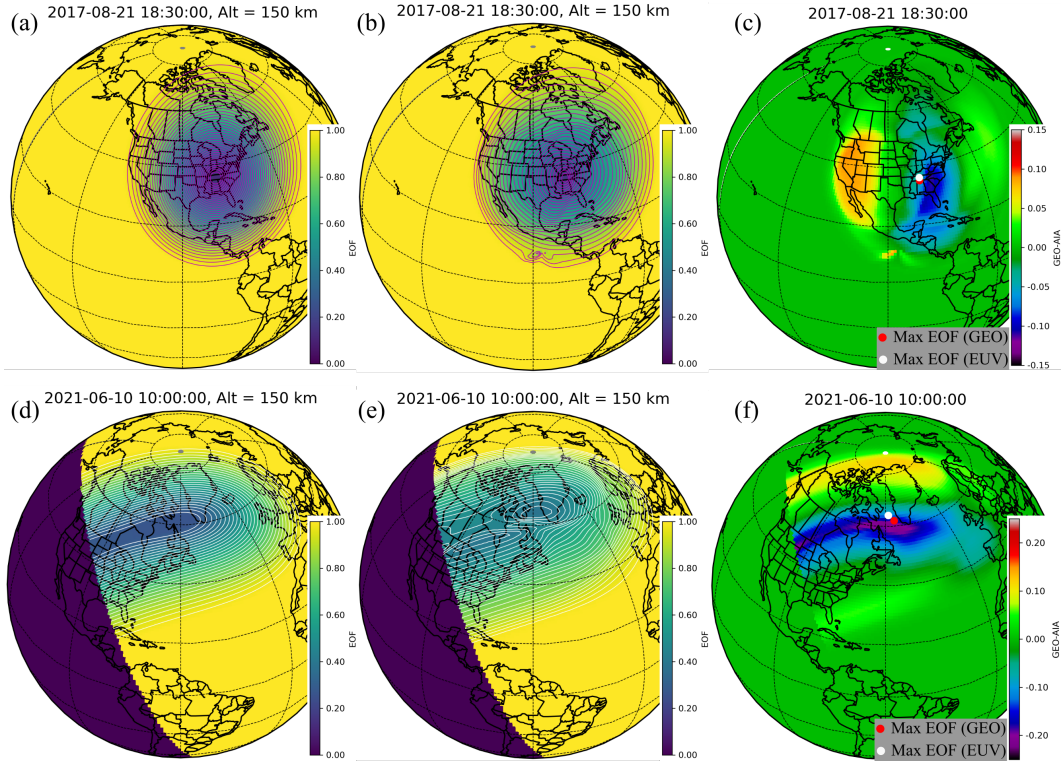


Figure 5. 2-dimensional latitude-longitude eclipse masks for two eclipses (top/bottom columns). (a–c) 21 August 2017 eclipse masks at 18:30 UT: (a) uniform mask with 10% inflated solar radii (GEO 1.1), (b) EUV mask using 9.4 nm SDO AIA image, (c) difference between (a) and (b). (d–f) 10 June 2021 eclipse masks at 10:00 UT: Rows are in the same format as the top panel. Different contour colors are for improving contrast and highlight the different features. Red/White dots in panels c and f the last row denote the maximum eclipse (minimum EOF) of the GEO and EUV masks, respectively.

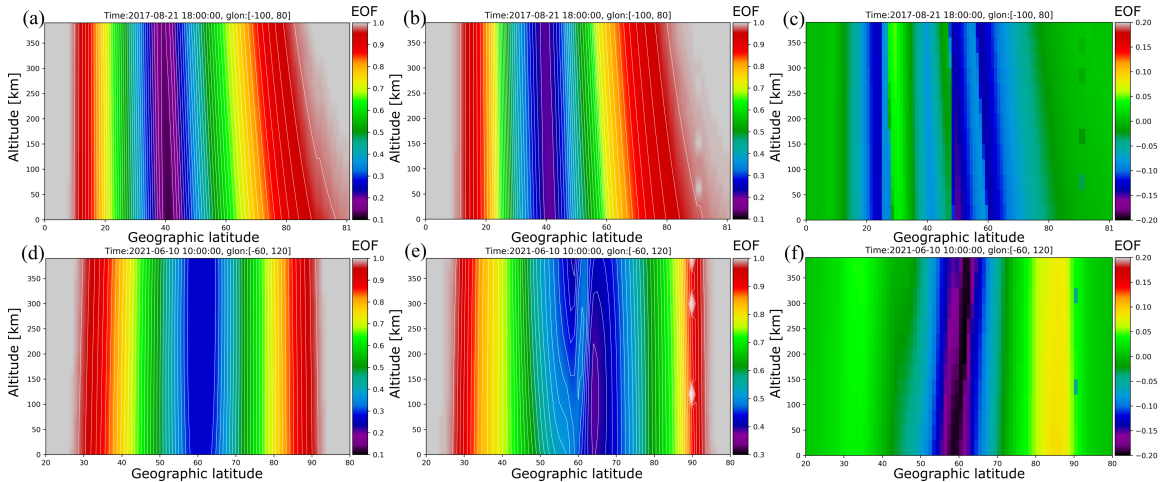


Figure 6. 2-dimensional latitude-altitude eclipse masks in the same format as for the eclipse from in Figure 5).

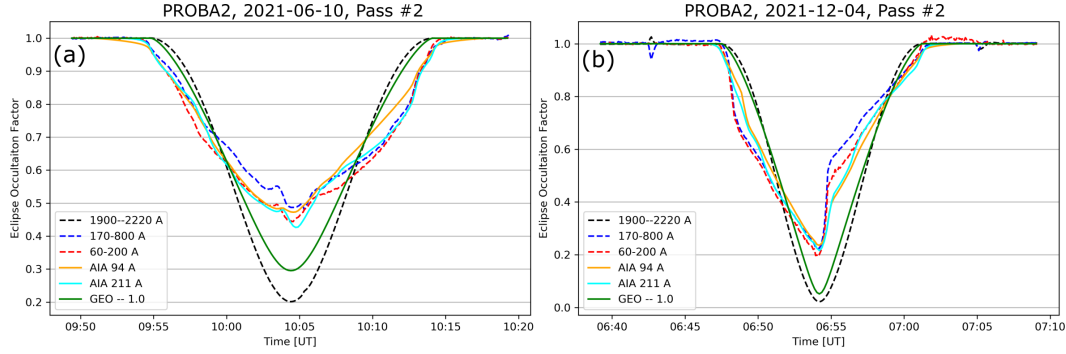


Figure 7. PROBA2/LYRA observations of the relative decrease in irradiance flux (dashed lines) compared to the PyEclipse model (solid lines) during one pass through the 10 June 2021 (a), and 4 December 2021 (b) eclipse. Colors represent three different LYRA wavelength bands (channels): (blue) LYRA 6-20 nm, (red) LYRA 17-80, and (black) LYRA 190-220 nm. Modeled EOFs were computed using PyEclipse wavelengths: (orange) SDO AIA 9.4 nm, (cyan) SDO AIA 21.1 nm, (black) GEO 1.0.

266 altitude for computing the 2D (lon/lat) eclipse mask knowing the systemic altitude-dependent
 267 trend (T. G. W. Verhulst & Stankov, 2020): at the E-region height where the impacts
 268 in plasma production and loss are the most significant, or at the height of the model's
 269 upper boundary condition?

270 4 Validation

271 We validate the PyEclipse EUV masks with direct measurements of solar irradiance
 272 using the Project for Onboard Autonomy 2 (PROBA2) Large Yield Radiometer
 273 (LYRA) (Dominique et al., 2013; BenMoussa et al., 2009). LYRA includes 4 photometers
 274 out of which we use 3: (1) 190-222 nm Herzberg continuum channel, (2) 17 - 80 nm
 275 + X-ray below 5 nm channel, and (3) 6 - 20 nm + X-ray below 2 nm. For this study,
 276 we used the data from the backup unit of LYRA (unit1), which is the least degraded.
 277 LYRA data were calibrated by subtracting dark currents for each channel. Then the data
 278 were decimated from the original 20 Hz to 2 Hz, and the irradiance flux was normalized
 279 by setting it to 1.0 adjacent to the eclipse transition. This procedure was applied in pre-
 280 vious studies (Stankov et al., 2017).

281 PROBA2 passed the 10 June 2021 and the 4 December 2021 eclipses three times
 282 with the second pass being the longest and at the highest solar zenith angle. We com-
 283 pare LYRA measurements taken from the second passes of each eclipse and converted
 284 them into eclipse occultation factors as described earlier. These observations are com-
 285 pared with the PyEclipse-modeled EOF at three wavelengths along the satellite trajec-
 286 tory. This comparison is presented in Figure 7. We use LYRA observations from the Herzberg
 287 continuum channel 1, X-ray+EUV channel 2, and X-ray+EUV channel 3. The modeled
 288 EOFs are computed using a geometrically symmetric mask with non-inflated solar radi-
 289 us (GEO 1.0), SDO AIA 9.4 nm, and SDO AIA 21.1 nm channels. All comparisons
 290 show the same trend and very similar maximum occultation. The difference in the max-
 291 imum occultation can be accounted for by virtue of using an arbitrary detrending of LYRA
 292 measurements, and a slightly different effective radius for the Herzberg continuum whose
 293 source region apparently dims toward the limb of the Sun causing a bigger maximum
 294 eclipse compared to the GEO 1.0 calculation. The only considerable difference is in the
 295 covering/uncovering of the solar active regions. While the model reproduces the timing
 296 and duration of the eclipse mask transients, the repose time is slower for both cases. This

297 can be explained by a couple of different factors: (1) The AIA images have finite spa-
 298 tial resolution and dynamic range smearing out sharp brightness transitions. (2) PyE-
 299 clipse model is purely geometric, it does not consider any diffraction of the Moon limb.
 300 (3) LYRA detectors are aging, even those on the backup unit, and are losing sensitiv-
 301 ity over time that might reflect sharper changes (BenMoussa et al., 2013). (4) The LYRA
 302 wavelength response is different from the SDO AIA narrowband telescopes, and LYRA
 303 is sensitive to soft X-ray bands while SDO AIA does not cover these wavelengths. In ag-
 304 gregate, the in-situ observations of abated solar irradiance are morphologically replicated
 305 by the PyEclipse model, the timing and duration of overall eclipse shadow as well as the
 306 transient perturbations are in agreement. If the model misses anything, then these are
 307 only very steep transitions which would lead to a slight underestimation of the modeled
 308 gradients using PyEclipse eclipse masks.

309 5 Modeling I-T response to the 21 August 2017 eclipse

310 The impact of a EUV (9.4 nm) eclipse mask compared to the uniform (GEO) eclipse
 311 mask on the I-T system was investigated using the Global Ionosphere Thermosphere Model
 312 (GITM) (A. Ridley et al., 2006). GITM is a 3D non-hydrostatic GCM that self-consistently
 313 solves the neutral and ion densities, composition, velocities, and temperatures on an ad-
 314 justable spatial and temporal resolution. GITM differs from other GCMs in that it can
 315 simulate the non-hydrostatic processes caused by the variation of energy inputs (Deng
 316 et al., 2008, 2011, 2021; Lin et al., 2017, 2018; Zhu et al., 2017). The electrodynamic solver
 317 in GITM used in this study is the NCAR 3D dynamo solver (Maute & Richmond, 2017)
 318 which was coupled by Zhu et al. (2019).

319 Three simulations are carried out: one is the controlled run where no eclipse mask
 320 is included; another two simulations are eclipse runs where the GEO and EUV eclipse
 321 masks are included. The way to introduce the time-evolving eclipse mask is similar to
 322 that in Lin et al. (2018) where the eclipse mask is spatiotemporally interpolated to the
 323 GITM grids and model running time during the simulation. Hence, an EOF can be ob-
 324 tained at a grid and a model running time which is then multiplied by the EUV flux,
 325 derived from the F10.7 on that day, to calculate the ionization and heating due to the
 326 EUV radiation using Torr et al. (1979). For all GITM runs, the spatial resolution is 2.5°
 327 in longitude, 1.25° in latitude, and $1/3$ scale height in altitude, the temporal resolution
 328 is 2s and the output cadence is 10 min. The high-latitude electric field and electron pre-
 329 cipitation are specified by the Auroral Spectrum and High Latitude Electric field vari-
 330 ability (ASHLEY, Zhu et al. (2021)) model, which is driven by the realistic interplan-
 331 etary magnetic field (IMF) and solar wind data. GITM has been used before to study
 332 the global response to the 2017 eclipse (Cnossen et al., 2019), model-data comparison
 333 (Wu et al., 2018), and to identify small-scale wave-like features (Lin et al., 2018). The
 334 exact comparison between the previous runs is not possible due to the simplified eclipse
 335 trajectory (Wu et al., 2018). We show only modeling results of the 21 August 2017 eclipse
 336 and compare them to observations in the literature to quantify the contribution of the
 337 EUV mask to the I-T response compared to the uniform eclipse assumption. Other eclipses
 338 discussed in the previous sections deserve separate model-data investigations because of
 339 the unique features associated with each eclipse.

340 5.1 Total Electron Content

341 We present the modeled GITM TEC response in Figure 8. In all GITM figures, the
 342 left column represents the difference between the GITM eclipse run using a 9.4 nm EUV
 343 mask and the baseline run without the eclipse (eclipse_euv - baseline). The right column
 344 is the contribution of the EUV variability demonstrated by the difference plots obtained
 345 by GITM eclipse runs using the EUV mask and a geometrically symmetric (GEO) ap-
 346 proximation with 10% inflated solar radius (eclipse_euv - eclipse_geo). First, the GITM

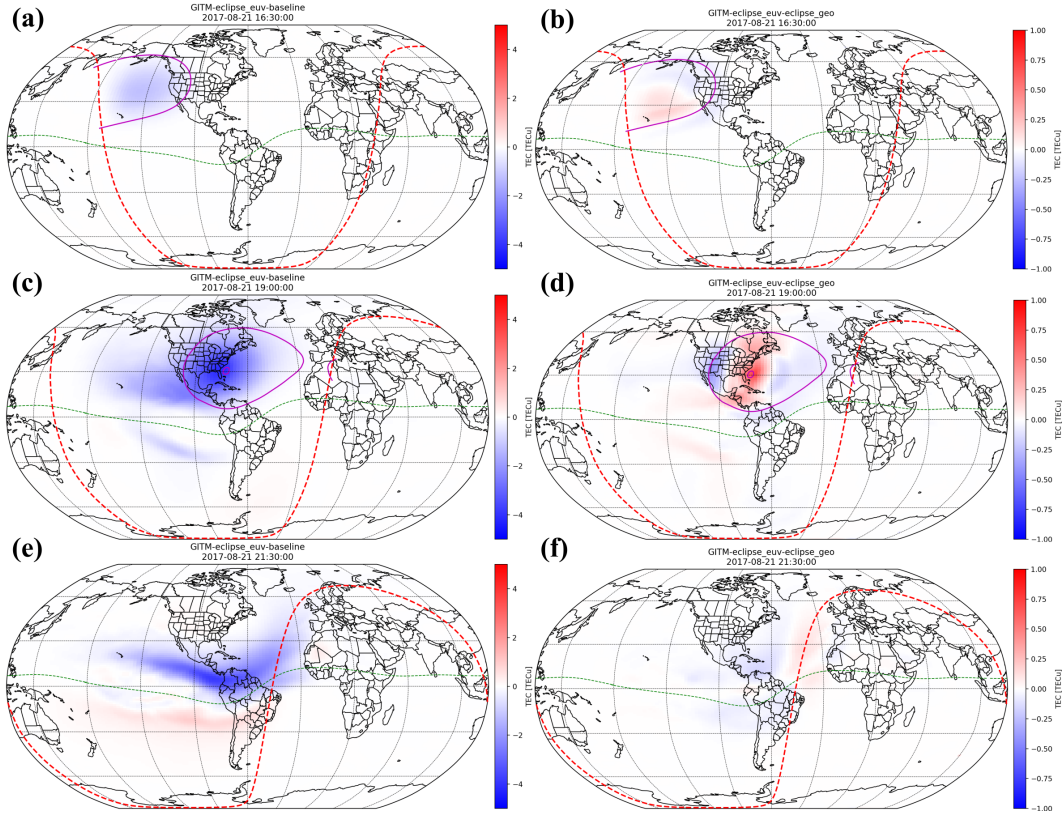


Figure 8. GITM modeled TEC during the 21 August 2017 eclipse. (a, c, e) TEC changes were caused by an eclipse with a 9.4nm EUV mask compared to a baseline run without the eclipse. (b, d, f) TEC changes caused by the EUV mask compared to the uniform eclipse mask assuming symmetric Sun with inflated solar radius by 10%. The red dashed line is a solar terminator at 100 km altitude. The Green dashed line is the magnetic equator. The purple contour denotes the EUV eclipse at EOF=0.9.

347 results show the increasing depletion growing within the eclipse’s shadow reaching ~ 5
 348 TECu. The TEC depletion was then trailing the eclipse pass at low latitudes, where the
 349 northern ionospheric crest density remained depleted even after the eclipse was gone (bot-
 350 tom panel). This is consistent with reported observations (magnitude 5-7 TECu) and
 351 the zonally-elongated depletion at lower latitudes (Coster et al., 2017; Cherniak & Za-
 352 kharenkova, 2018). Interestingly, the southern crest was first slightly negative (panel c)
 353 followed by a positive bay afterward. TEC observations from the southern hemisphere
 354 reported TEC depletion at low-latitudes (Zhang et al., 2021) and both depletion and in-
 355 crease at higher latitudes (He et al., 2018). These results reinforce the TEC data assim-
 356 ilation results indicating early reduction followed by the relative increase in the south-
 357 ern equatorial ionization anomaly (EIA) crest (Chen et al., 2019). The right column de-
 358 picts the difference between using a simple uniform mask and an eclipse mask at EUV
 359 wavelengths. The salient finding is that the use of the EUV mask contributes to as much
 360 as ± 1 TECu difference at a one-time instance (panel d) which corresponds to $\pm 20\%$ of
 361 the total TEC depletion. The biggest difference occurs when an eclipse is near local noon
 362 (e.g., panel d). Moreover, Figure 8d shows the difference-TEC gradients resemble the
 363 projection of solar active regions (Mrak et al., 2018; Hairston et al., 2018). Animation
 364 showing TEC perturbations for the whole eclipse pass is available as a supplemental movie
 365 S1.

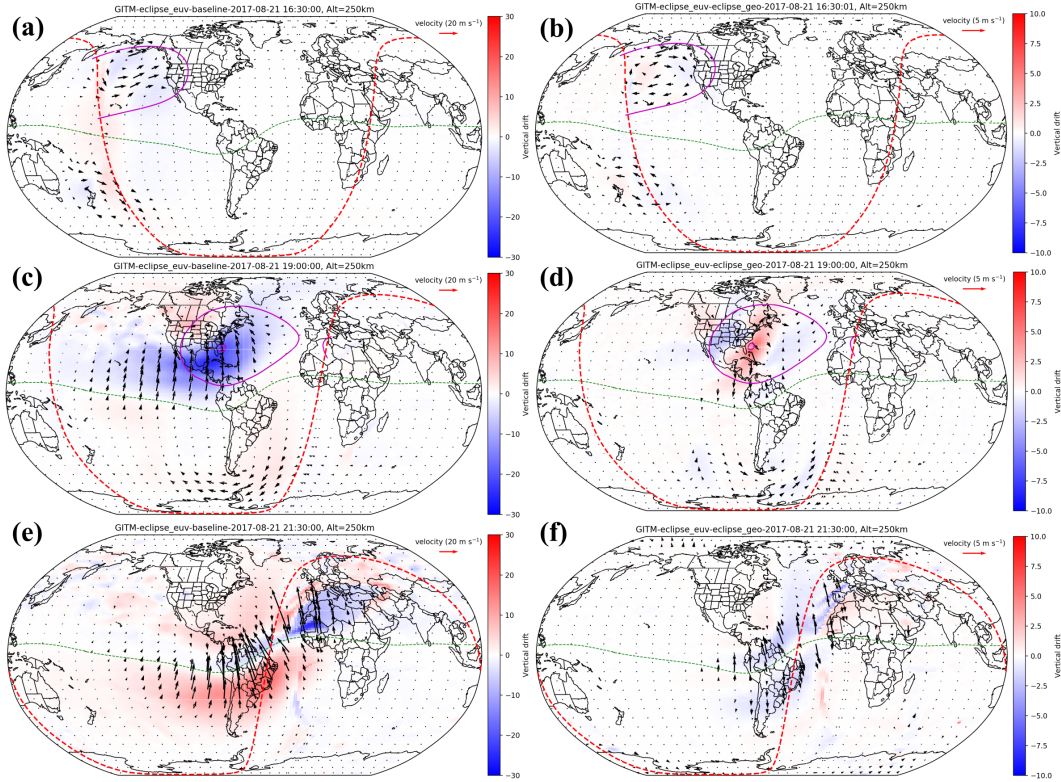


Figure 9. GITM modeled plasma drift at 250 km during the 21 August 2017 eclipse. The format is the same as in Figure 8, horizontal wind scale is at the top right of a panel. Color represents vertical plasma drift.

5.2 Plasma drift

The F-region plasma drift at 250 km altitude is depicted in Figure 9. The model results indicate the eclipse caused global plasma redistribution lasting even after the eclipse was gone. First, panel (a) at 16:30 UT shows the eclipse interacted with the sunrise terminator (red-dashed line) and that it had a weak conjugate effect. During the daytime eclipse transition, the horizontal drift was converging towards the maximum eclipse occultation, with downward plasma drift exceeding 10 m/s (negative velocity). The plasma drift maximized when the eclipse interacted with the sunset terminator and the equatorial electrojet shown in panel (e). The horizontal drift maximized in the vicinity of the magnetic equator, several degrees longitude into the night side with predominantly northward horizontal drifts of the order of 50 m/s and vertical drifts exceeding 20 m/s downward at the equator and upward at both EIA crests. Although the solar eclipse occurred in the northern hemisphere, the impacts are also present in the southern hemisphere because the hemispheres are electromagnetically coupled through closed field lines. Additionally, the dynamo electric field changed due to eclipse-induced neutral wind changes leading to changes at low-latitudes on both sides of the equator. The neutral wind can impact the plasma drift in two ways: 1) change the neutral dynamo electric field; 2) neutral-ion drag force directly impact plasma drift. The contribution of the EUV mask on the plasma drift was in the order of 5%-20% with the maximum contribution to the vertical drift during the daytime (panel d) and to the horizontal drift when interacting with the sunset terminator and the equatorial electrojet. The animation is available as a supplemental movie S2. The morphology of the plasma drift did not change significantly with altitudes above 250 km, except that the drift's magnitude increased with height.

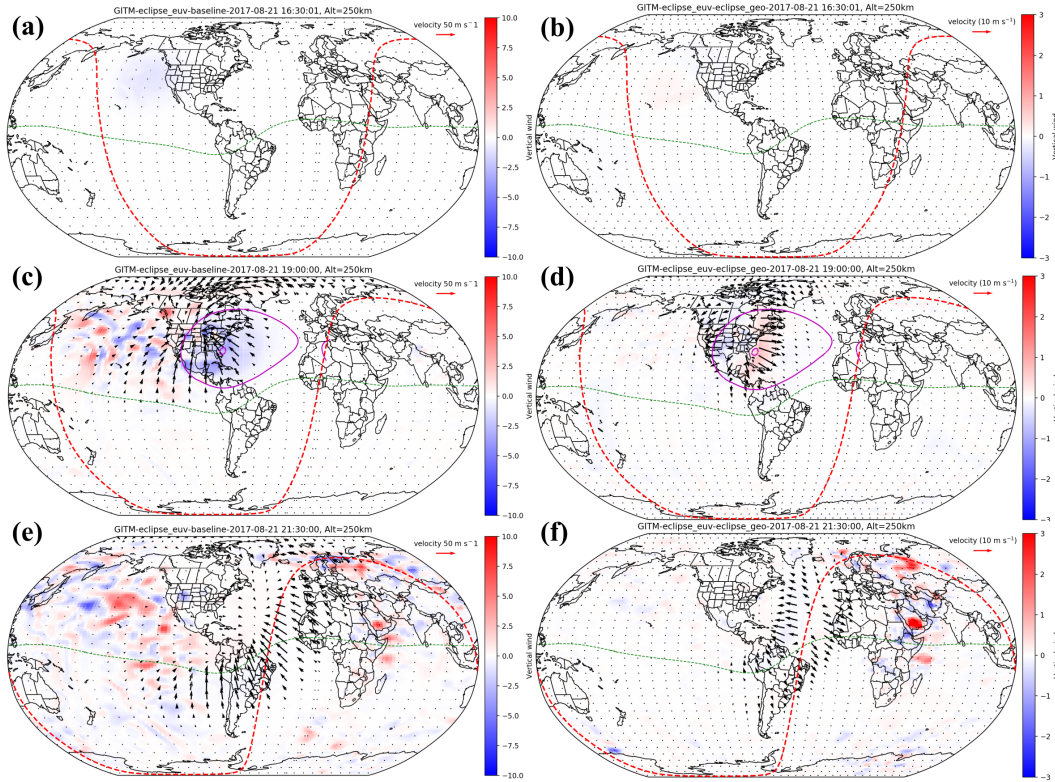


Figure 10. GITM modeled neutral wind at 250 km during the 21 August 2017 eclipse. The format is the same as in Figure 9, horizontal wind scale is at the top right of a panel. Color represents vertical winds.

389

5.3 Neutral winds

390

391

392

393

394

395

396

397

398

399

400

401

402

403

404

405

406

407

408

409

410

The neutral response to the eclipse is depicted in Figure 10. It can be observed that the eclipse caused a global thermospheric response to the cooling within the eclipse penumbra as shown by other authors (Wu et al., 2018; Cnossen et al., 2019; Harding et al., 2018). This cooling caused the neutral winds to converge toward the maximum eclipse with the biggest perturbation winds located in the leading half of the penumbra. The neutral response extended to the polar region and beyond the northern hemisphere as depicted in panel (c) making the eclipse response global. When the eclipse started to fade away, a large-scale bow-shaped wave-like traveling atmospheric disturbance emerged (panel e) that propagated into the nighttime and to the southern hemisphere as previously shown with observations (Harding et al., 2018) and numerical models (Dang et al., 2018; Lin et al., 2018). Significant activity in the vertical winds was present both on the eclipse trajectory, mainly lagging the penumbra, and on the nighttime hemisphere. While the former was previously explained with GITM simulations (Lin et al., 2018), the latter hasn't been reported. In comparison, a hydrostatic model showed just a smooth trendline (Dang et al., 2018). These waves were present in the night-time hemisphere and lasted for hours after the eclipse was gone. This indicates that some of the observations from Europe (T. G. Verhulst & Stankov, 2018) and from nighttime post-eclipse (Aryal et al., 2019) could be directly associated with the global thermospheric wind response. This feature is likely related to the global neutral wind response over the northern pole. The contribution of the EUV eclipse mask was more prominent compared to the plasma drift: the amplitude of horizontal wind was reduced by 20-30% (the vectors point in the opposite direction

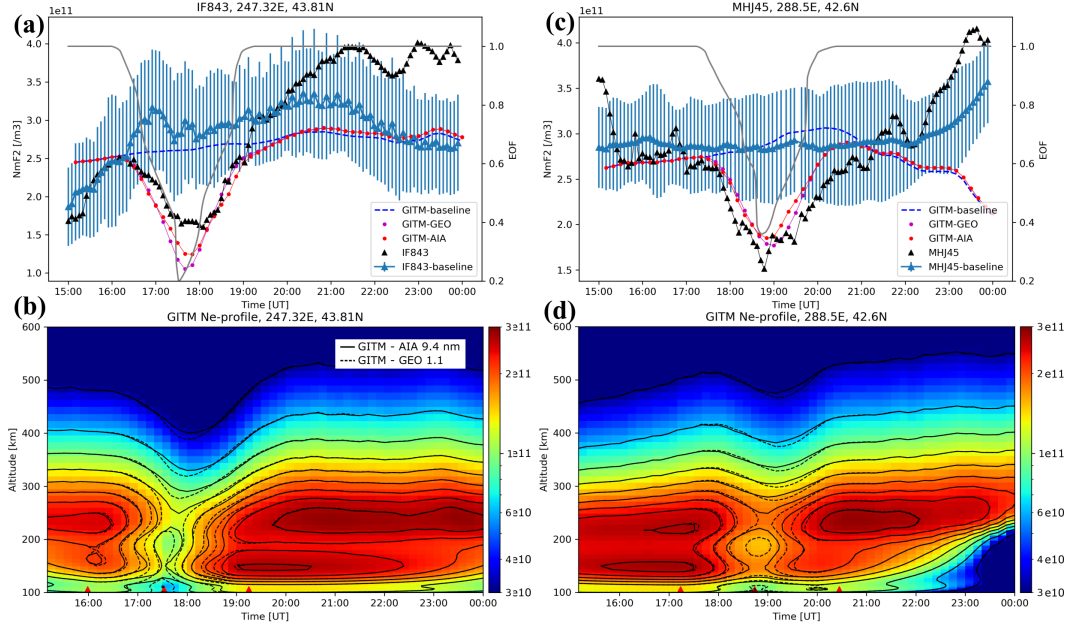


Figure 11. Ionosonde observations of NmF2 from Lusk, Idaho (left, IF843) and Millstone Hill (right, MHJ45) compared to GITM simulation outputs. The top row consists of time-series profiles of observed NmF2 (black), modeled GITM-AIA NmF2 (red), and modeled GITM-GEO NmF2. The blue-dashed line is GITM NmF2 without any eclipse mask. Light blue points are average NmF2 observed by the ionosonde in August 2017 with the corresponding spread represented by ± 1 standard deviation. The gray line is the 9.4 nm eclipse occultation function. The bottom tiles are vertical density profiles from GITM simulations. The heat maps are from the GITM-AIA run. Contours represent altitudes of constant density, solid lines from the GITM-AIA run, and the dashed line from the GITM-GEO run.

411 to the background trend) compared to the use of the GEO mask. The animation showing
 412 full thermospheric wind perturbations is available as a supplemental movie S3.

413 5.4 Height-dependent electron density

414 The height-dependent density response to the solar eclipse and comparison with
 415 ionosonde observations at Lusk, Idaho, and Millstone Hill, Massachusetts is depicted in
 416 Figure 11. The top panels show a trend of the peak F2-region density (NmF2) and stan-
 417 dard deviation for the month of August 2017 (minus the eclipse day) in blue and the eclipse-
 418 day observation in black. The NmF2 inferred from GITM runs using EUV 9.4 nm
 419 and GEO 1.1 masks and no eclipse (baseline) are plotted for comparison. In the bottom pan-
 420 els, we plot the electron density profile from GITM simulations. The NmF2 observations
 421 and GITM simulations indicate the lag between the maximum eclipse and the peak NmF2
 422 depletion to be in the order of 15-30 minutes. The general trend in the observed NmF2
 423 has been elaborated before (Wu et al., 2018; Reinisch et al., 2018) so we focus on the dif-
 424 ferences caused by the two eclipse masks. The differences are due to the plateau in the
 425 GEO EOF due to the increased solar radius as discussed in Figure 3. This caused big-
 426 ger maximum depletion at both locations compared to the SDO AIA mask. The smaller
 427 depletion caused by the SDO AIA mask was closer to observations. There are some dis-
 428 tinct differences between the model results and observations with the most profound dif-
 429 ference being the post-eclipse increase in density and signatures of waves – specifically

430 at Millstone Hill. These features are described and elaborated in the literature and are
 431 beyond the scope of this paper focusing on the eclipse mask and the associated local re-
 432 sponse to abated EUV.

433 Vertical density profiles at both locations are depicted in the bottom row of Fig-
 434 ure 11. Contours mark the altitudes of constant density over time, where the solid lines
 435 are from the GITM run with the EUV mask and the dashed lines are from the GITM-
 436 GEO 1.1 run. Both locations show that the GITM-GEO caused bigger density depletion
 437 at all altitudes. The biggest differences are observed at altitudes below 200 km due
 438 to a rapid response of molecular ions to a different shape of incoming irradiance. The
 439 magnitude of density reductions varies with altitude and time because the recombina-
 440 tion time-constant is increasing with height yielding a slower response to the abated EUV
 441 flux. During the recovery, the F1 density in Idaho was higher compared to the F2-
 442 region density following the maximum eclipse (second red ticker on the x-axis), whereas
 443 this was not the case at Millstone Hill (panel d). The result from Lusk, Idaho, is in agree-
 444 ment with the observed G-condition, that is a situation where $NmF1 \geq NmF2$, from Wyoming
 445 ionosonde measurements (Bullett & Mabie, 2018) and historical literature (Rishbeth, 1968).

446 6 Summary

447 We introduced a computational model of solar eclipse masks PyEclipse, that com-
 448 puted eclipse occultation factors as a function of geolocation, time, and wavelength. The
 449 eclipse occultations can be computed using the traditional approach assuming a geomet-
 450 rically symmetric Sun with a variable radius. In addition, PyEclipse computes EUV eclipses
 451 at 9 wavelengths using SDO AIA and GOES-R SUVI telescopes. We discuss spatiotem-
 452 poral features of EUV masks, featuring overall slightly different eclipse occultation gra-
 453 dients compared to the GEO mask, and spatiotemporal gradients due to projections of
 454 solar active regions. The differences between EUV and GEO masks depend on solar ac-
 455 tivity and depends on EUV wavelength. We show that in general the uniform GEO mask
 456 overestimates and underestimated the EOF by $\pm 20\%$, that the position of the maximum
 457 eclipse and varies wand is wavelength dependent and that the eclipse mask varies with
 458 altitude owing to the solar active region projection. The spatiotemporal morphology of
 459 modeled eclipse mask was validated using in-situ observations from PROBA2 spacecraft.
 460 We identified that the modeled EOF follows the observations. The model captures the
 461 eclipse magnitude as a function of wavelength, timing, and duration of transients. The
 462 instantaneous response to these transients, however, lags the magnitude of observed changes.

463 The effects of EUV spatiotemporal variability were assessed with GITM using the
 464 21 August 2017 case study. We identified that the EUV mask contributed up to $\pm 20\%$
 465 in TEC changes, 5-20% in the F-region plasma drift changes, and 20-30% in the neutral
 466 wind response. These results bolster the need for using EUV masks for eclipse simula-
 467 tions and data-model comparison. We compared the plasma response with two ionoson-
 468 des. The modeled NmF2 decrease with the EUV mask was smaller in magnitude but had
 469 a slower recovery compared to the GEO mask. While these modeled changes might be
 470 perceived as small, the impacts of the transient gradients in the ionospheric density cre-
 471 ate spatial gradients in ionospheric conductance which controls how magnetospheric cur-
 472 rent close, thereby directly affecting the magnetosphere-ionosphere coupling during eclipses
 473 occurring at high-latitudes.

474 7 Open Research

475 PyEclipse is open source software, available from GitHub <https://github.com/aldebaran1/PyEclipse>
 476 (Mrak, 2022). All eclipse masks used in this paper can be reproduced using the PyE-
 477 clipse software package. GITM simulation outputs used in this study are available from
 478 NCAR GDEX <https://doi.org/10.5065/1mtb-e447>. Calibrated PROBA2/LYRA data and
 479 ionosonde data files are available from Zenodo: <https://doi.org/10.5281/zenodo.7042037>

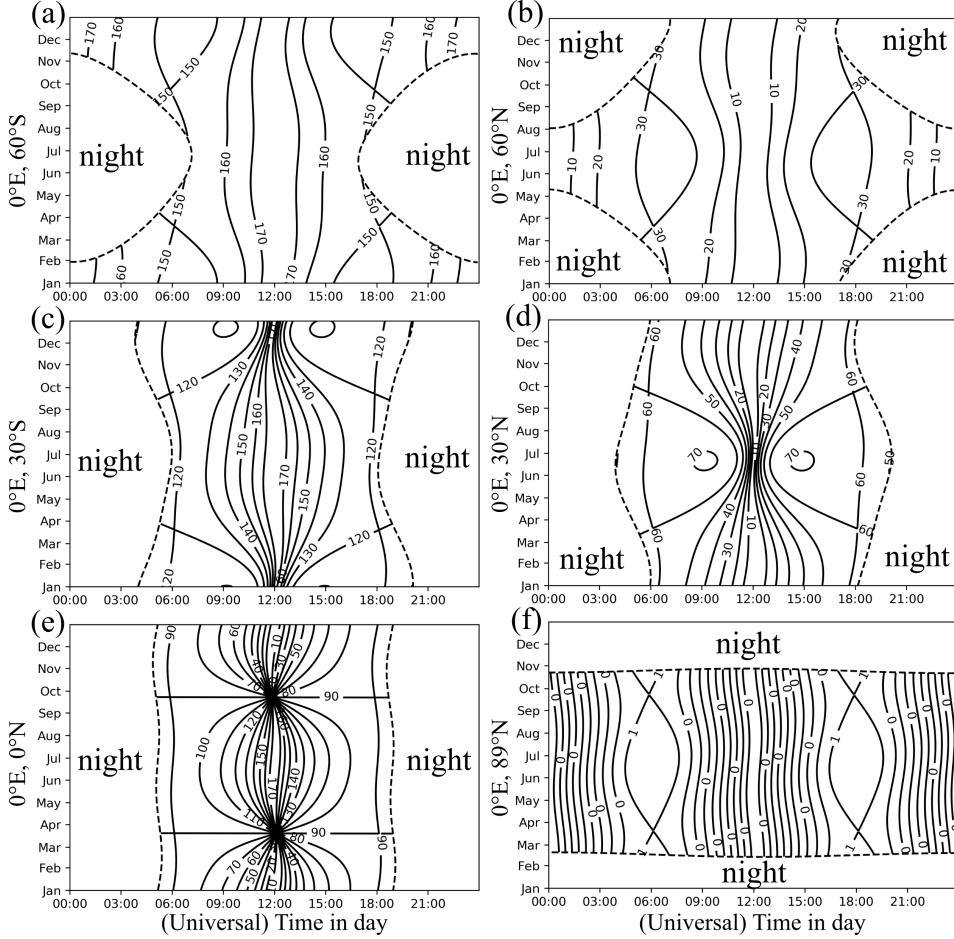


Figure A1. Parallax angle as a function of time in a day (x-axis), time in a year (y-axis), and different geographic latitudes (a–f) at the zero longitudes (the Greenwich meridian). Dashed lines denote the line of solar zenith angle at 90 degrees (solar terminator).

480 **Appendix A Parallax angle**

481 The impact of parallax angle η on the observer in the Earth’s inertial coordinate
 482 system was introduced by Meadows (2007). We depict its local time, seasonal and lat-
 483 tudinal dependence in Figure A1. The magnitude of the parallax angle and its rate
 484 of change highly depends on the latitude. The biggest rate of change occurs just around
 485 12 noon when the location of the observer crosses the sub-solar point. At the equator,
 486 the magnitude of η changes considerably with the season: There is no change in η dur-
 487 ing equinoxes, while η changes by $\pm 90^\circ$ during solstices. The magnitude, rate of change,
 488 and seasonal dependence reduce closer to the poles. At the poles, η is constant through-
 489 out the year and day, during polar summer. This is because an observer sitting at the
 490 pole has the local zenith always aligned with the Sun’s pole. Either looking in exactly
 491 the same direction when at the north pole ($\eta = 0$) or exactly in the opposite direction
 492 at the sought pole ($\eta = 180$).

493 **Appendix B EOF of a geometrically symmetric eclipse**

494 The geometrically symmetric eclipse is a spherical geometry exercise where the eclipse
 495 occultation is a ratio of the occulted area A (area of two overlapping circles) over the

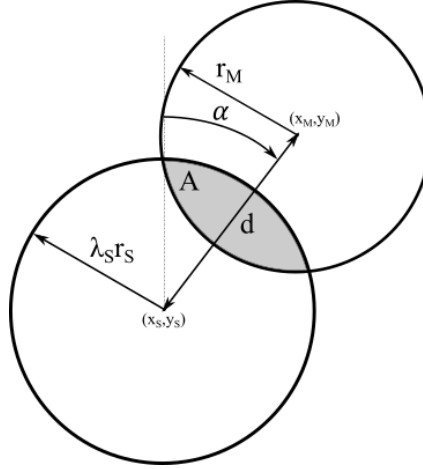


Figure B1. Illustration of the geometrically symmetric eclipse calculation with the Sun (subscript S) and the Moon (subscript M) assumed as circles. The distance d , and the bearing angle α are computed using the spherical geometry formulae. The resulting eclipse occultation function is the area of the circles' overlapping region, i.e., the shared area.

496 area of the Sun derived in Section 2, Equation 5. The illustration of this problem is depicted in Figure B1. Here, the bearing angle α between the Sun and the Moon was defined in Equation 2 and the distance d between the centers of the bodies in Equation 1. 497
498
499 In the calculation of the overlapping area A we assume the position of the center of the Sun $(x_s, y_s) = (0, 0)$. The position of the center of the Moon (x_m, y_m) is computed via 500
501 the coordinate transformation from d, α :

$$x_m = \arctan\left(\frac{\sin d \sin \alpha}{\cos d}\right) \quad (\text{B1})$$

$$y_m = \arcsin(\sin d \cos \alpha) \quad (\text{B2})$$

502 Then, the overlapping area A is

$$A = r_s^2 \arccos\left(\frac{d_1}{r_s}\right) - d_1 \sqrt{r_s^2 - d_1^2} + r_m^2 \arccos\left(\frac{d_2}{r_m}\right) - d_2 \sqrt{r_m^2 - d_2^2} \quad (\text{B3})$$

503 where,

$$d_1 = \frac{r_s^2 - r_m^2 + \sqrt{d_0^2}}{2d_0} \quad (\text{B4})$$

$$d_2 = d_0 - d_1 \quad (\text{B5})$$

$$d_0 = \sqrt{x_m^2 + y_m^2} \quad (\text{B6})$$

504 Acknowledgments

505 The study was supported by NSF-AGS 1929879 and NASA 80NSSC22K0324 to Boston
506 University and the University of Colorado Boulder. PROBA2 Lyra data is available from
507 <https://proba2.sidc.be/data/lyra/level2>. The ionosonde data is available from
508 <https://giro.uml.edu/didbase/scaled.php>.

509 References

510 Aryal, S., Geddes, G., Finn, S. C., Mrak, S., Galkin, I., Cnossen, I., . . . Chakrabarti,
511 S. (2019, 5). Multispectral and multi-instrument observation of tids following

- 512 the total solar eclipse of 21 august 2017. *Journal of Geophysical Research:*
 513 *Space Physics*, 124, 3761-3774. Retrieved from [https://onlinelibrary](https://onlinelibrary.wiley.com/doi/abs/10.1029/2018JA026333)
 514 [.wiley.com/doi/abs/10.1029/2018JA026333](https://onlinelibrary.wiley.com/doi/abs/10.1029/2018JA026333) doi: 10.1029/2018JA026333
- 515 Barnes, W. T., Bobra, M. G., Christe, S. D., Freij, N., Hayes, L. A., Ireland, J., ...
 516 Dang, T. K. (2020). The sunpy project: Open source development and status
 517 of the version 1.0 core package. *The Astrophysical Journal*, 890, 68. doi:
 518 10.3847/1538-4357/ab4f7a
- 519 BenMoussa, A., Dammasch, I. E., Hochedez, J.-F., Schühle, U., Koller, S., Stock-
 520 man, Y., ... Schmutz, W. (2009, 12). Pre-flight calibration of lyra, the solar
 521 vuv radiometer on board proba2. *Astronomy & Astrophysics*, 508, 1085-1094.
 522 Retrieved from <http://www.aanda.org/10.1051/0004-6361/200913089> doi:
 523 10.1051/0004-6361/200913089
- 524 BenMoussa, A., Gissot, S., Schühle, U., Zanna, G. D., Auchère, F., Mekaoui, S., ...
 525 Woods, T. N. (2013, 11). On-orbit degradation of solar instruments. *Solar*
 526 *Physics*, 288, 389-434. Retrieved from [https://link.springer.com/](https://link.springer.com/article/10.1007/s11207-013-0290-z)
 527 [article/10.1007/s11207-013-0290-z](https://link.springer.com/article/10.1007/s11207-013-0290-z) doi: 10.1007/S11207-013-0290-Z/
 528 FIGURES/27
- 529 Bravo, M., Martínez-Ledesma, M., Foppiano, A., Urra, B., Ovalle, E., Villalobos,
 530 C., ... Stepanova, M. (2020, 9). First report of an eclipse from chilean
 531 ionosonde observations: Comparison with total electron content estimations
 532 and the modeled maximum electron concentration and its height. *Jour-*
 533 *nal of Geophysical Research: Space Physics*, 125, 1-21. Retrieved from
 534 <https://onlinelibrary.wiley.com/doi/10.1029/2020JA027923> doi:
 535 10.1029/2020JA027923
- 536 Bullett, T., & Mabie, J. (2018, 4). Vertical and oblique ionosphere sounding dur-
 537 ing the 21 august 2017 solar eclipse. *Geophysical Research Letters*, 45, 3690-
 538 3697. Retrieved from [https://onlinelibrary.wiley.com/doi/abs/10.1002/](https://onlinelibrary.wiley.com/doi/abs/10.1002/2018GL077413)
 539 [2018GL077413](https://onlinelibrary.wiley.com/doi/abs/10.1002/2018GL077413) doi: 10.1002/2018GL077413
- 540 Chen, C.-H., Lin, C.-H. C., & Matsuo, T. (2019, 2). Ionospheric re-
 541 sponses to the 21 august 2017 solar eclipse by using data assimilation
 542 approach. *Progress in Earth and Planetary Science*, 6. Retrieved
 543 from [https://progearthplanetsci.springeropen.com/articles/](https://progearthplanetsci.springeropen.com/articles/10.1186/s40645-019-0263-4)
 544 [10.1186/s40645-019-0263-4](https://progearthplanetsci.springeropen.com/articles/10.1186/s40645-019-0263-4)[http://files/1384/Chenetal.-2019](http://files/1384/Chenetal.-2019-Ionosphericresponsestothe21August2017solar.pdf)
 545 [-Ionosphericresponsestothe21August2017solar.pdf](http://files/1384/Chenetal.-2019-Ionosphericresponsestothe21August2017solar.pdf) doi: 10.1186/
 546 s40645-019-0263-4
- 547 Cherniak, I., & Zakharenkova, I. (2018, 2). Ionospheric total electron content re-
 548 sponse to the great american solar eclipse of 21 august 2017. *Geophysical Re-*
 549 *search Letters*, 45, 1199-1208. Retrieved from [https://onlinelibrary.wiley](https://onlinelibrary.wiley.com/doi/10.1002/2017GL075989)
 550 [.com/doi/10.1002/2017GL075989](https://onlinelibrary.wiley.com/doi/10.1002/2017GL075989) doi: 10.1002/2017GL075989
- 551 Cnossen, I., Ridley, A. J., Goncharenko, L. P., & Harding, B. J. (2019, 8). The
 552 response of the ionosphere-thermosphere system to the 21 august 2017 so-
 553 lar eclipse. *Journal of Geophysical Research: Space Physics*, 124, 7341-
 554 7355. Retrieved from [https://onlinelibrary.wiley.com/doi/10.1029/](https://onlinelibrary.wiley.com/doi/10.1029/2018JA026402)
 555 [2018JA026402](https://onlinelibrary.wiley.com/doi/10.1029/2018JA026402) doi: 10.1029/2018JA026402
- 556 Coster, A. J., Goncharenko, L., Zhang, S.-R., Erickson, P. J., Rideout, W., &
 557 Vierinen, J. (2017, 12). Gns observations of ionospheric variations during
 558 the 21 august 2017 solar eclipse. *Geophysical Research Letters*, 44, 12,041-
 559 12,048. Retrieved from <http://doi.wiley.com/10.1002/2017GL075774> doi:
 560 10.1002/2017GL075774
- 561 Dang, T., Lei, J., Wang, W., Zhang, B., Burns, A., Le, H., ... Wan, W. (2018, 8).
 562 Global responses of the coupled thermosphere and ionosphere system to the
 563 august 2017 great american solar eclipse. *Journal of Geophysical Research:*
 564 *Space Physics*, 123, 7040-7050. doi: 10.1029/2018JA025566
- 565 Darnel, J. M., Seaton, D. B., Bethge, C., Rachmeler, L., Jarvis, A., Hill, S. M., ...
 566 Timothy, S. (2022, 4). The goes-r solar ultraviolet imager. *Space Weather*,

20. Retrieved from <https://onlinelibrary.wiley.com/doi/10.1029/2022SW003044> doi: 10.1029/2022SW003044
- 569 Davis, C. J., Lockwood, M., Bell, S. A., Smith, J. A., & Clarke, E. M. (2000, 2).
570 Ionospheric measurements of relative coronal brightness during the total solar
571 eclipses of 11 august, 1999 and 9 july, 1945. *Annales Geophysicae*, *18*, 182-190.
572 Retrieved from <https://angeo.copernicus.org/articles/18/182/2000/>
573 doi: 10.1007/s00585-000-0182-z
- 574 Deehr, C. S., & Rees, M. H. (1964, 9). The eclipse of 20 july 1963 spectrophoto-
575 metry of atmospheric emissions. *Planetary and Space Science*, *12*, 875-
576 888. Retrieved from [https://linkinghub.elsevier.com/retrieve/pii/](https://linkinghub.elsevier.com/retrieve/pii/0032063364900479)
577 [0032063364900479](https://linkinghub.elsevier.com/retrieve/pii/0032063364900479) doi: 10.1016/0032-0633(64)90047-9
- 578 Deng, Y., Fuller-Rowell, T. J., Akmaev, R. A., & Ridley, A. J. (2011, 5). Impact
579 of the altitudinal joule heating distribution on the thermosphere. *Journal of*
580 *Geophysical Research: Space Physics*, *116*, 5313. Retrieved from [http://](http://doi.wiley.com/10.1029/2010JA016019)
581 doi.wiley.com/10.1029/2010JA016019 doi: 10.1029/2010JA016019
- 582 Deng, Y., Lin, C. Y., Zhu, Q., & Sheng, C. (2021, 3). *Influence of nonhydrostatic*
583 *processes on the ionosphere-thermosphere* (Vol. 4). Retrieved from [https://](https://onlinelibrary.wiley.com/doi/10.1002/9781119815631.ch4)
584 onlinelibrary.wiley.com/doi/10.1002/9781119815631.ch4 doi: 10.1002/
585 9781119815631.ch4
- 586 Deng, Y., Richmond, A. D., Ridley, A. J., & Liu, H. L. (2008). Assessment
587 of the non-hydrostatic effect on the upper atmosphere using a general
588 circulation model (gcm). *Geophysical Research Letters*, *35*, 2-6. doi:
589 10.1029/2007GL032182
- 590 Dominique, M., Hochedez, J.-F., Schmutz, W., Dammasch, I. E., Shapiro, A. I.,
591 Kretschmar, M., ... BenMoussa, A. (2013, 8). The lyra instrument onboard
592 proba2: Description and in-flight performance. *Solar Physics*, *286*, 21-42. Re-
593 trieved from <http://link.springer.com/10.1007/s11207-013-0252-5> doi:
594 10.1007/s11207-013-0252-5
- 595 Hairston, M. R., Mrak, S., Coley, W. R., Burrell, A., Holt, B., Perdue, M., ...
596 Power, R. (2018, 8). Topside ionospheric electron temperature observa-
597 tions of the 21 august 2017 eclipse by dmsp spacecraft. *Geophysical Research*
598 *Letters*, *45*, 7242-7247. Retrieved from [http://doi.wiley.com/10.1029/](http://doi.wiley.com/10.1029/2018GL077381)
599 [2018GL077381](http://doi.wiley.com/10.1029/2018GL077381) doi: 10.1029/2018GL077381
- 600 Harding, B. J., Drob, D. P., Buriti, R. A., & Makela, J. J. (2018, 4). Night-
601 side detection of a large-scale thermospheric wave generated by a solar
602 eclipse. *Geophysical Research Letters*, *45*, 3366-3373. Retrieved from
603 <https://onlinelibrary.wiley.com/doi/abs/10.1002/2018GL077015> doi:
604 10.1002/2018GL077015
- 605 He, L., Heki, K., & Wu, L. (2018). Three-dimensional and trans-hemispheric changes
606 in ionospheric electron density caused by the great solar eclipse in north amer-
607 ica on 21 august 2017. *Geophysical Research Letters*, *45*, 10,933-10,940. doi:
608 10.1029/2018GL080365
- 609 Huba, J. D., & Drob, D. (2017, 6). Sami3 prediction of the impact of the 21 au-
610 gust 2017 total solar eclipse on the ionosphere/plasmasphere system. *Geophys-*
611 *ical Research Letters*, *44*, 5928-5935. Retrieved from [http://doi.wiley.com/](http://doi.wiley.com/10.1002/2017GL073549)
612 [10.1002/2017GL073549](http://doi.wiley.com/10.1002/2017GL073549) doi: 10.1002/2017GL073549
- 613 Kaplan, G. H., Bartlett, J. L., Monet, A. K. B., Bangert, J. A., & Puatua, W. K.
614 (2011). *User's guide to novas version f3.1*.
- 615 Le, H., Liu, L., Yue, X., & Wan, W. (2008). The ionospheric responses to the 11 au-
616 gust 1999 solar eclipse: Observations and modeling. *Annales Geophysicae*, *26*,
617 107-116. doi: 10.5194/angeo-26-107-2008
- 618 Lemen, J. R., Title, A. M., Akin, D. J., Boerner, P. F., Chou, C., Drake, J. F., ...
619 Waltham, N. (2012, 1). The atmospheric imaging assembly (aia) on the so-
620 lar dynamics observatory (sdo). *Solar Physics*, *275*, 17-40. Retrieved from
621 <http://link.springer.com/10.1007/s11207-011-9776-8><http://files/>

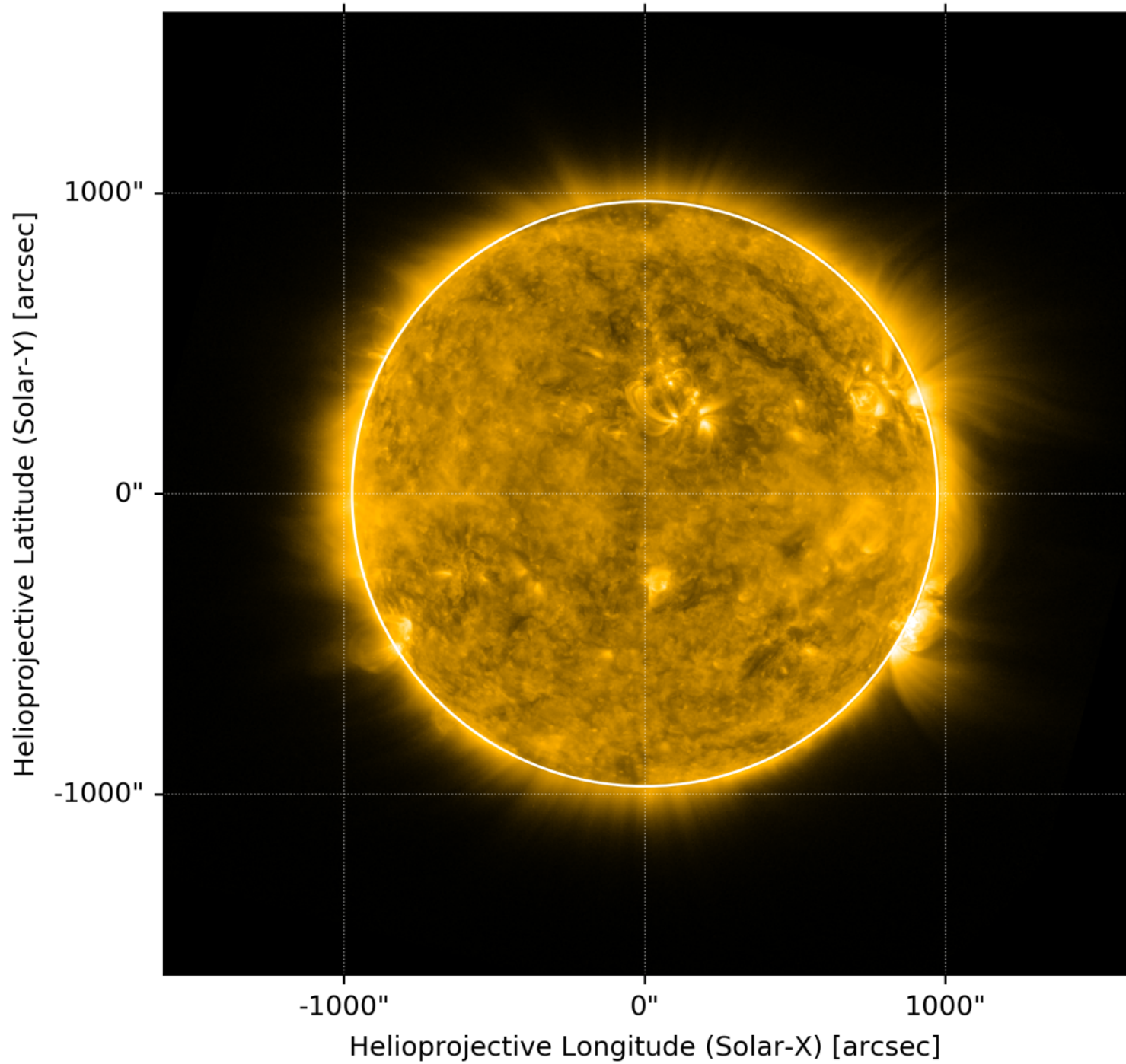
- 1340/Lemenetal.-2012-TheAtmosphericImagingAssembly(AIA)ontheSola
.pdf doi: 10.1007/s11207-011-9776-8
- 622
623
- 624 Lin, C. Y., Deng, Y., & Ridley, A. (2018, 5). Atmospheric gravity waves in
625 the ionosphere and thermosphere during the 2017 solar eclipse. *Geophys-*
626 *ical Research Letters*. Retrieved from [http://doi.wiley.com/10.1029/](http://doi.wiley.com/10.1029/2018GL077388)
627 [http://files/857/Lin_et_al-2018-Geophysical_Research](http://files/857/Lin_et_al-2018-Geophysical_Research_Letters.pdf)
628 [_Letters.pdf](http://files/857/Lin_et_al-2018-Geophysical_Research_Letters.pdf) doi: 10.1029/2018GL077388
- 629 Lin, C. Y., Deng, Y., Sheng, C., & Drob, D. P. (2017, 1). A study of the nonlinear
630 response of the upper atmosphere to episodic and stochastic acoustic-gravity
631 wave forcing. *Journal of Geophysical Research: Space Physics*, *122*, 1178-
632 1198. Retrieved from [https://onlinelibrary.wiley.com/doi/10.1002/](https://onlinelibrary.wiley.com/doi/10.1002/2016JA022930)
633 [2016JA022930](https://onlinelibrary.wiley.com/doi/10.1002/2016JA022930) doi: 10.1002/2016JA022930
- 634 Marriott, R. T., John, D. E. S., Thorne, R. M., & Venkateswaran, S. V. (1971, 12).
635 Xuv image of the sun from eclipse observations of the ionospheric e-region. *So-*
636 *lar Physics*, *21*, 483-494. Retrieved from [http://files/910/1971SoPh__21_](http://files/910/1971SoPh__21_483M.pdf)
637 [_483M.pdf](http://files/910/1971SoPh__21_483M.pdf)<http://link.springer.com/10.1007/BF00154303> doi: 10.1007/
638 [BF00154303](http://link.springer.com/10.1007/BF00154303)
- 639 Marriott, R. T., John, D. E. S., Thorne, R. M., Venkateswaran, S. V., & Ma-
640 hadevan, P. (1972). Ionospheric effects of two recent solar eclipses. *Jour-*
641 *nal of Atmospheric and Terrestrial Physics*, *34*, 695-712. doi: 10.1016/
642 [0021-9169\(72\)90157-2](https://doi.org/10.1016/0021-9169(72)90157-2)
- 643 Maute, A., & Richmond, A. D. (2017, 3). *f*-region dynamo simulations at low and
644 mid-latitude. *Space Science Reviews*, *206*, 471-493. Retrieved from [http://](http://link.springer.com/10.1007/s11214-016-0262-3)
645 link.springer.com/10.1007/s11214-016-0262-3 doi: 10.1007/s11214-016-
646 [0262-3](http://link.springer.com/10.1007/s11214-016-0262-3)
- 647 McInerney, J. M., Marsh, D. R., Liu, H., Solomon, S. C., Conley, A. J., & Drob,
648 D. P. (2018, 5). Simulation of the 21 august 2017 solar eclipse using the whole
649 atmosphere community climate model-extended. *Geophysical Research Letters*,
650 *45*, 3793-3800. Retrieved from [https://onlinelibrary.wiley.com/doi/](https://onlinelibrary.wiley.com/doi/10.1029/2018GL077723)
651 [10.1029/2018GL077723](https://onlinelibrary.wiley.com/doi/10.1029/2018GL077723) doi: 10.1029/2018GL077723
- 652 Meadows, P. (2007). The parallactic angle and the solar observer. *Journal of the*
653 *British Astronomical Association*, *117*, 35-36.
- 654 Mrak, S. (2022, 09). *aldebaran1/pyeclipse: v0.1.0. [software]*. Retrieved
655 from <https://github.com/aldebaran1/pyEclipse/>
656 [zenodo.7044996](https://github.com/aldebaran1/pyEclipse/) doi: 10.5281/
[zenodo.7044996](https://github.com/aldebaran1/pyEclipse/)
- 657 Mrak, S., Semeter, J., Drob, D., & Huba, J. D. (2018, 5). Direct evf/x-ray mod-
658 ulation of the ionosphere during the august 2017 total solar eclipse. *Geophys-*
659 *ical Research Letters*, *45*, 3820-3828. Retrieved from [http://doi.wiley.com/](http://doi.wiley.com/10.1029/2017GL076771)
660 [10.1029/2017GL076771](http://doi.wiley.com/10.1029/2017GL076771) doi: 10.1029/2017GL076771
- 661 Nestorov, G., & Taubenheim, J. (1962, 7). Untersuchungen an der ionosphärischen
662 e-schicht während der totalen sonnenfinsternis 15 februar 1961. *Jour-*
663 *nal of Atmospheric and Terrestrial Physics*, *24*, 633-642. Retrieved from
664 <https://linkinghub.elsevier.com/retrieve/pii/0021916962900855> doi:
665 [10.1016/0021-9169\(62\)90085-5](https://linkinghub.elsevier.com/retrieve/pii/0021916962900855)
- 666 Reinisch, B. W., Dandenault, P. B., Galkin, I. A., Hamel, R., & Richards,
667 P. G. (2018, 2). Investigation of the electron density variation dur-
668 ing the 21 august 2017 solar eclipse. *Geophysical Research Letters*, *45*,
669 1253-1261. Retrieved from [https://onlinelibrary.wiley.com/doi/](https://onlinelibrary.wiley.com/doi/abs/10.1002/2017GL076572)
670 [abs/10.1002/2017GL076572](https://onlinelibrary.wiley.com/doi/abs/10.1002/2017GL076572)[http://files/1371/Reinischetal.-2018](http://files/1371/Reinischetal.-2018-InvestigationoftheElectronDensityVariationDu.pdf)
671 [-InvestigationoftheElectronDensityVariationDu.pdf](http://files/1371/Reinischetal.-2018-InvestigationoftheElectronDensityVariationDu.pdf) doi: 10.1002/
672 [2017GL076572](https://onlinelibrary.wiley.com/doi/abs/10.1002/2017GL076572)
- 673 Ridley, A., Deng, Y., & Tóth, G. (2006, 5). The global ionosphere-thermosphere
674 model. *Journal of Atmospheric and Solar-Terrestrial Physics*, *68*, 839-
675 864. Retrieved from [https://linkinghub.elsevier.com/retrieve/pii/](https://linkinghub.elsevier.com/retrieve/pii/S1364682606000071)
676 [S1364682606000071](https://linkinghub.elsevier.com/retrieve/pii/S1364682606000071) doi: 10.1016/j.jastp.2006.01.008

- 677 Ridley, E. C., Dickinson, R. E., Roble, R. G., & Rees, M. H. (1984, 9). Thermo-
678 spheric response to the june 11, 1983, solar eclipse. *Journal of Geophysical Re-*
679 *search: Space Physics*, *89*, 7583-7588. Retrieved from [http://doi.wiley.com/](http://doi.wiley.com/10.1029/JA089iA09p07583)
680 [10.1029/JA089iA09p07583](http://doi.wiley.com/10.1029/JA089iA09p07583) doi: 10.1029/JA089iA09p07583
- 681 Rishbeth, H. (1968, 9). Solar eclipses and ionospheric theory. *Space Science Reviews*,
682 *8*, 543-554. Retrieved from <http://link.springer.com/10.1007/BF00175006>
683 doi: 10.1007/BF00175006
- 684 Smith, L. G., Accardo, C. A., Weeks, L. H., & McKinnon, P. J. (1965, 7). Mea-
685 surements in the ionosphere during the solar eclipse of 20 july 1963. *Journal of*
686 *Atmospheric and Terrestrial Physics*, *27*, 803-829. doi: 10.1016/0021-9169(65)
687 90049-8
- 688 Stankov, S. M., Bergeot, N., Berghmans, D., Bolsée, D., Bruyninx, C., Chevalier,
689 J.-M., ... West, M. J. (2017, 3). Multi-instrument observations of the solar
690 eclipse on 20 march 2015 and its effects on the ionosphere over belgium and
691 europe. *Journal of Space Weather and Space Climate*, *7*, A19. Retrieved from
692 [http://www.swsc-journal.org/10.1051/swsc/2017017http://files/799/](http://www.swsc-journal.org/10.1051/swsc/2017017http://files/799/swsc160032.pdf)
693 [swsc160032.pdf](http://www.swsc-journal.org/10.1051/swsc/2017017http://files/799/swsc160032.pdf) doi: 10.1051/swsc/2017017
- 694 Taubenheim, J., & Serafimov, K. (1969, 2). Brightness distribution of soft x-rays on
695 the sun, inferred from ionospheric e-layer variations during an eclipse. *Journal*
696 *of Atmospheric and Terrestrial Physics*, *31*, 307-312. Retrieved from [https://](https://linkinghub.elsevier.com/retrieve/pii/0021916969900476)
697 linkinghub.elsevier.com/retrieve/pii/0021916969900476 doi: 10.1016/
698 0021-9169(69)90047-6
- 699 Torr, D., Torr, M., Brinton, H., Brace, L., Spencer, N., Hedin, A., ... Rusch, D.
700 (1979). An experimental and theoretical study of the mean diurnal varia-
701 tion of $o\ j_{sup\ i} / j_{sup\ i}$, $no\ j_{sup\ i} / j_{sup\ i}$, $o\ j_{sub\ i} / j_{sub\ i}$, $o\ j_{sub\ i} / j_{sub\ i}$, and
702 $n\ j_{sub\ i} / j_{sub\ i}$ ions in the mid-latitude f_i / i_i f_i / i_i layer of the ionosphere. *Journal of Geophysical Research*, *84*, 3360. Re-
703 trieved from <http://doi.wiley.com/10.1029/JA084iA07p03360> doi:
704 [10.1029/JA084iA07p03360](http://doi.wiley.com/10.1029/JA084iA07p03360)
- 705 Verhulst, T. G., & Stankov, S. M. (2018, 5). Ionospheric wave signature of the
706 american solar eclipse on 21 august 2017 in europe. *Advances in Space Re-*
707 *search*, *61*, 2245-2251. Retrieved from [https://linkinghub.elsevier.com/](https://linkinghub.elsevier.com/retrieve/pii/S0273117718301224)
708 [retrieve/pii/S0273117718301224](https://linkinghub.elsevier.com/retrieve/pii/S0273117718301224) doi: 10.1016/j.asr.2018.02.007
- 709 Verhulst, T. G. W., & Stankov, S. M. (2020, 7). Height dependency of solar eclipse
710 effects: The ionospheric perspective. *Journal of Geophysical Research: Space*
711 *Physics*, *125*, 1-20. Retrieved from [https://onlinelibrary.wiley.com/doi/](https://onlinelibrary.wiley.com/doi/10.1029/2020JA028088)
712 [10.1029/2020JA028088](https://onlinelibrary.wiley.com/doi/10.1029/2020JA028088) doi: 10.1029/2020JA028088
- 713 Wu, C., Ridley, A. J., Goncharenko, L., & Chen, G. (2018, 7). Gitm-data compar-
714 isons of the depletion and enhancement during the 2017 solar eclipse. *Geophys-*
715 *ical Research Letters*, *45*, 3319-3327. Retrieved from [http://doi.wiley.com/](http://doi.wiley.com/10.1002/2018GL077409http://files/963/2018GL077409.pdf)
716 [10.1002/2018GL077409http://files/963/2018GL077409.pdf](http://doi.wiley.com/10.1002/2018GL077409http://files/963/2018GL077409.pdf) doi: 10.1002/
717 2018GL077409
- 718 Zhang, S. R., Erickson, P. J., Vierinen, J., Aa, E., Rideout, W., Coster, A. J., &
719 Goncharenko, L. P. (2021, 2). Conjugate ionospheric perturbation during the
720 2017 solar eclipse. *Journal of Geophysical Research: Space Physics*, *126*. doi:
721 [10.1029/2020JA028531](https://doi.org/10.1029/2020JA028531)
- 722 Zhu, Q., Deng, Y., Maute, A., Kilcommons, L. M., Knipp, D. J., & Hairston, M.
723 (2021, 5). Ashley: A new empirical model for the high-latitude electron
724 precipitation and electric field. *Space Weather*, *19*, 1-25. Retrieved from
725 <https://onlinelibrary.wiley.com/doi/10.1029/2020SW002671> doi:
726 [10.1029/2020SW002671](https://onlinelibrary.wiley.com/doi/10.1029/2020SW002671)
- 727
728 Zhu, Q., Deng, Y., Maute, A., Sheng, C., & Lin, C. Y. (2017, 6). Impact of the
729 vertical dynamics on the thermosphere at low and middle latitudes: Gitm
730 simulations. *Journal of Geophysical Research: Space Physics*, *122*, 6882-
731 6891. Retrieved from [https://onlinelibrary.wiley.com/doi/10.1002/](https://onlinelibrary.wiley.com/doi/10.1002/2017JA024891)

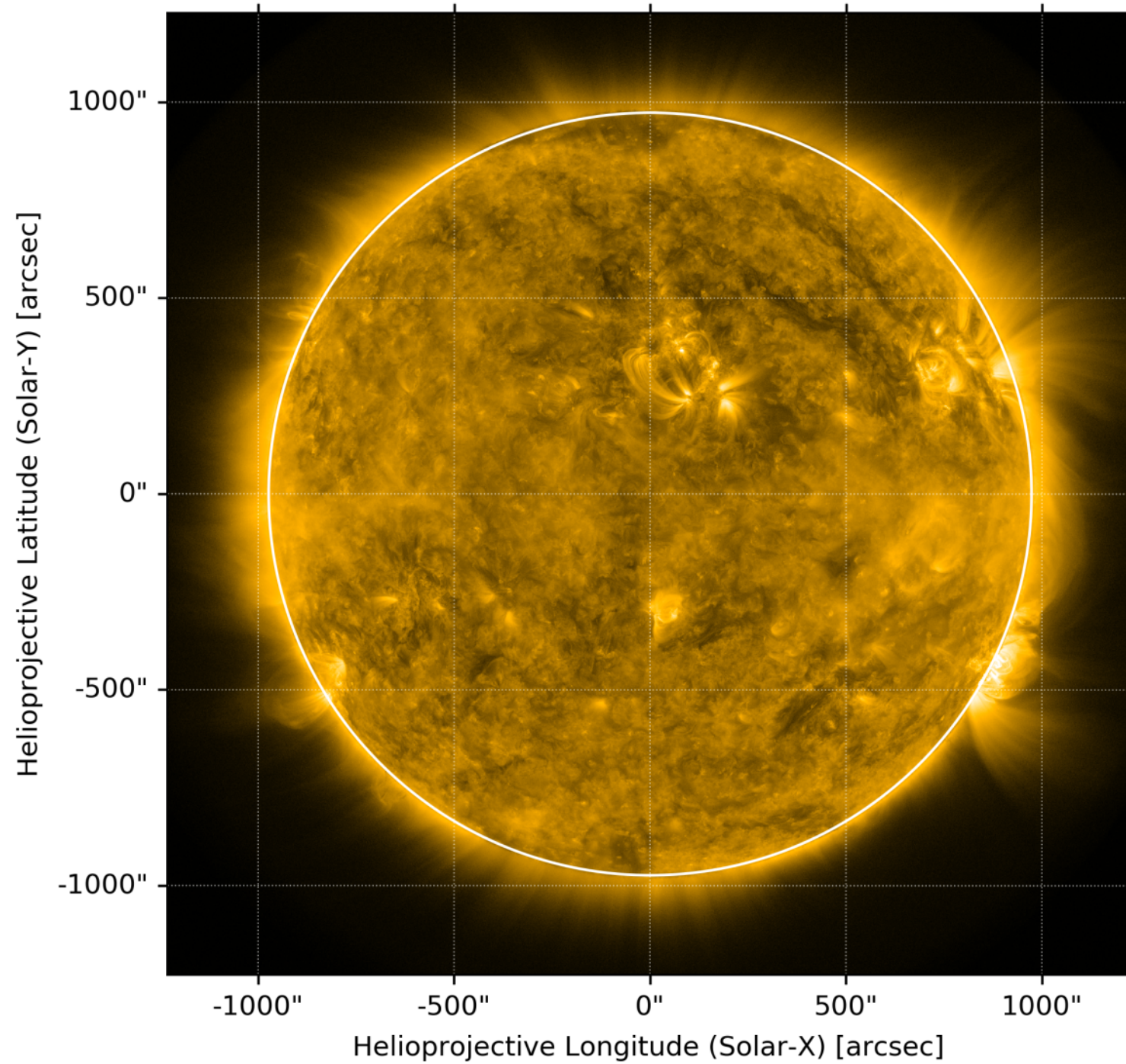
732 2017JA023939 doi: 10.1002/2017JA023939
733 Zhu, Q., Deng, Y., Richmond, A., McGranaghan, R. M., & Maute, A. (2019, 5).
734 Impacts of multiscale facs on the ionosphere-thermosphere system: Gitm
735 simulation. *Journal of Geophysical Research: Space Physics*, 124, 3532-
736 3542. Retrieved from [https://onlinelibrary.wiley.com/doi/10.1029/
737 2018JA026082](https://onlinelibrary.wiley.com/doi/10.1029/2018JA026082) doi: 10.1029/2018JA026082

Figure 1.

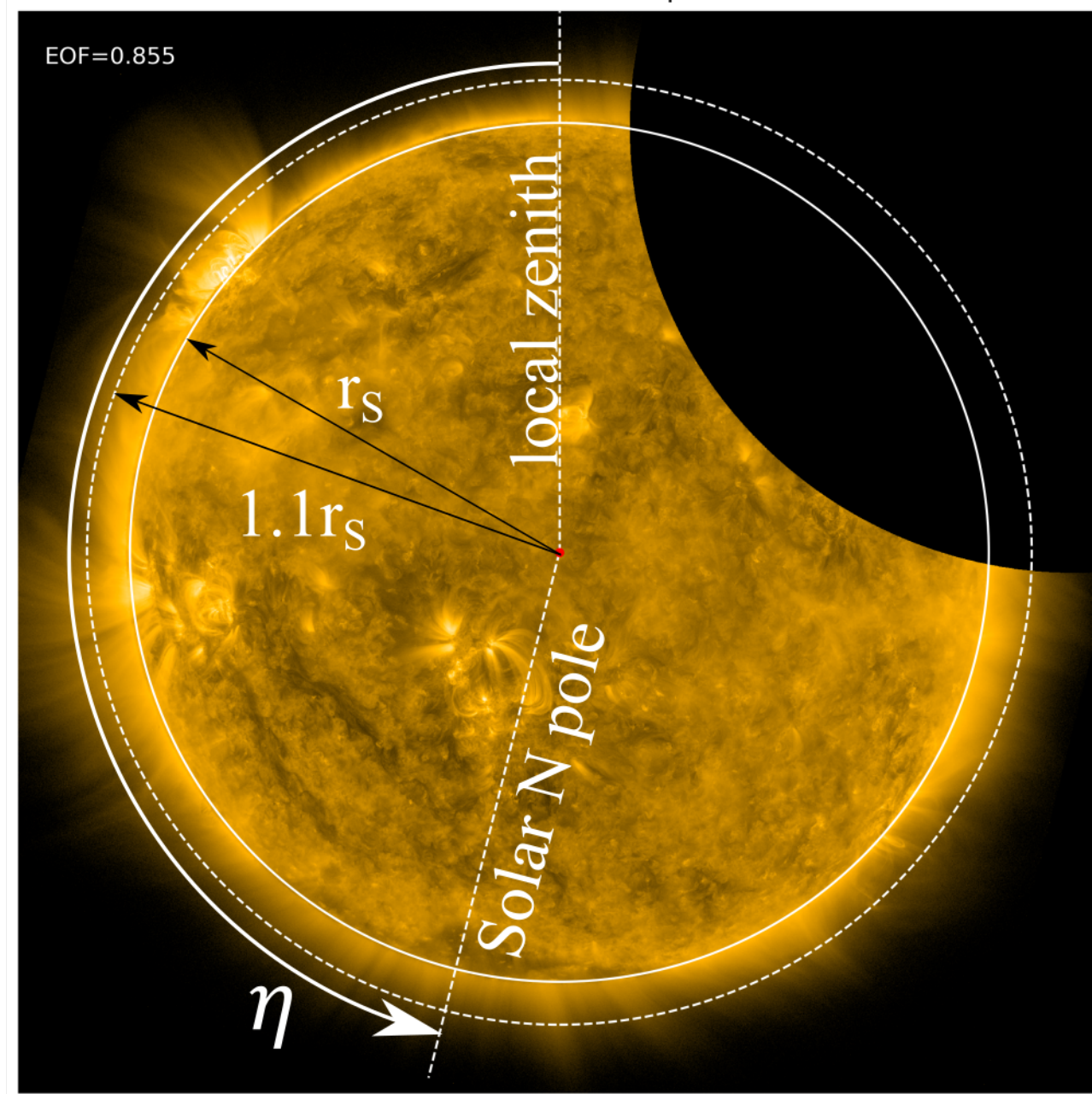
SUVI 171 Å 2021-12-04 08:28:31



AIA 171 Å 2021-12-04 08:30:09



SDO AIA 171 Å Eclipse



Geometrically Symmetric Eclipse

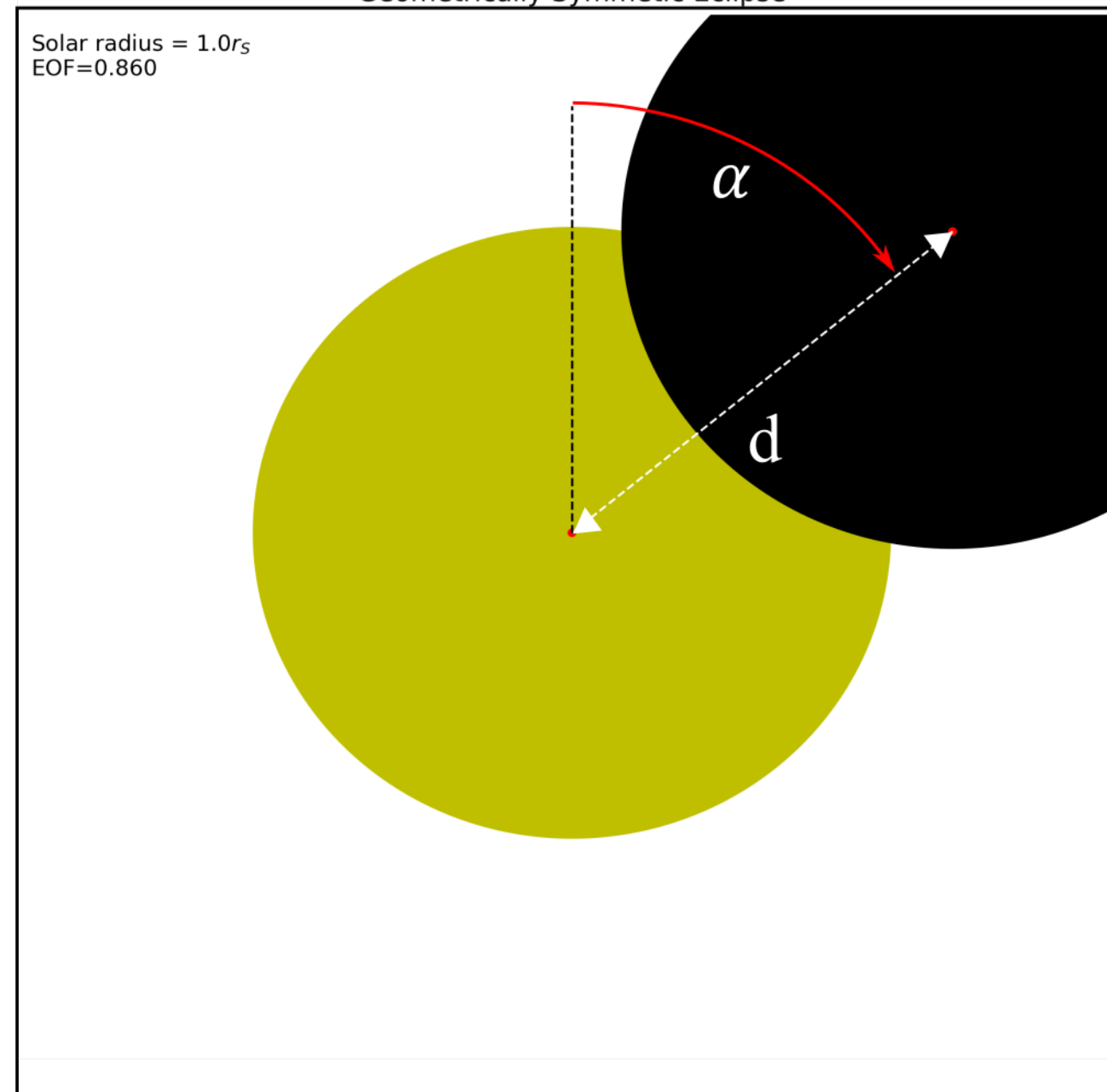
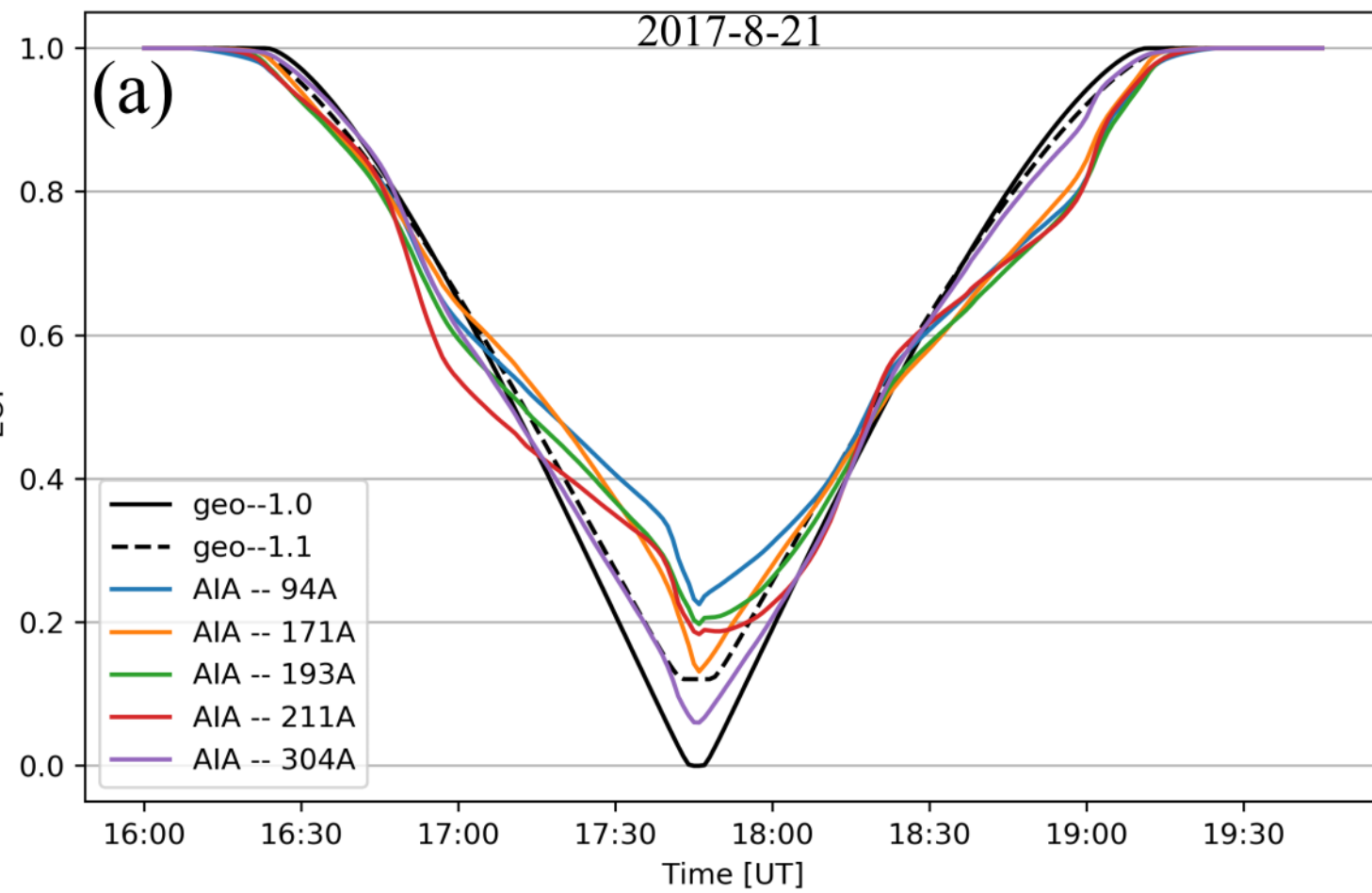
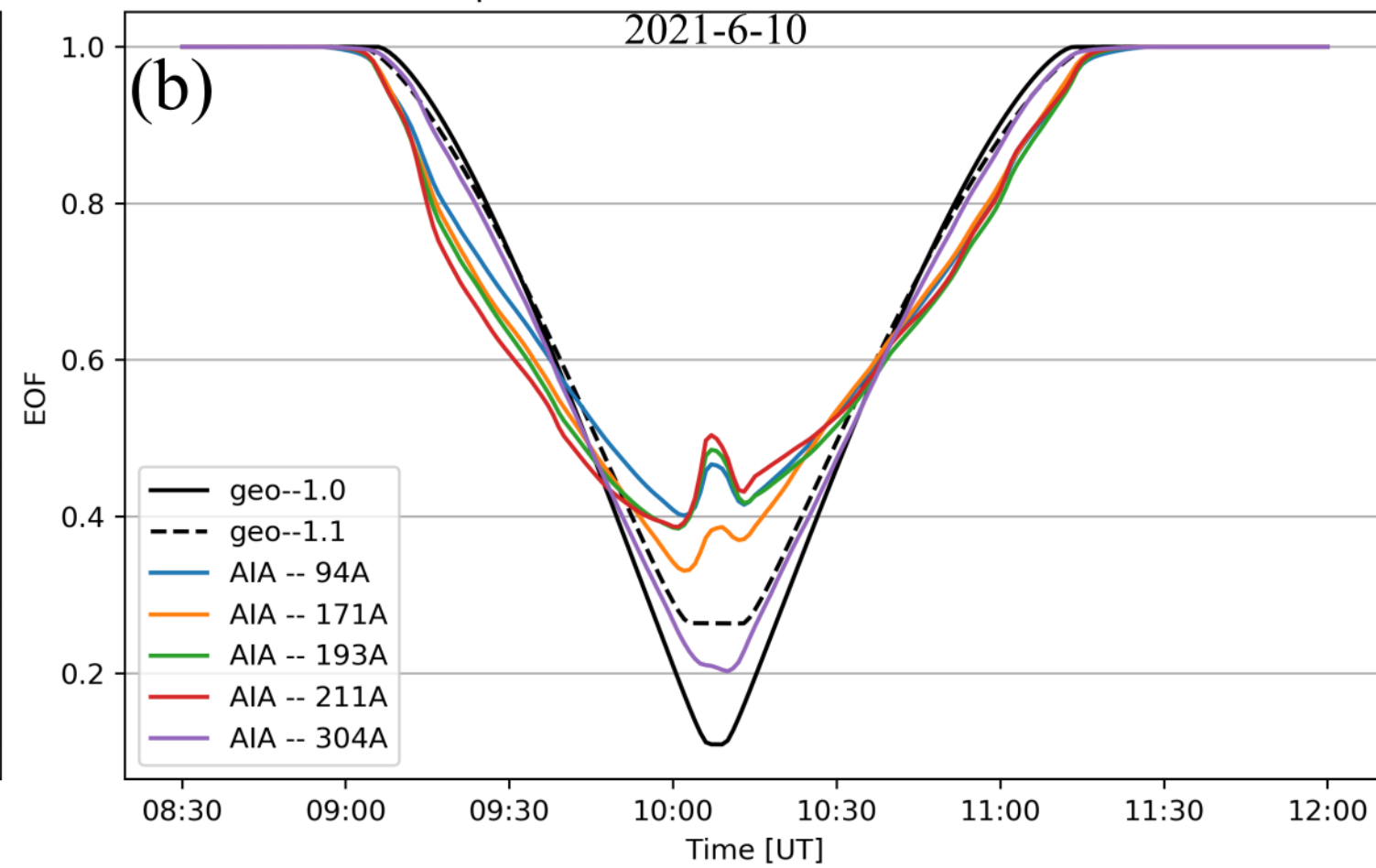


Figure 3.

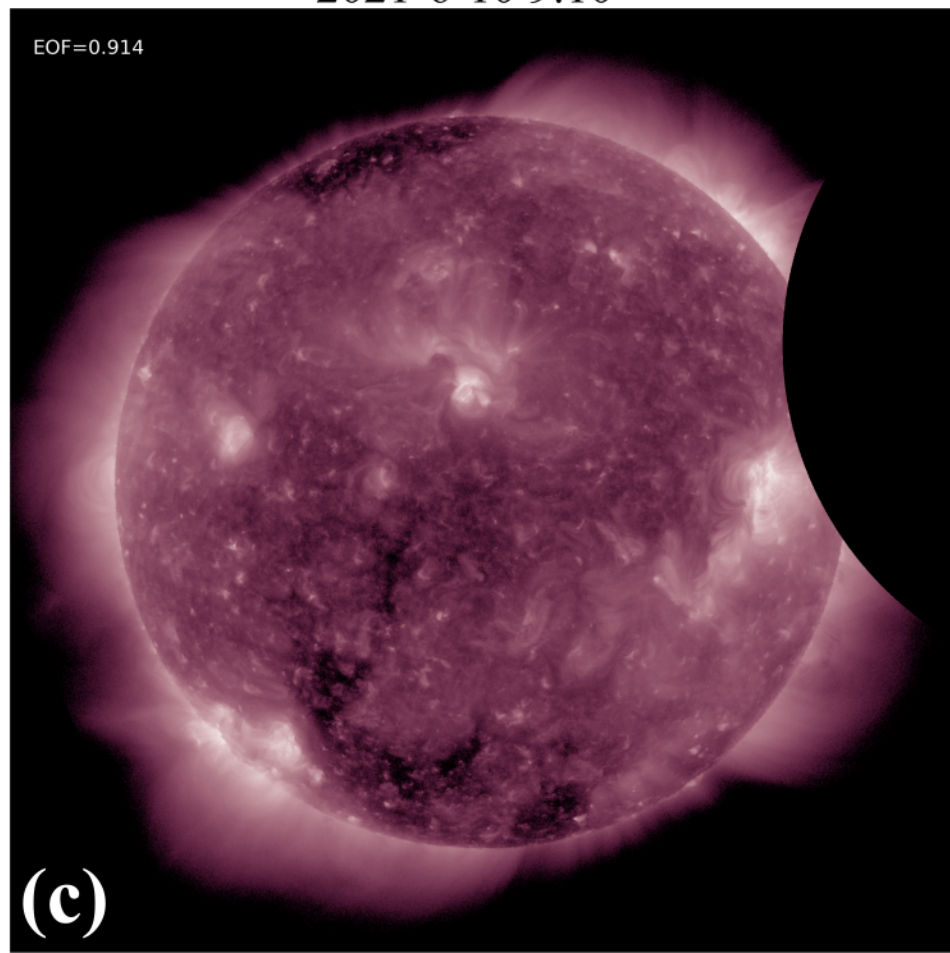
Lusk, ID: 105.4W, 42.76N, 0km



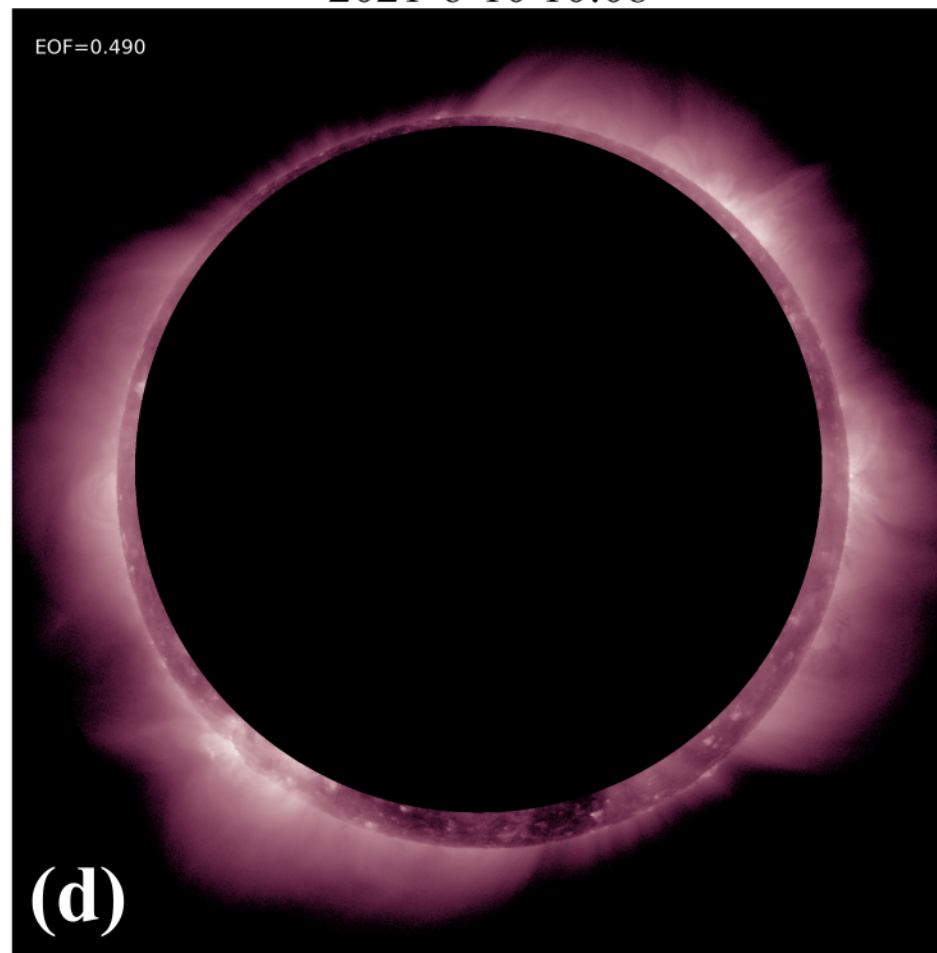
Iqaluit, Canada: 68.5W, 63.7N, 0km



2021-6-10 9:10



2021-6-10 10:08



2021-6-10 11:15

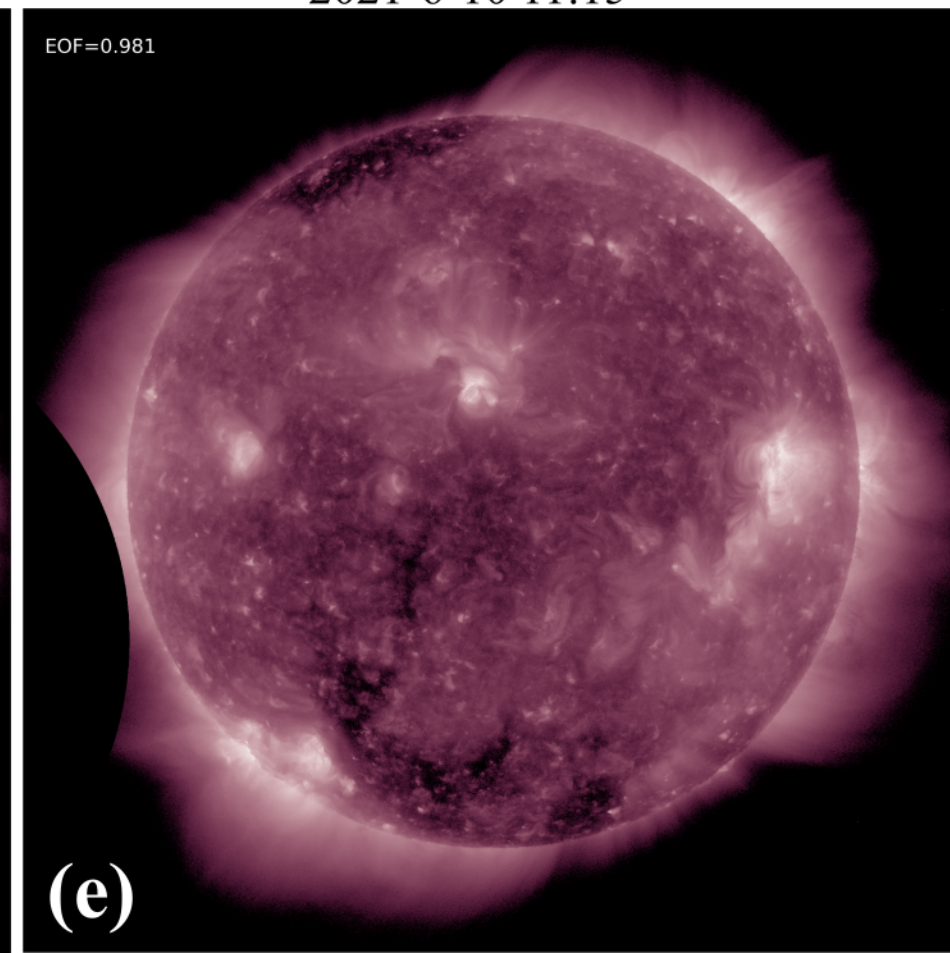
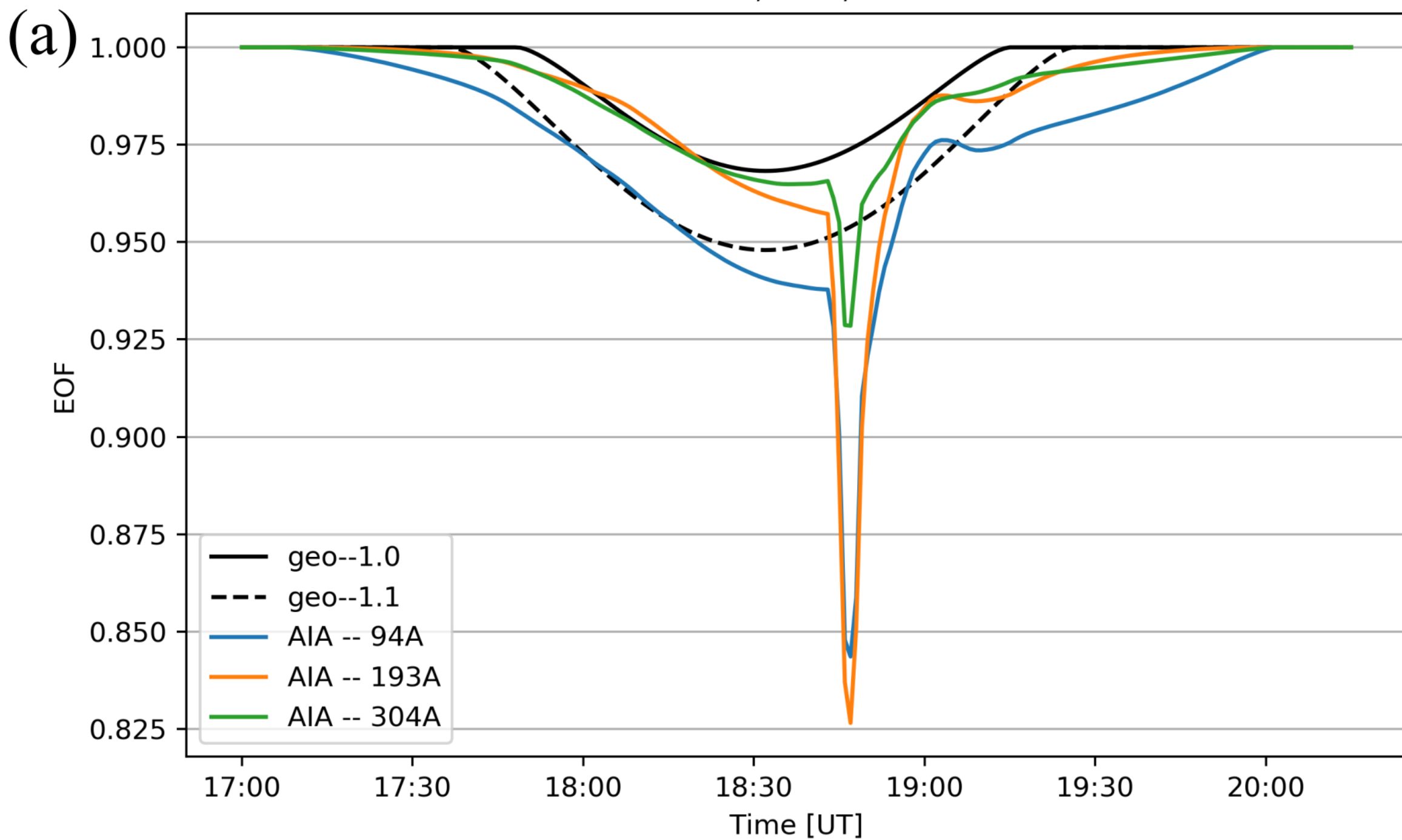


Figure 4.

100W, 10N, 0km



SDO AIA 193A

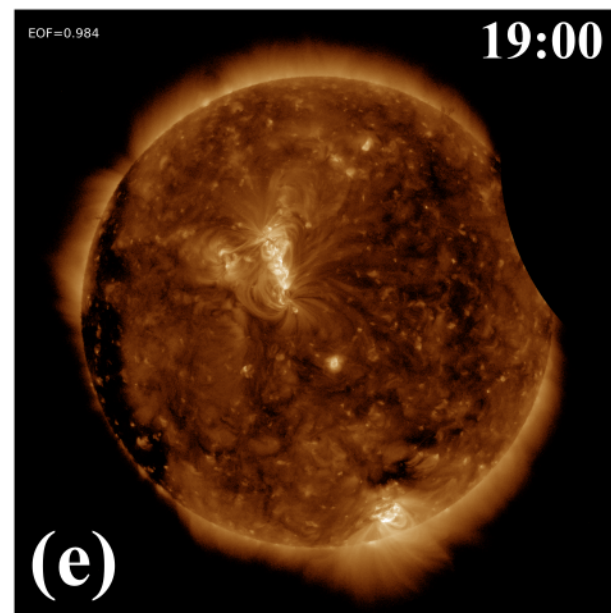
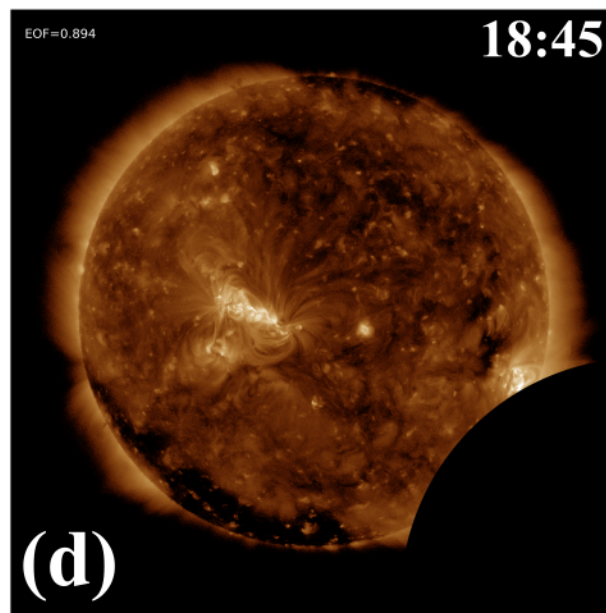
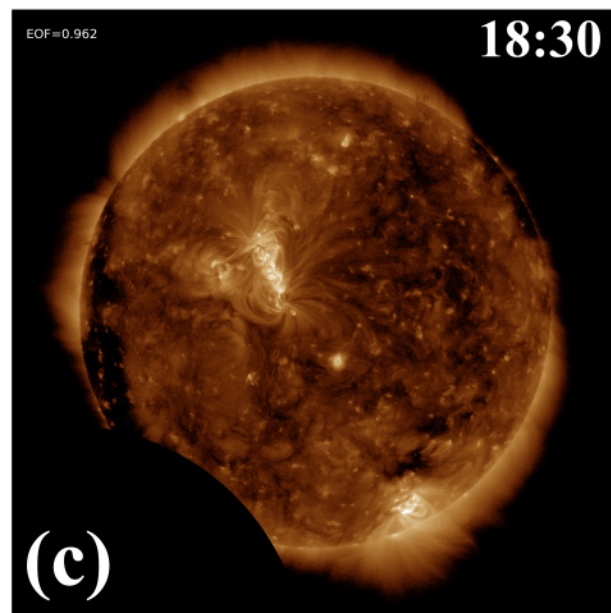
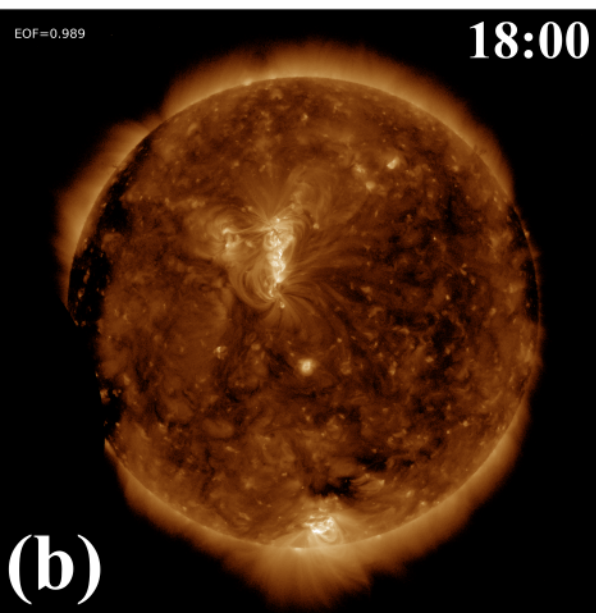
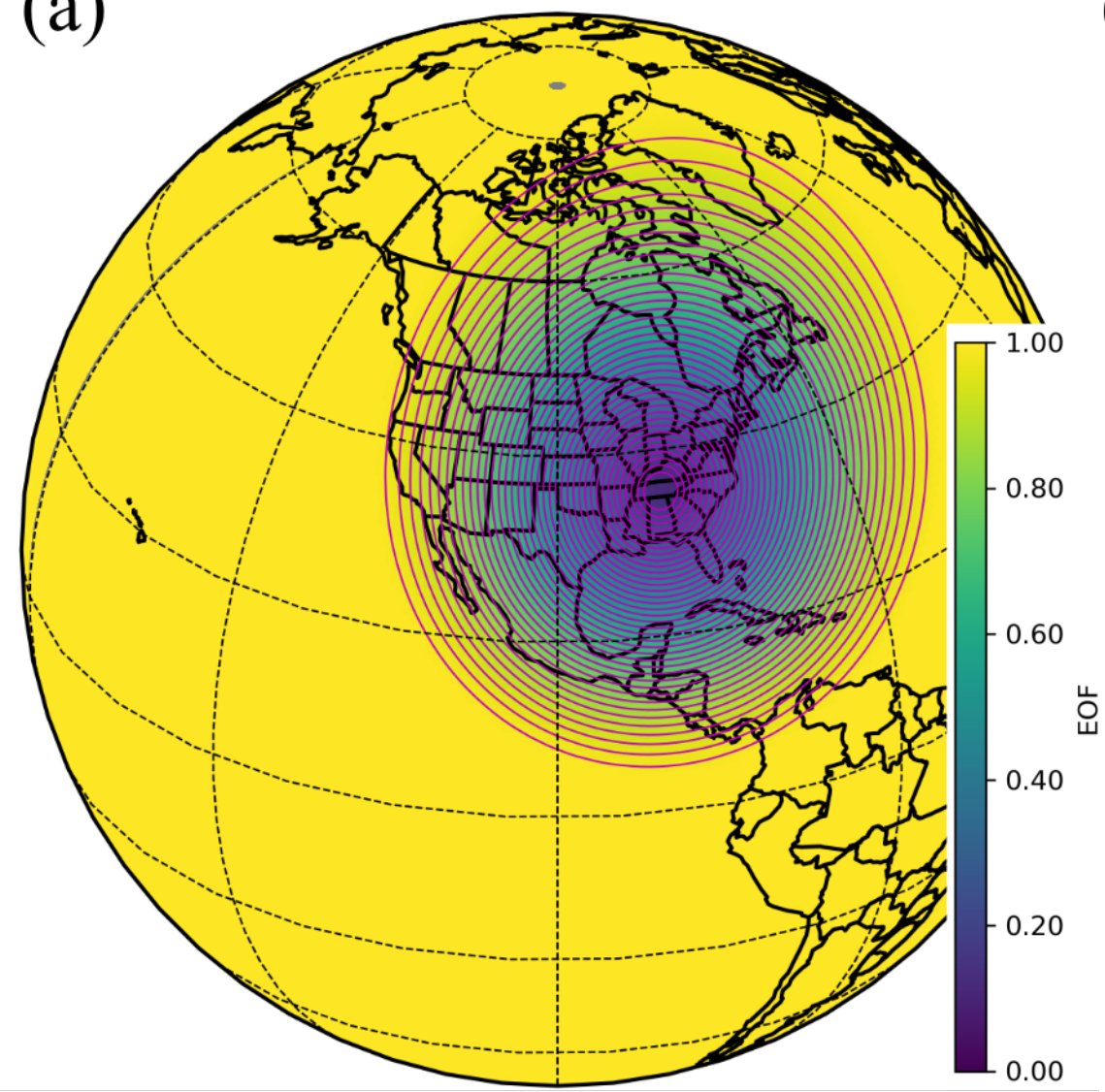
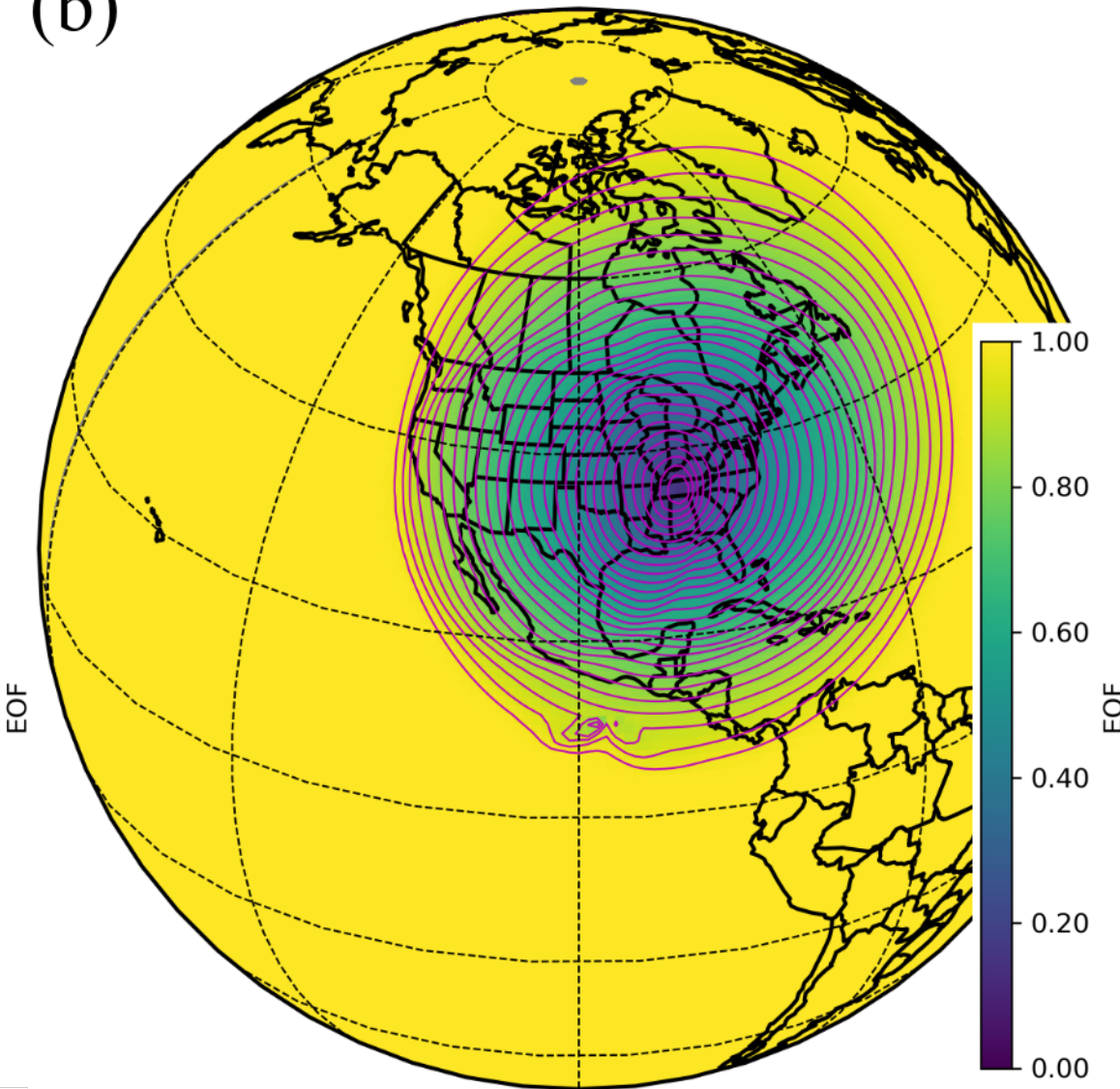


Figure 5.

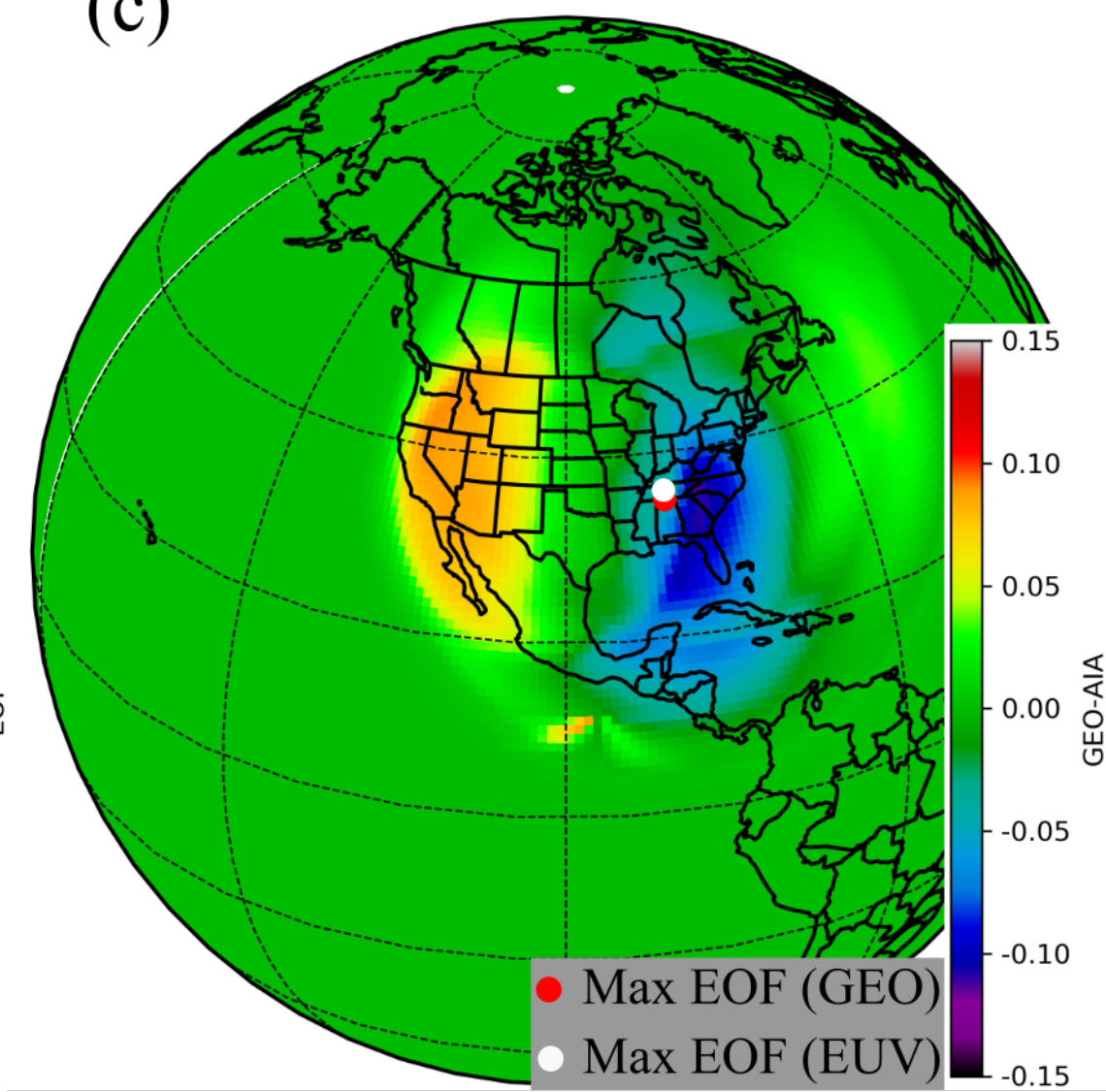
(a) 2017-08-21 18:30:00, Alt = 150 km



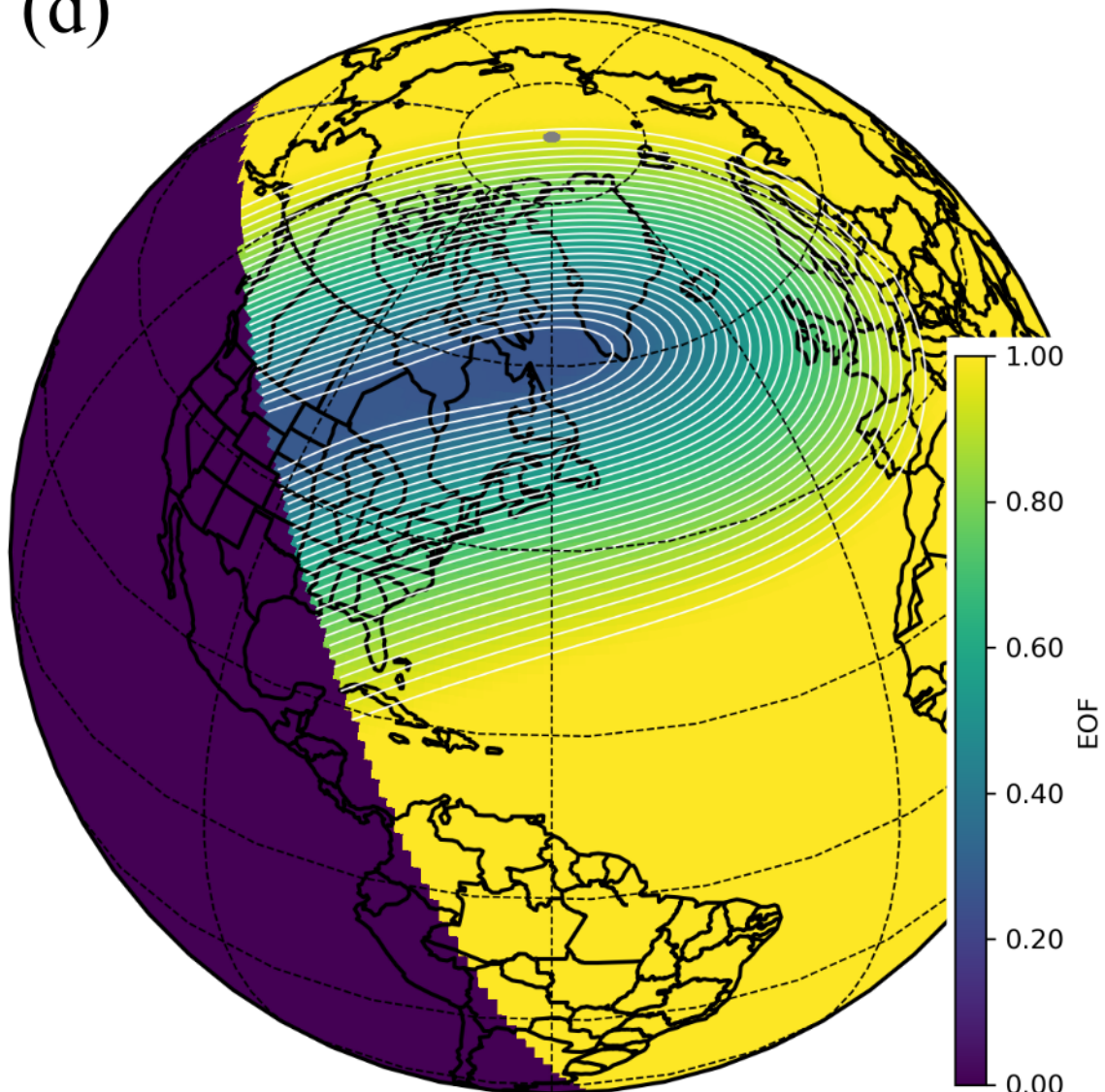
(b) 2017-08-21 18:30:00, Alt = 150 km



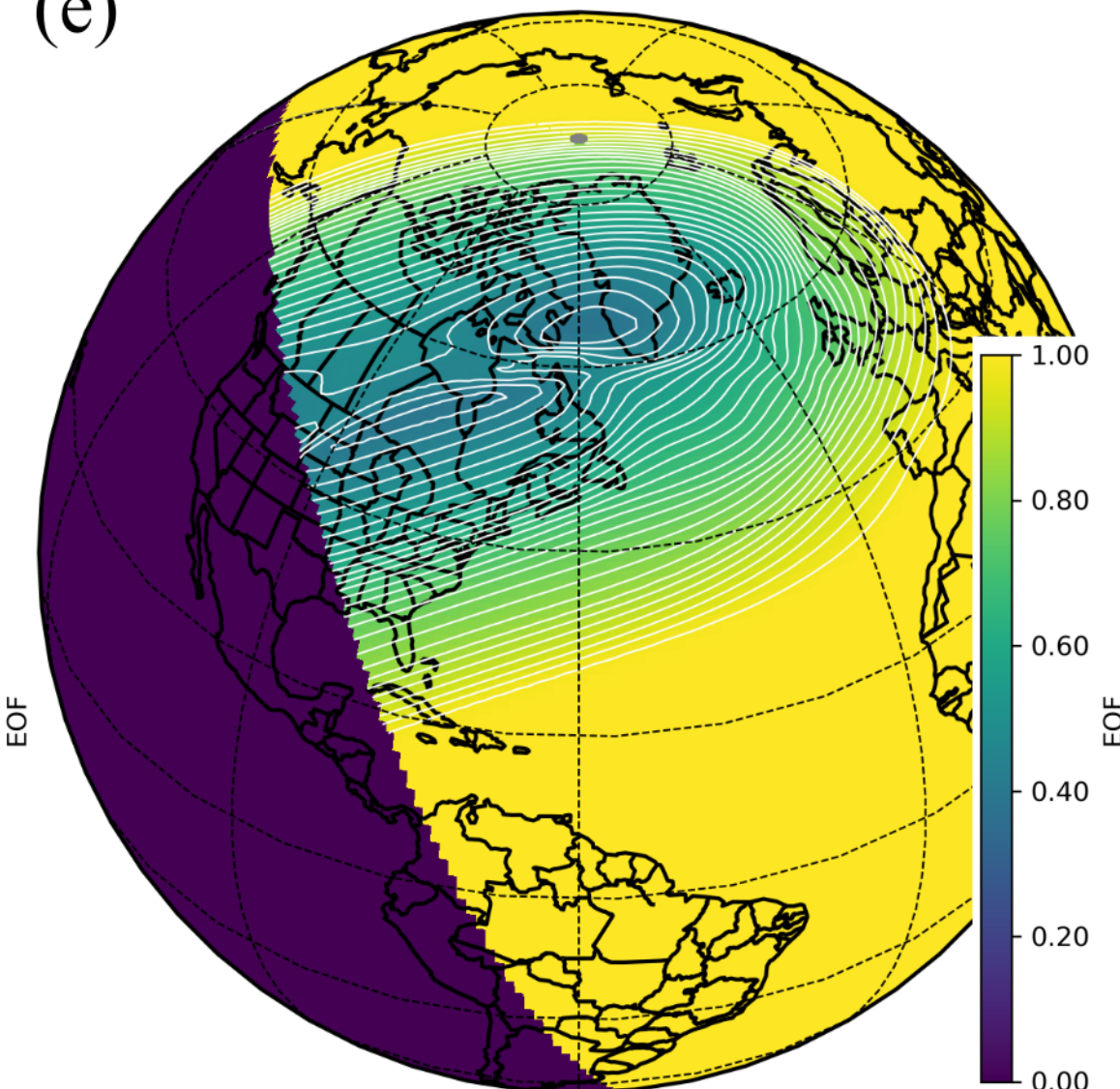
(c) 2017-08-21 18:30:00



(d) 2021-06-10 10:00:00, Alt = 150 km



(e) 2021-06-10 10:00:00, Alt = 150 km



(f) 2021-06-10 10:00:00

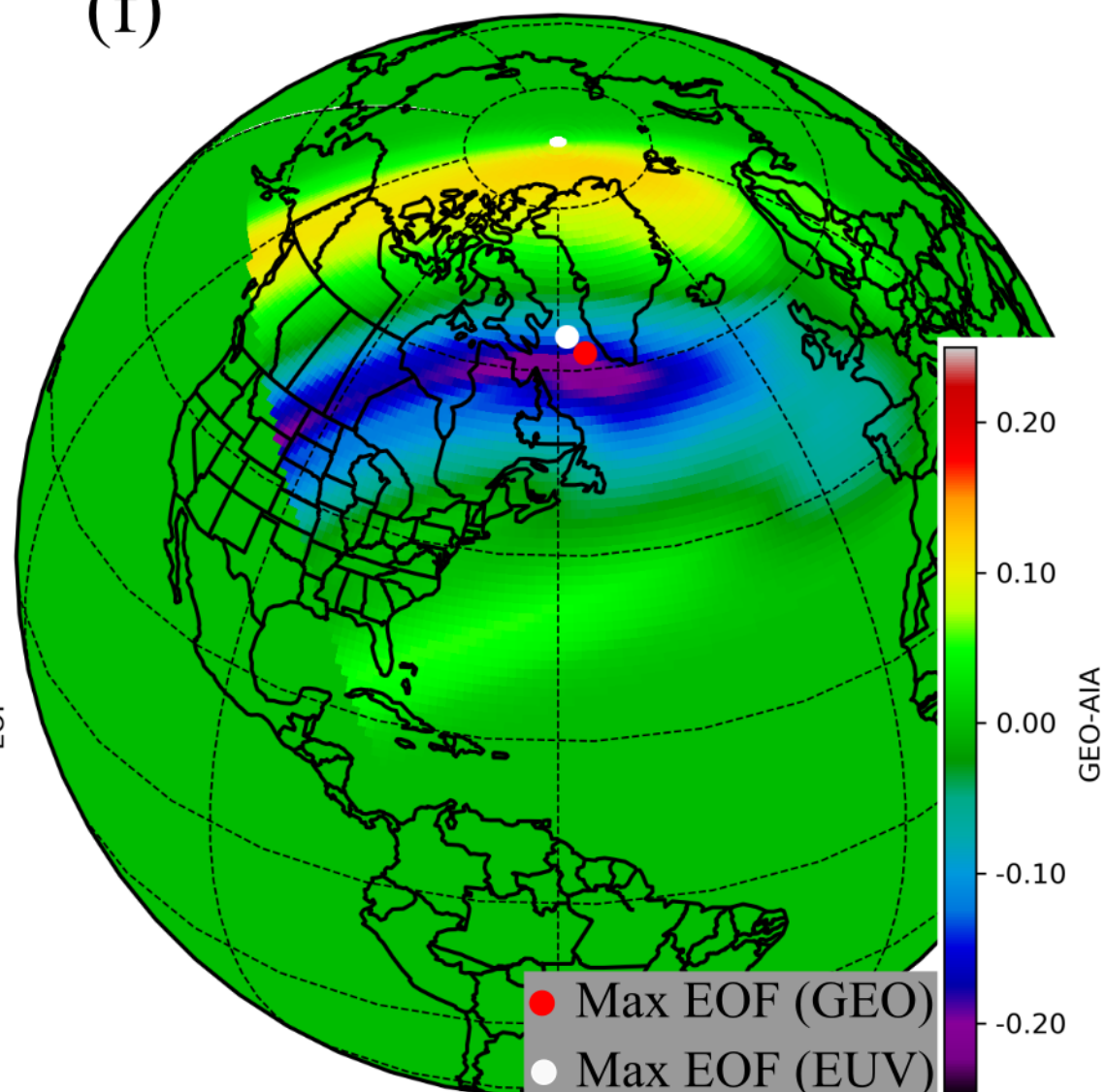
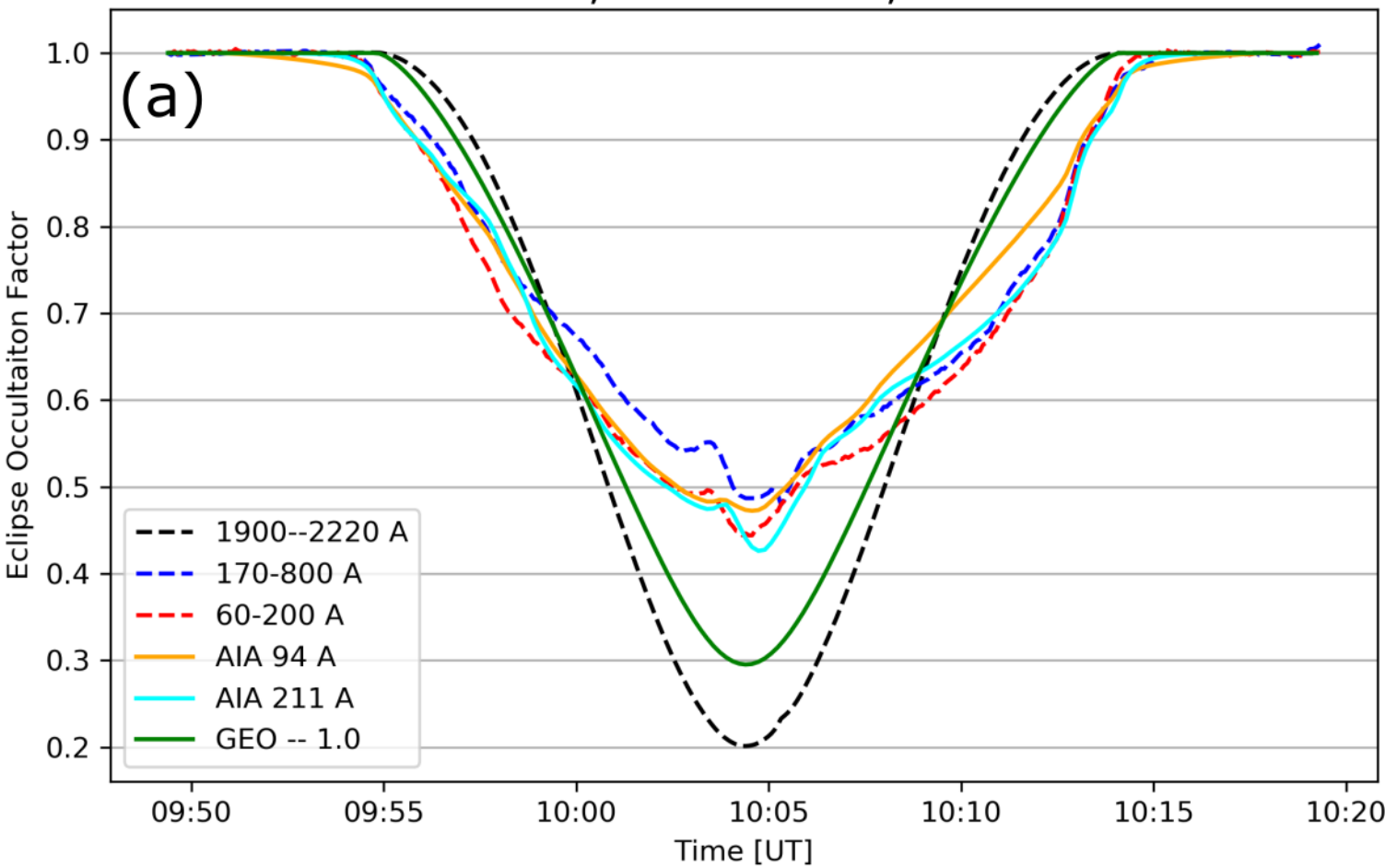


Figure 6.

Figure 7.

PROBA2, 2021-06-10, Pass #2



PROBA2, 2021-12-04, Pass #2

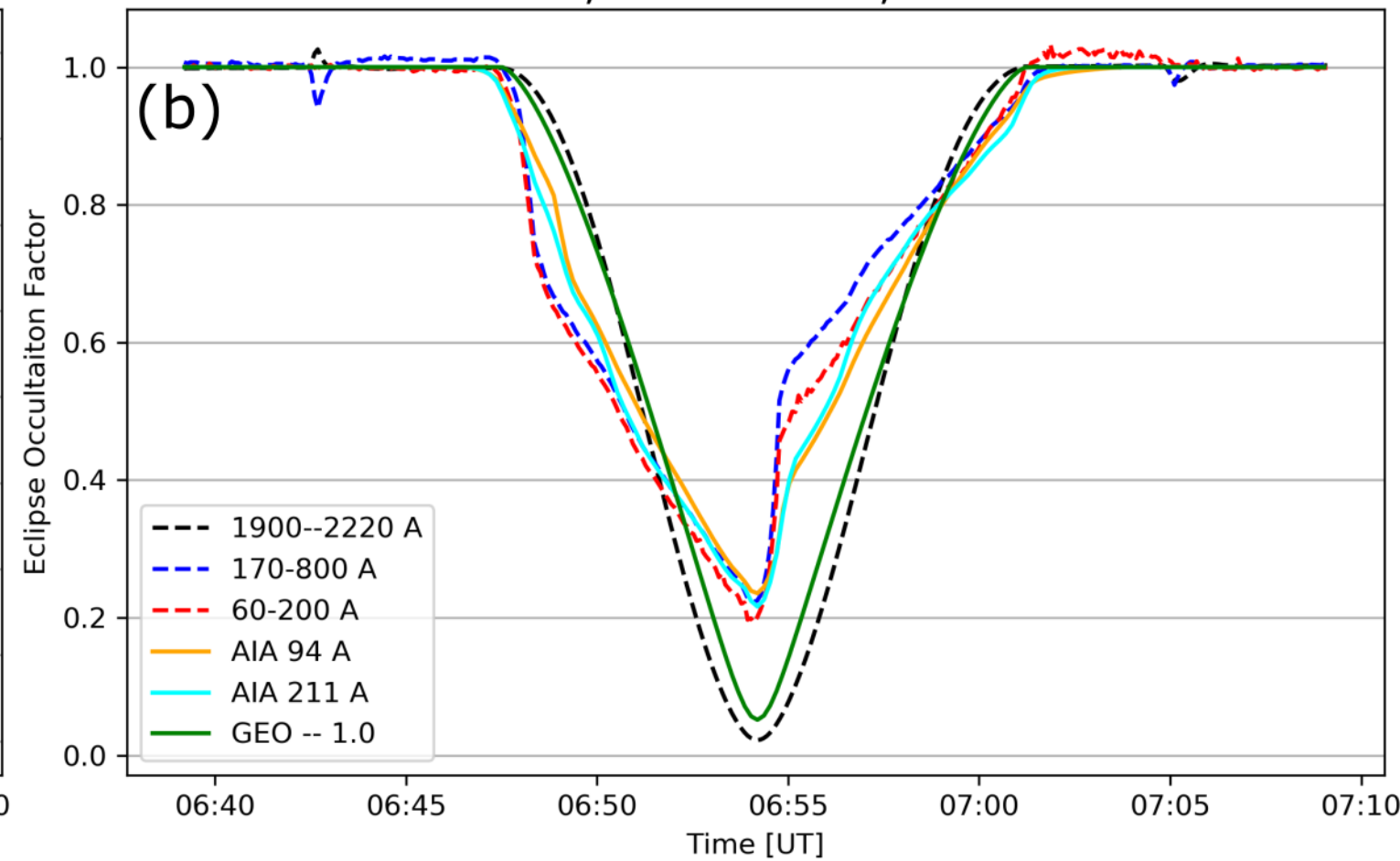


Figure 8.

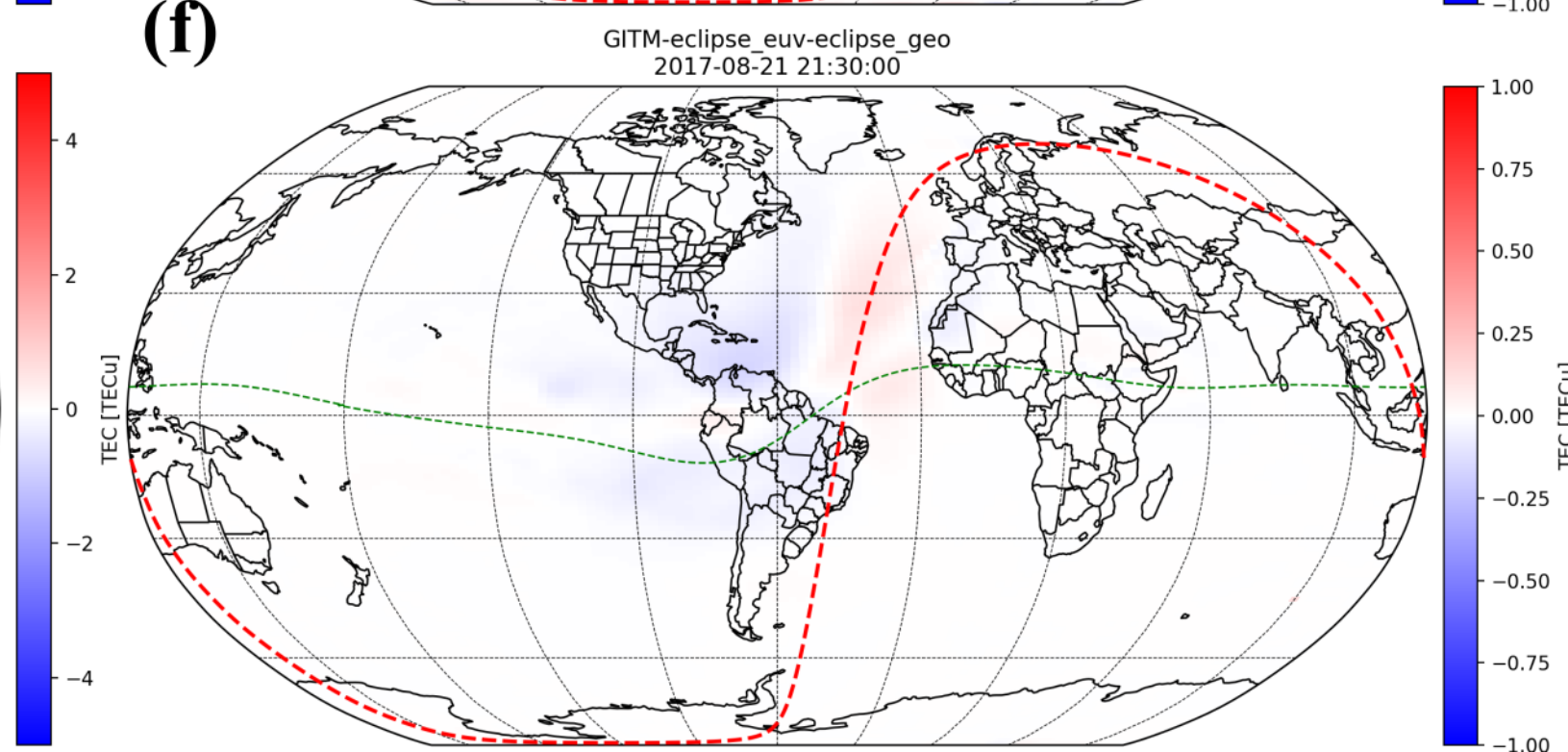
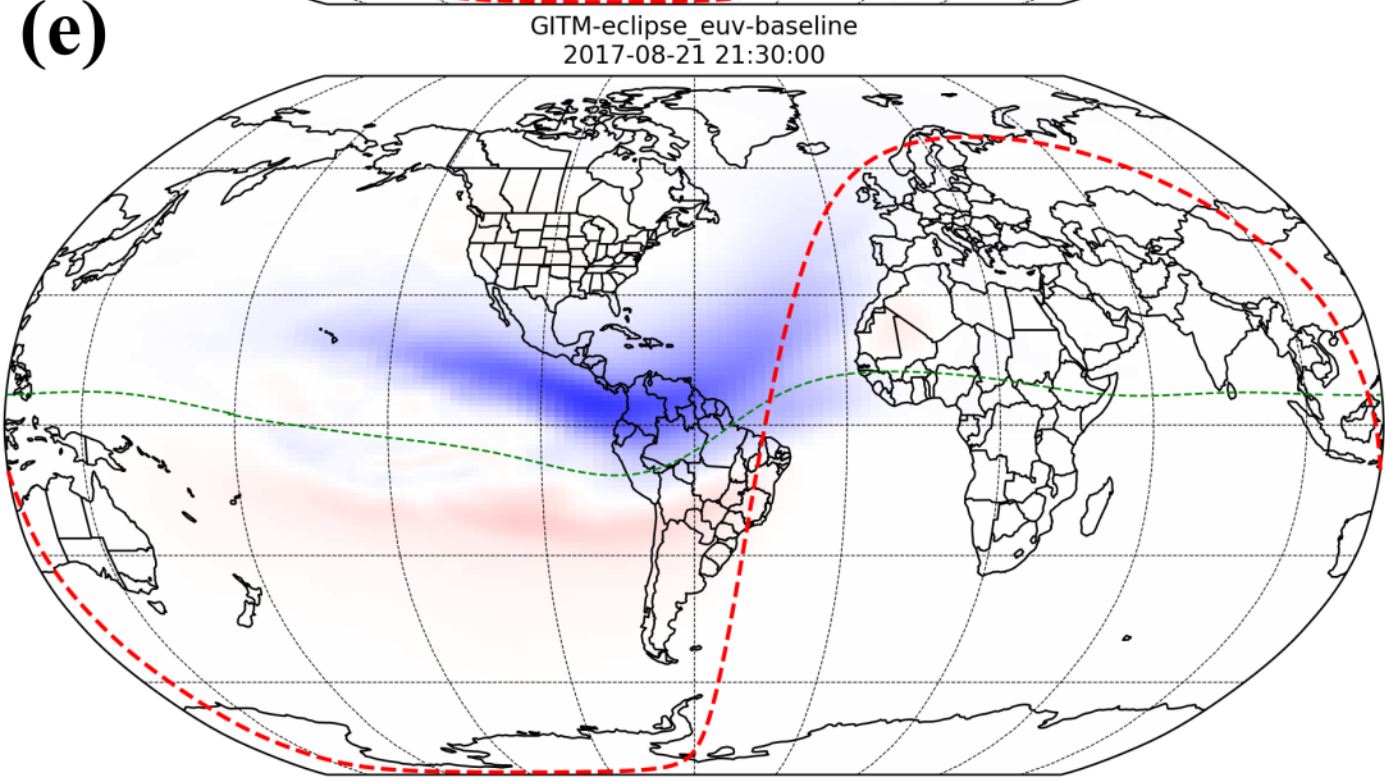
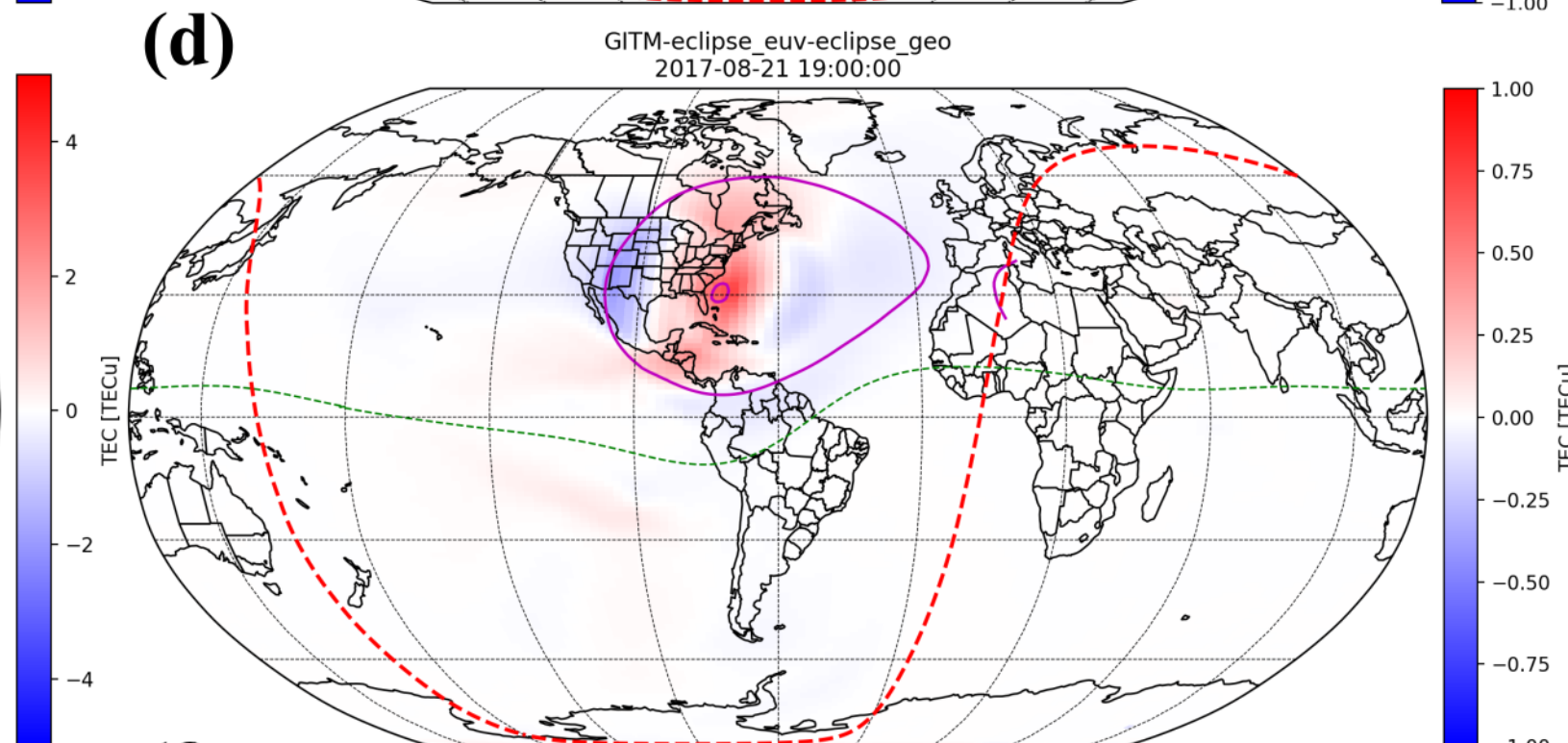
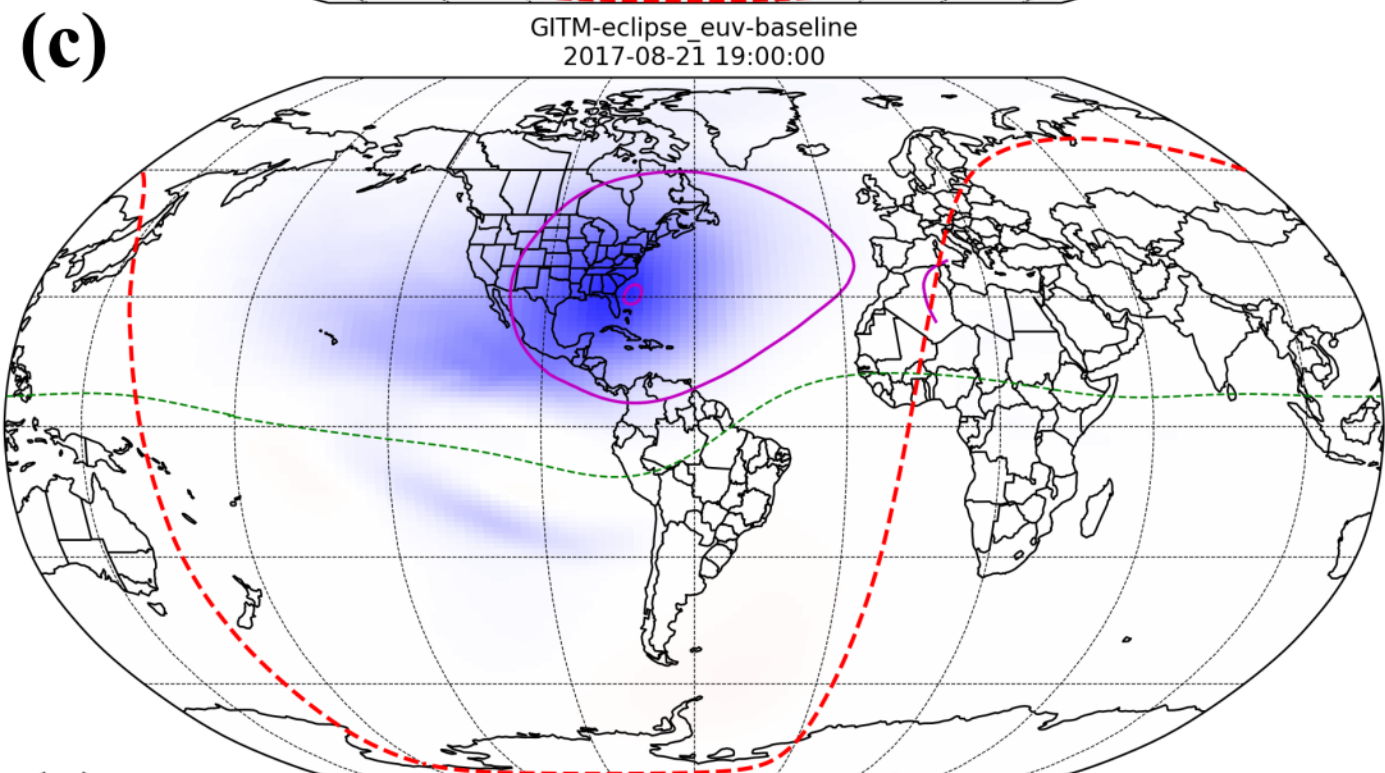
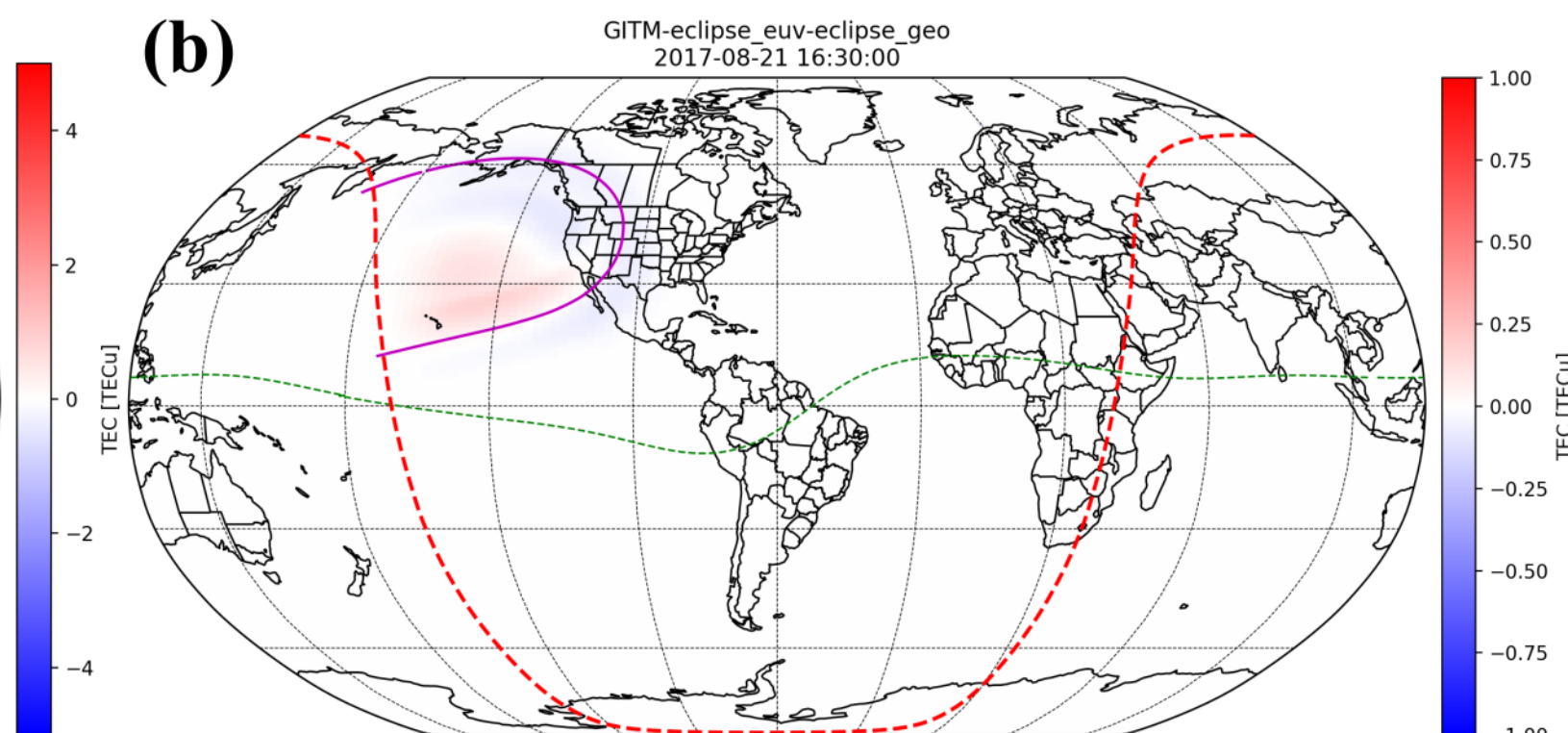
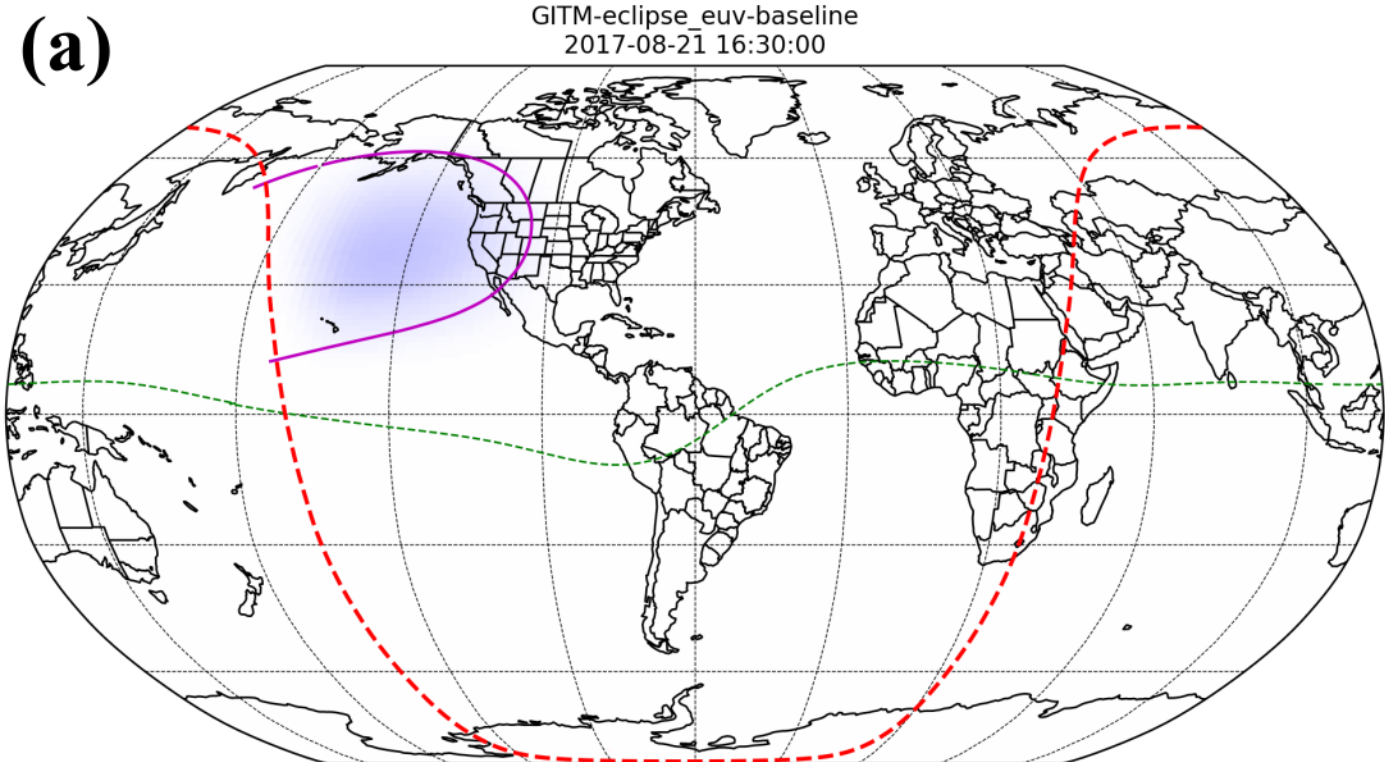


Figure 9.

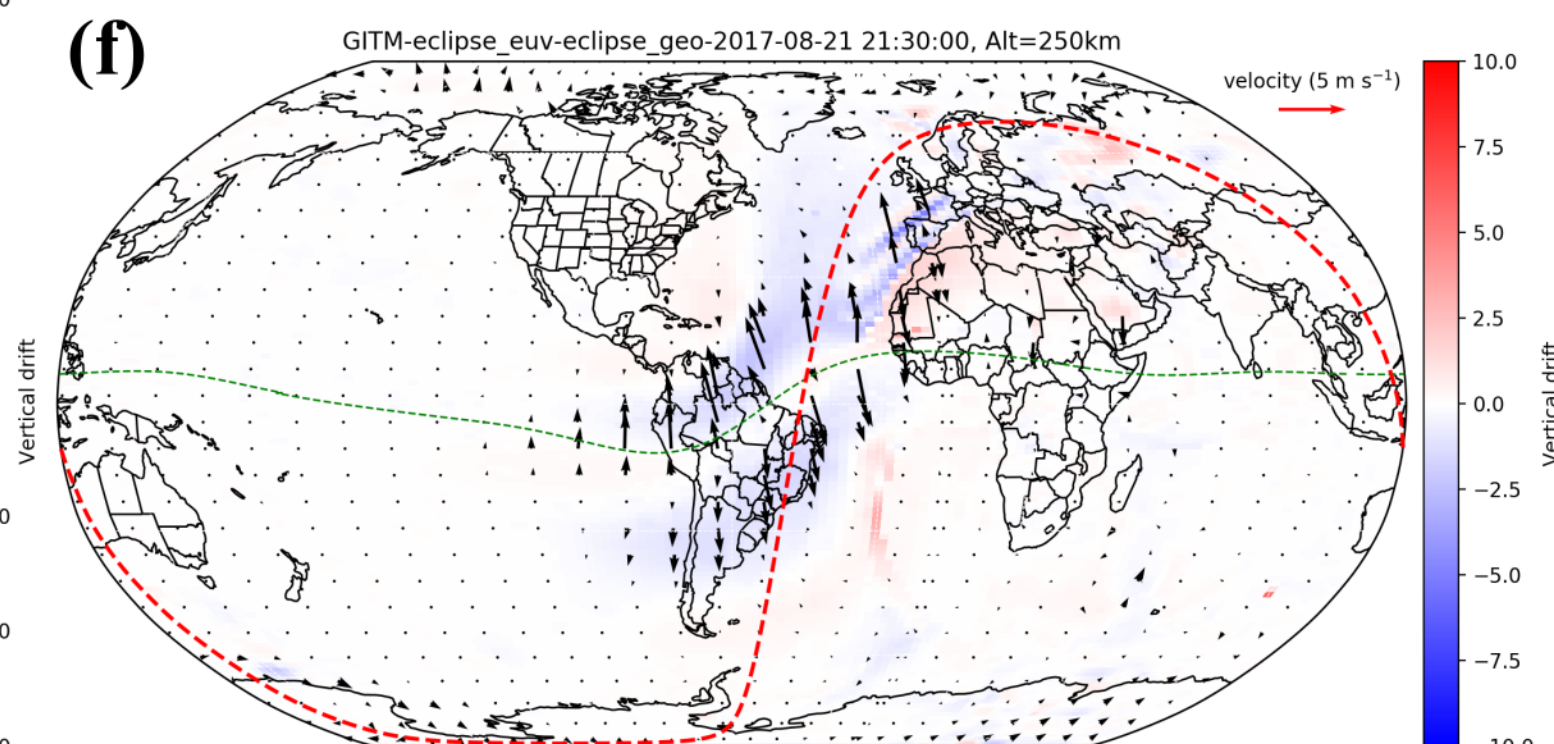
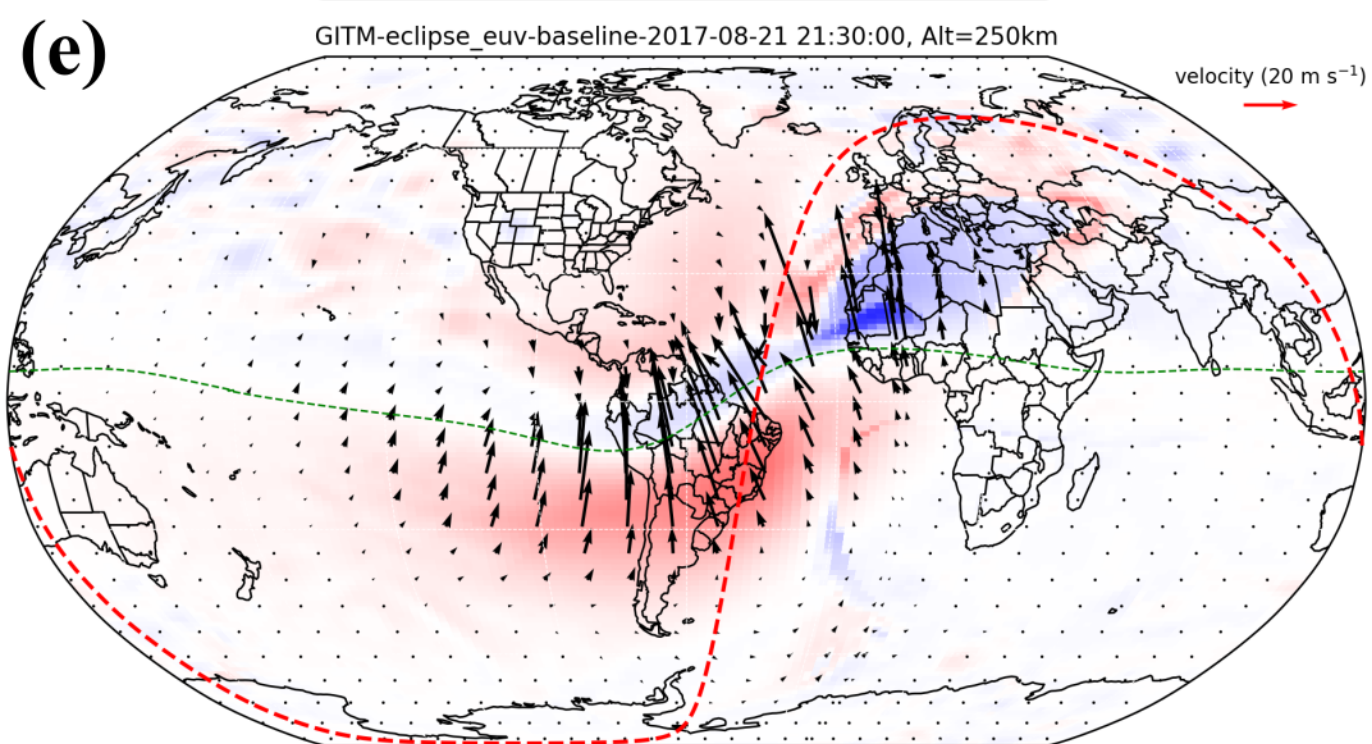
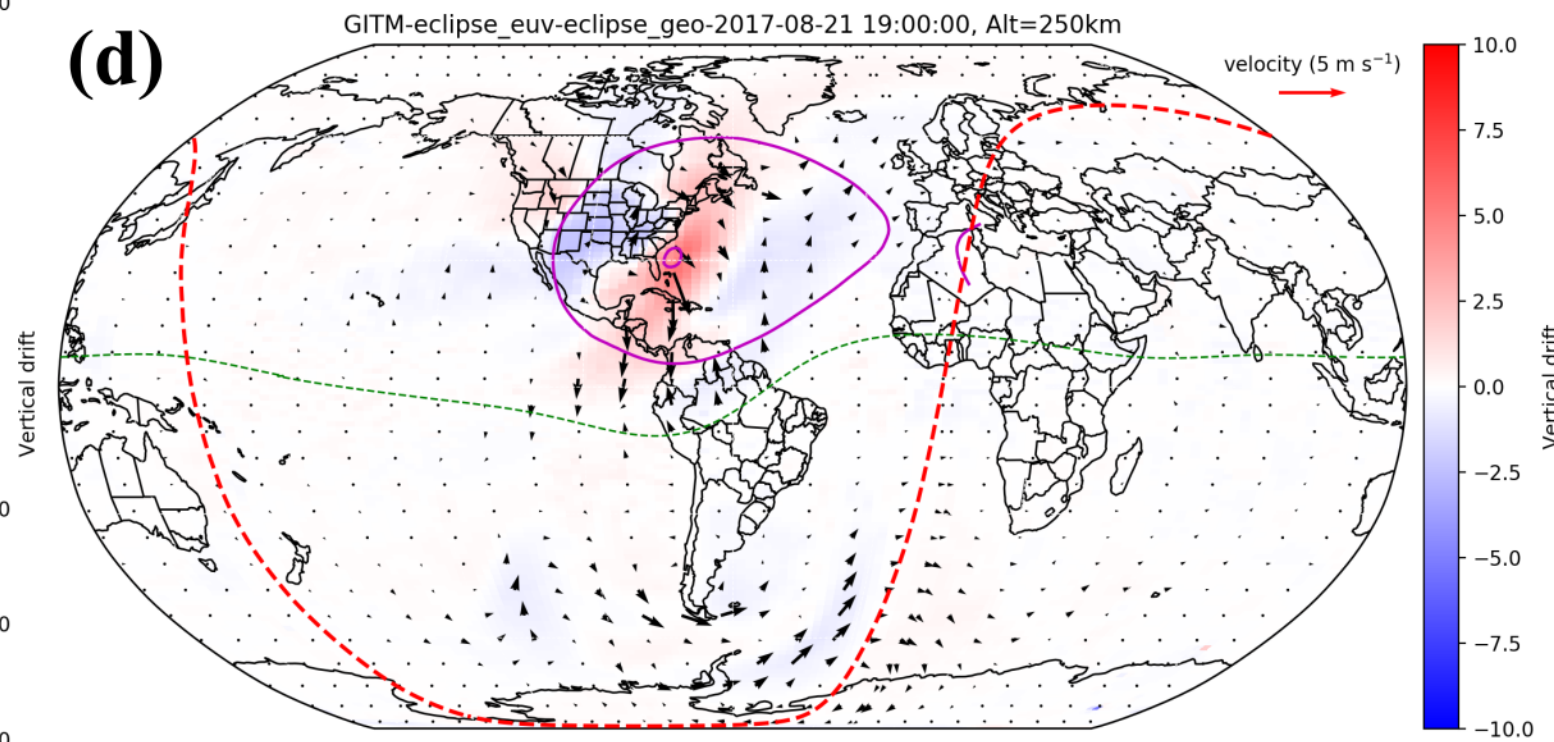
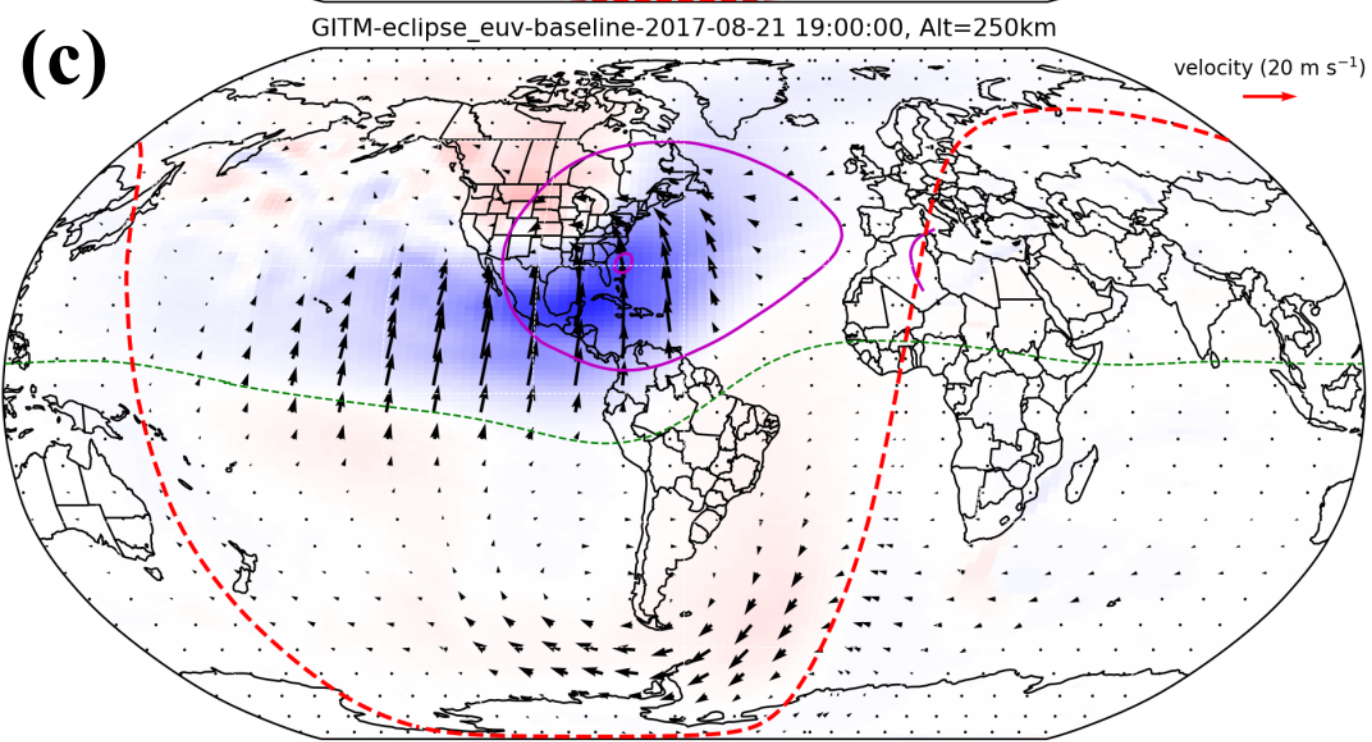
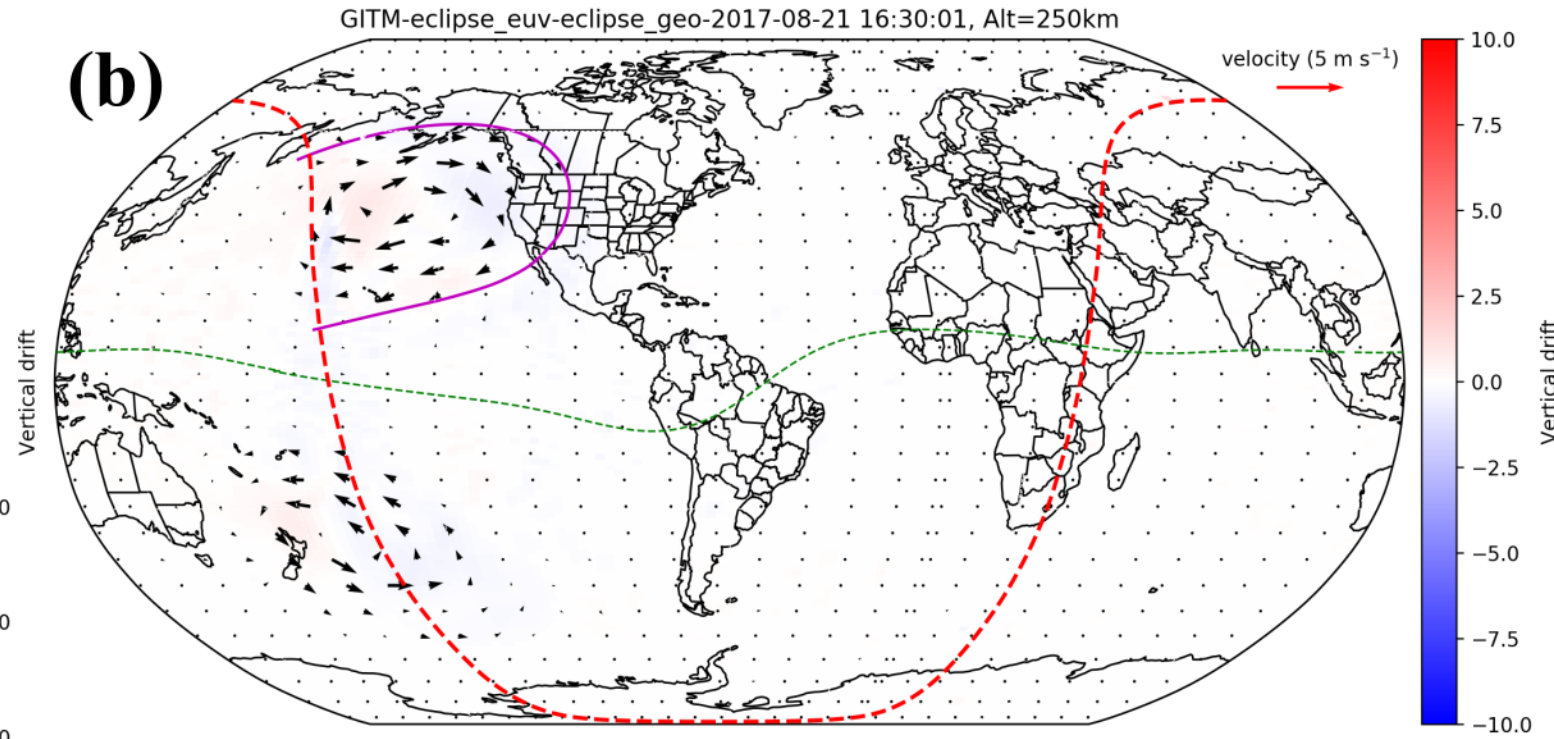
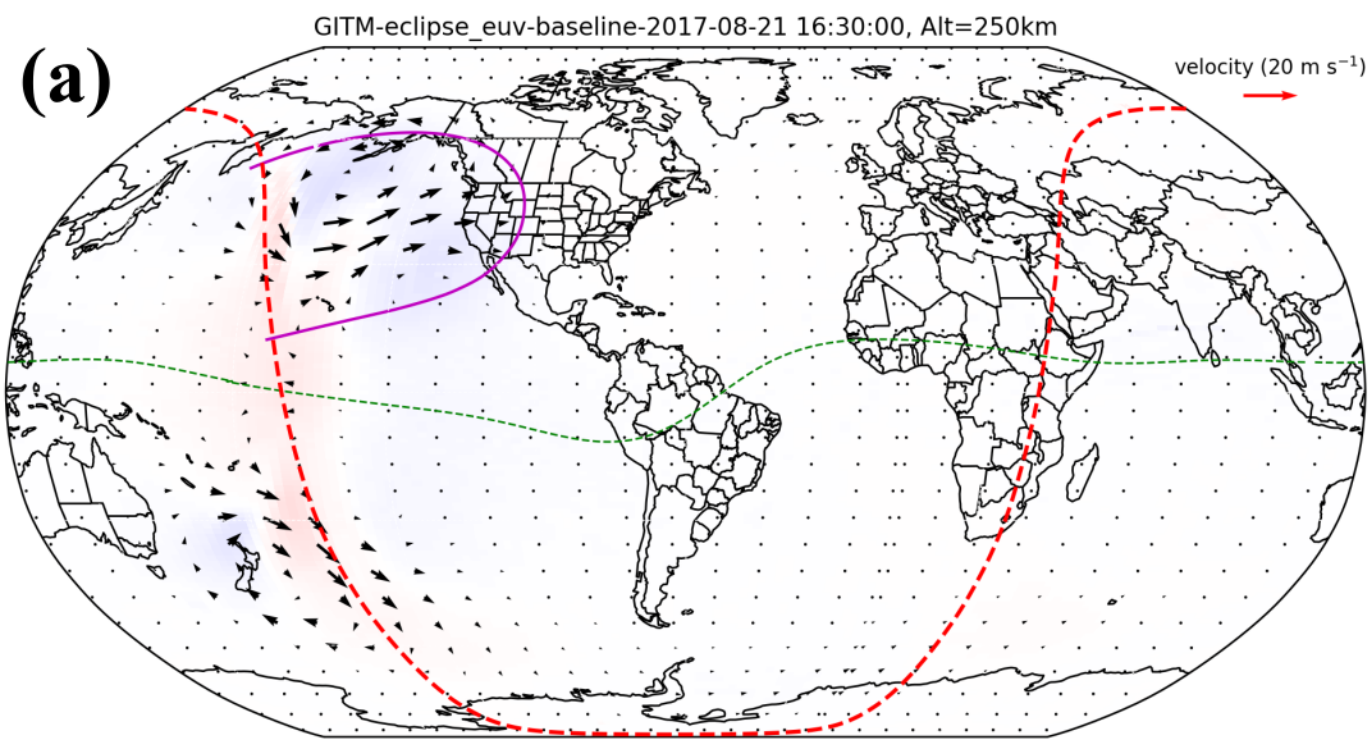


Figure 10.

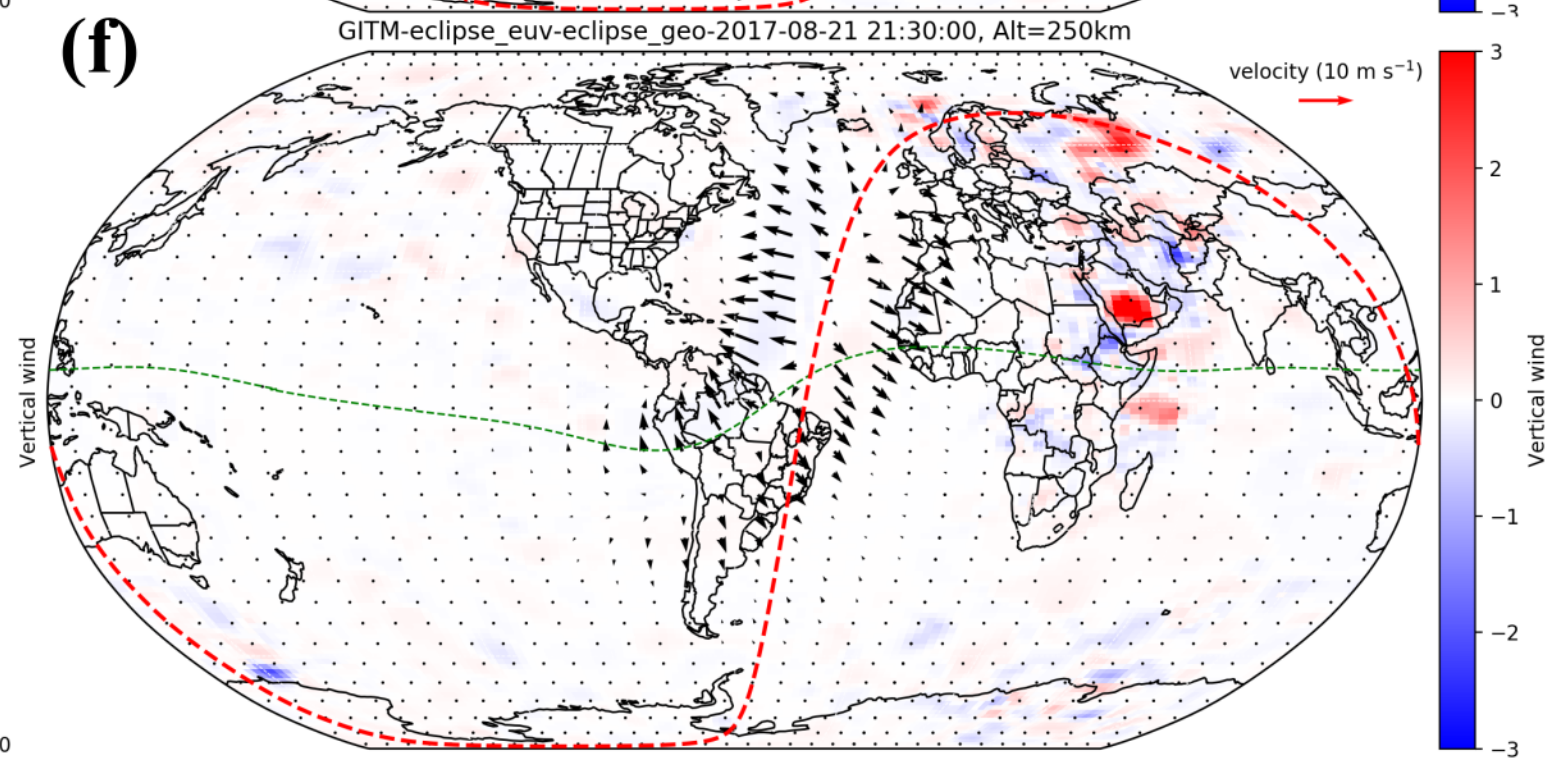
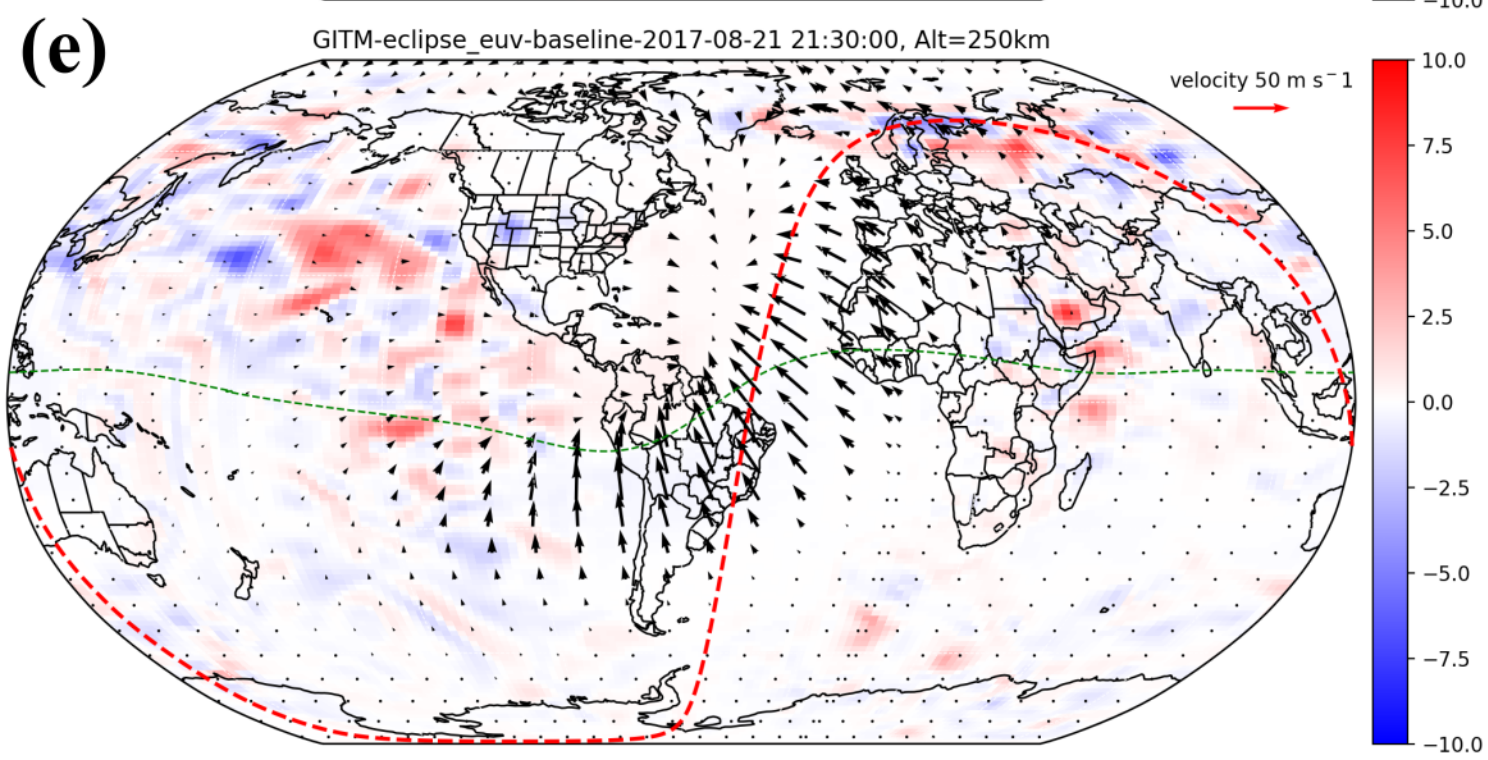
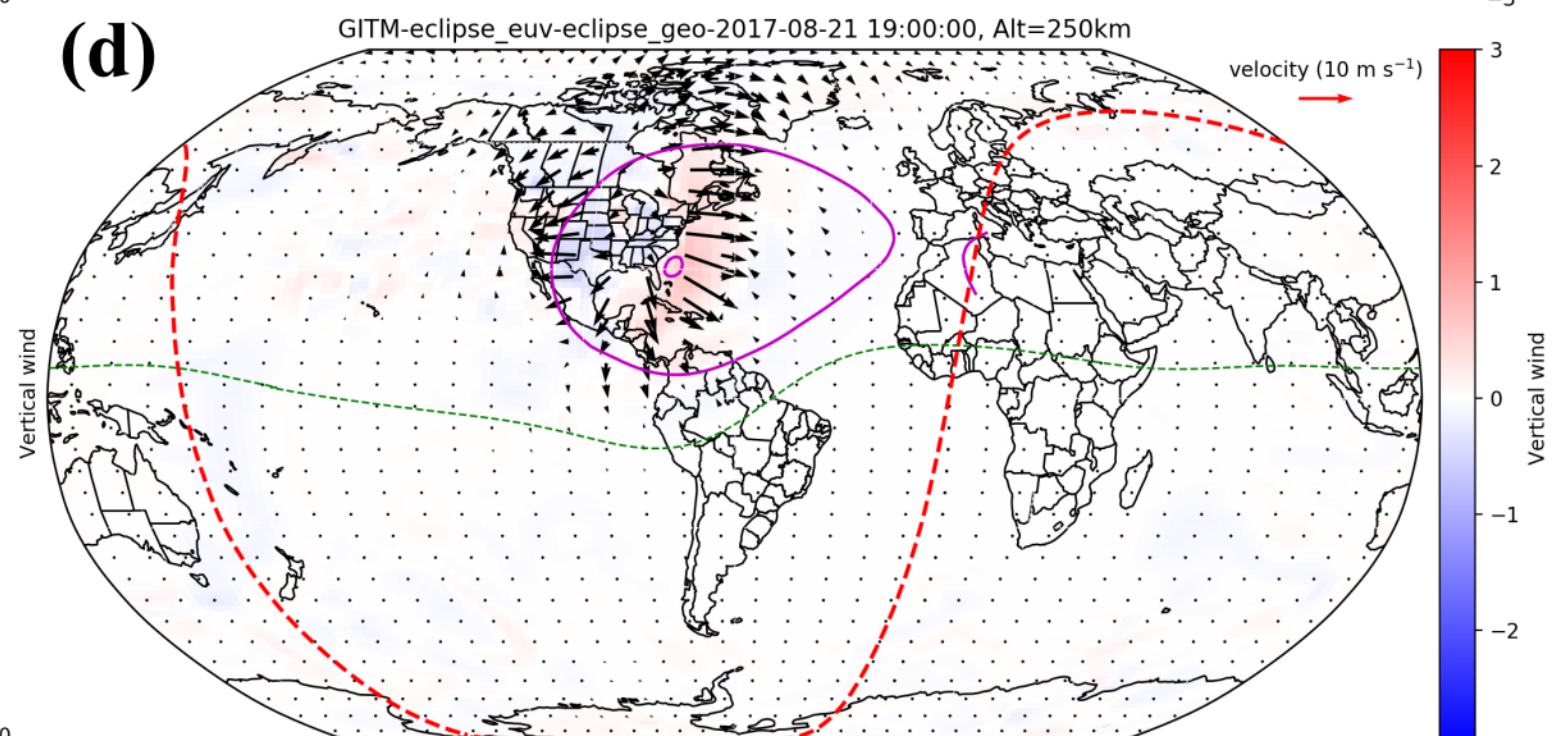
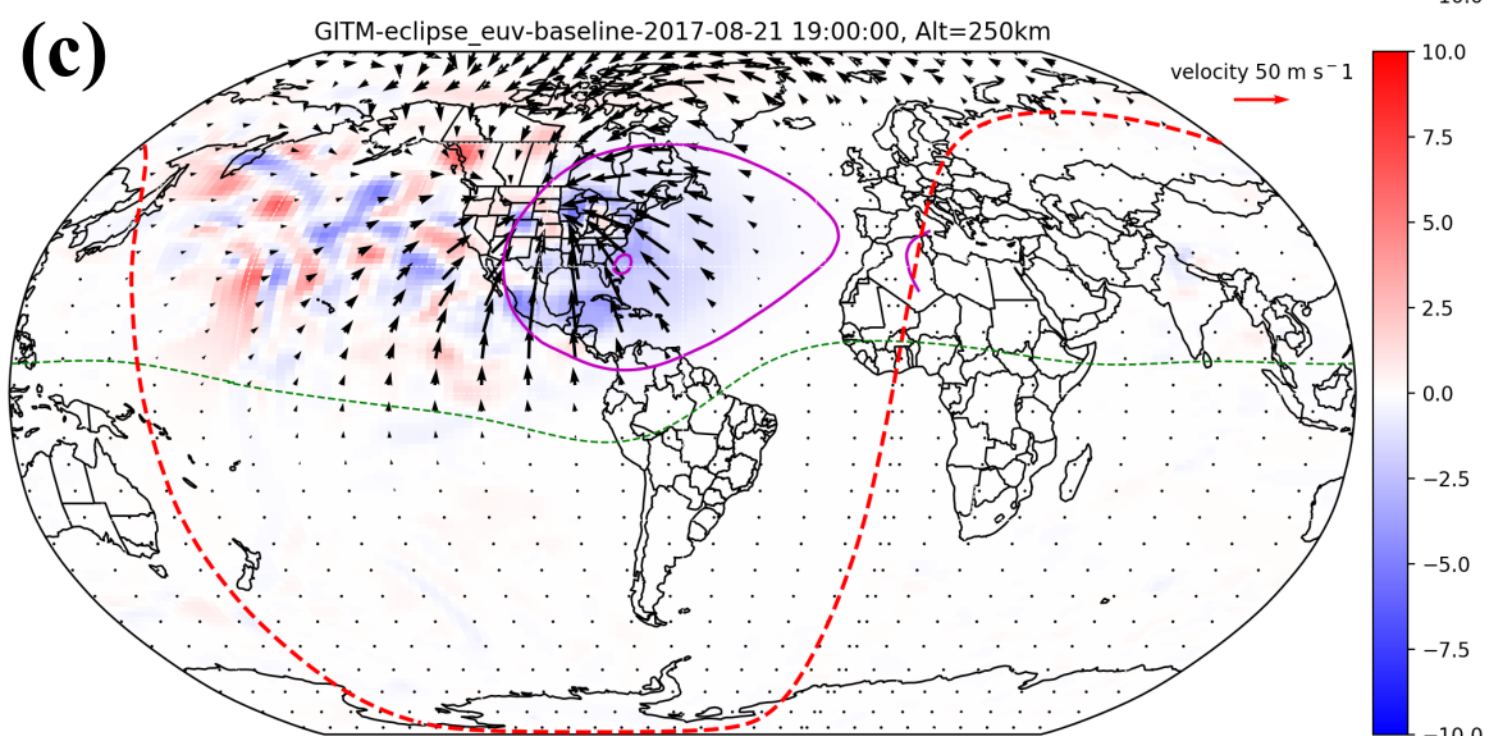
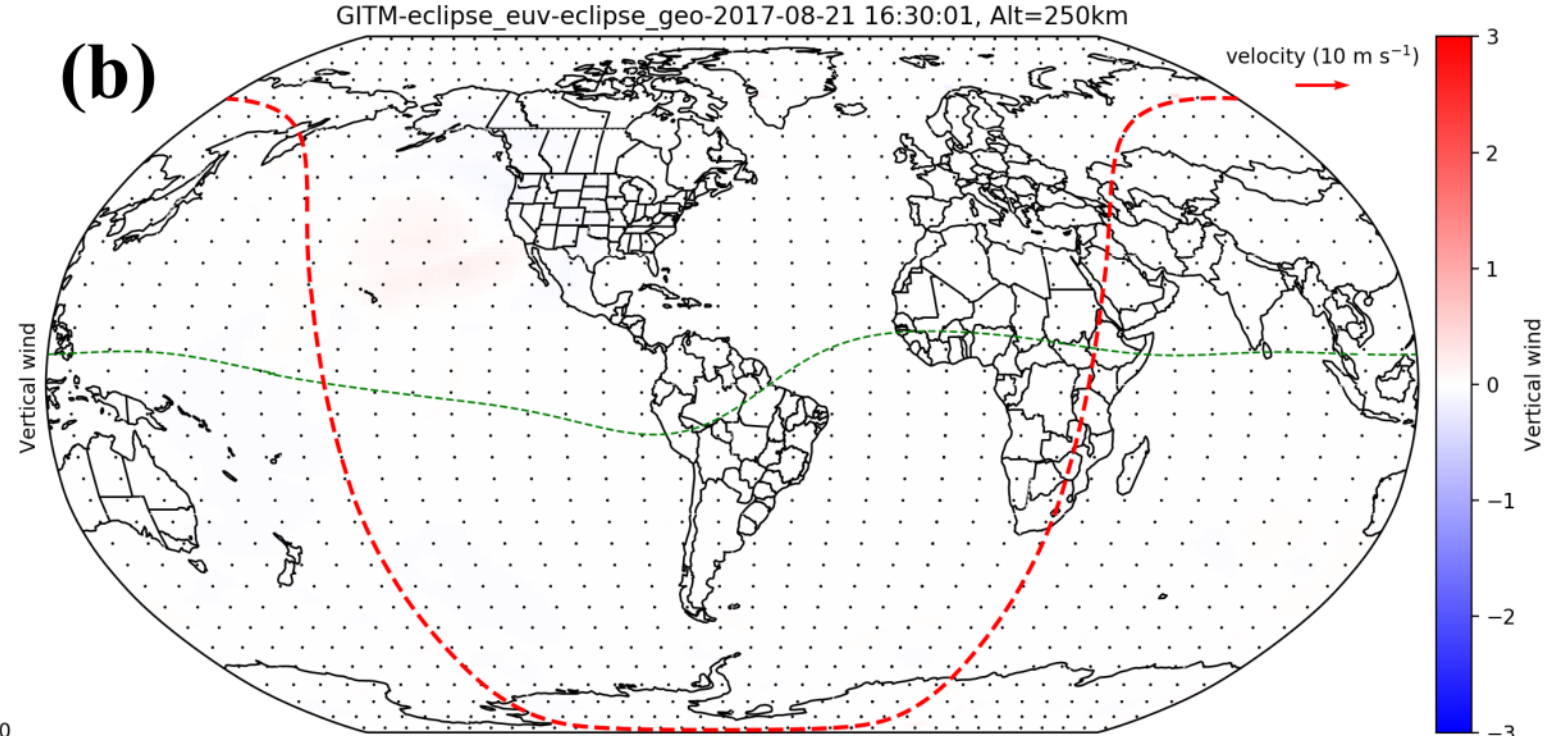
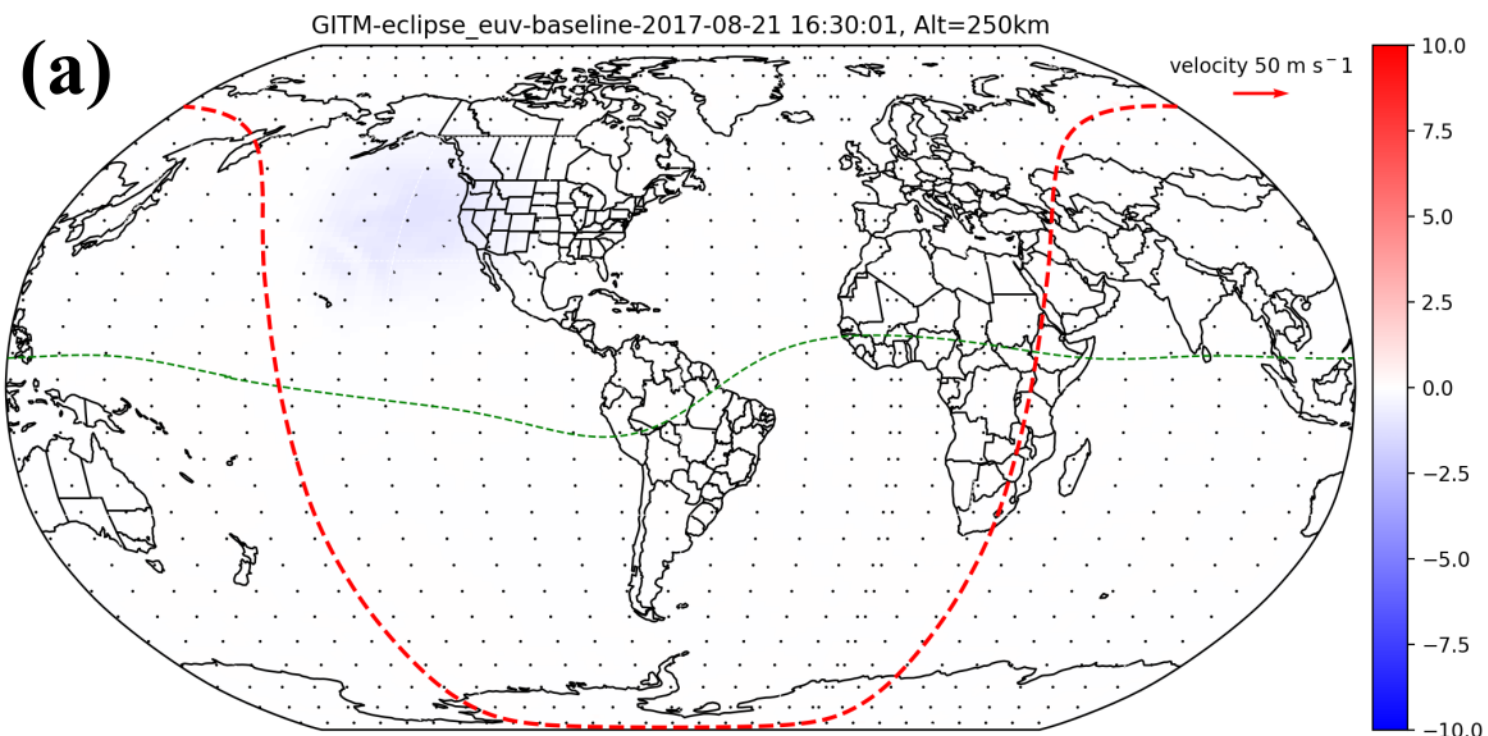


Figure 11.

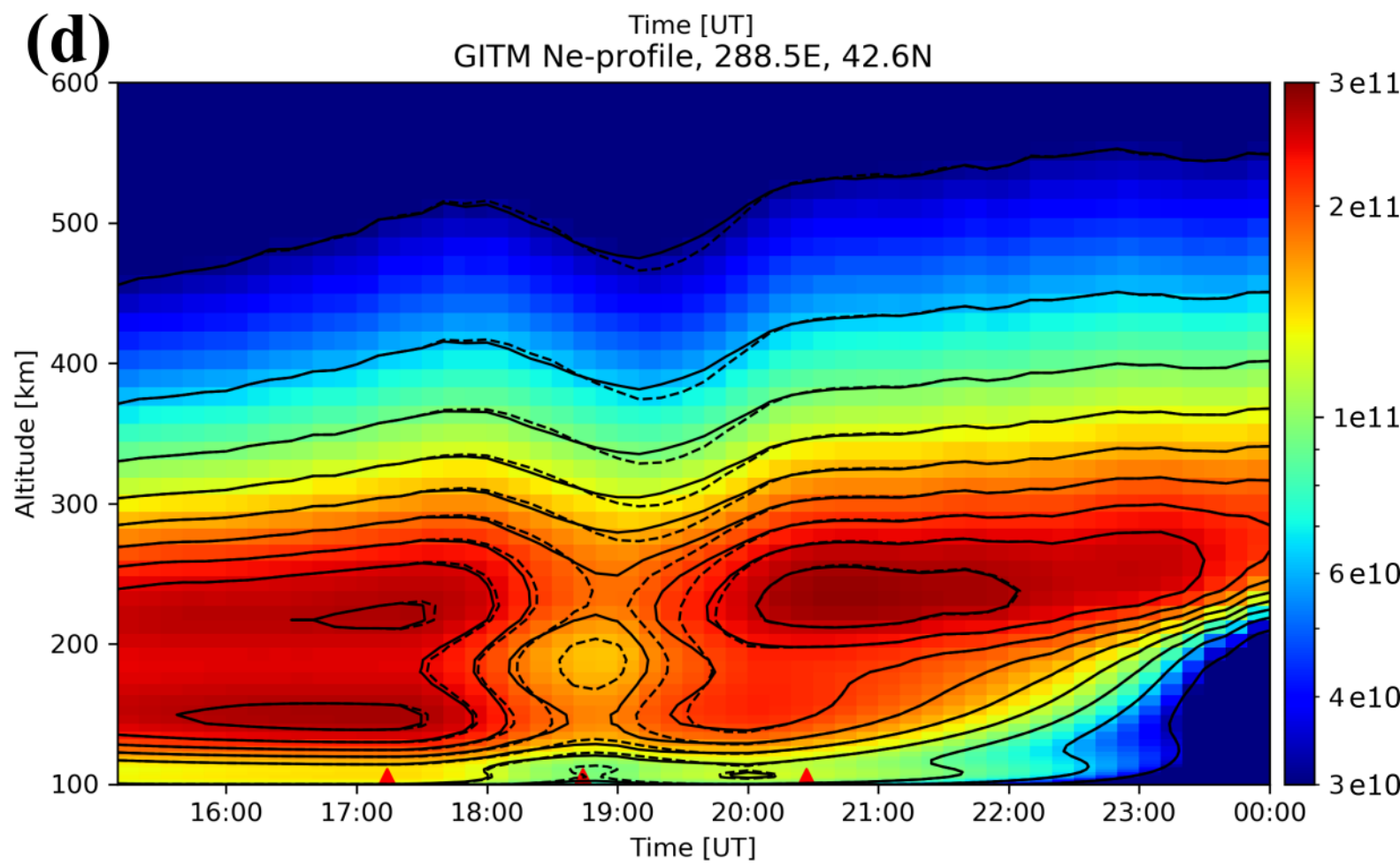
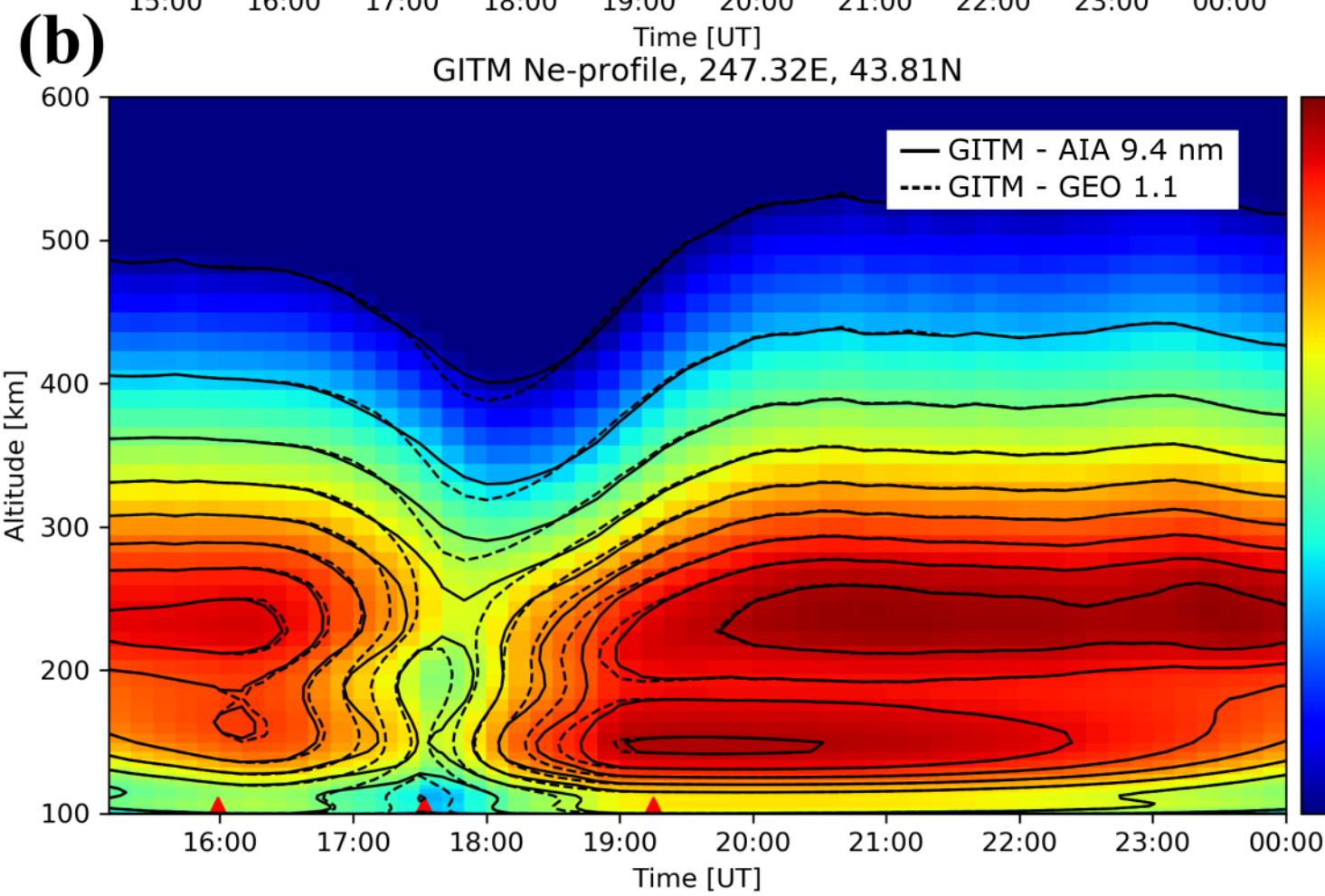
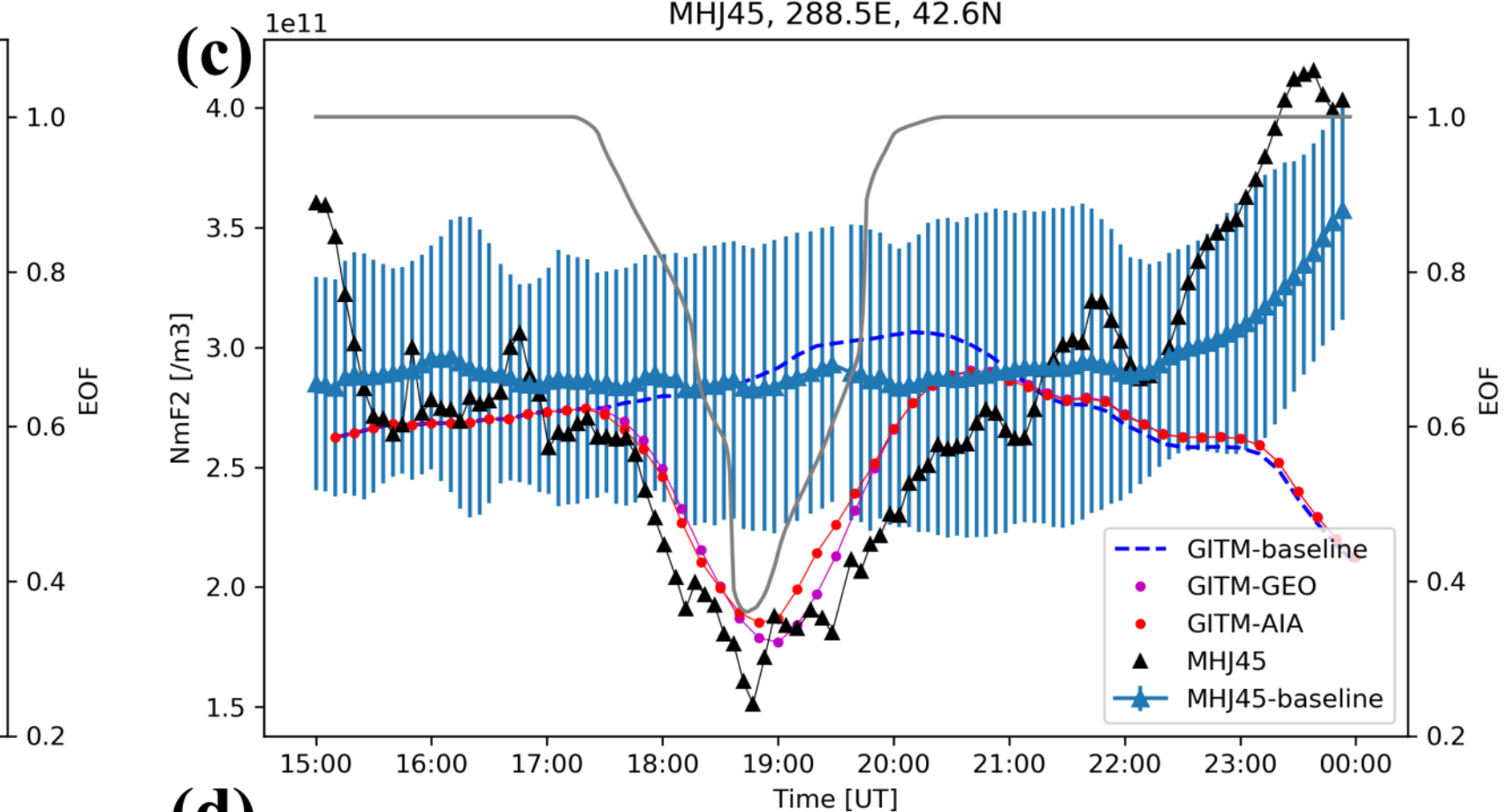
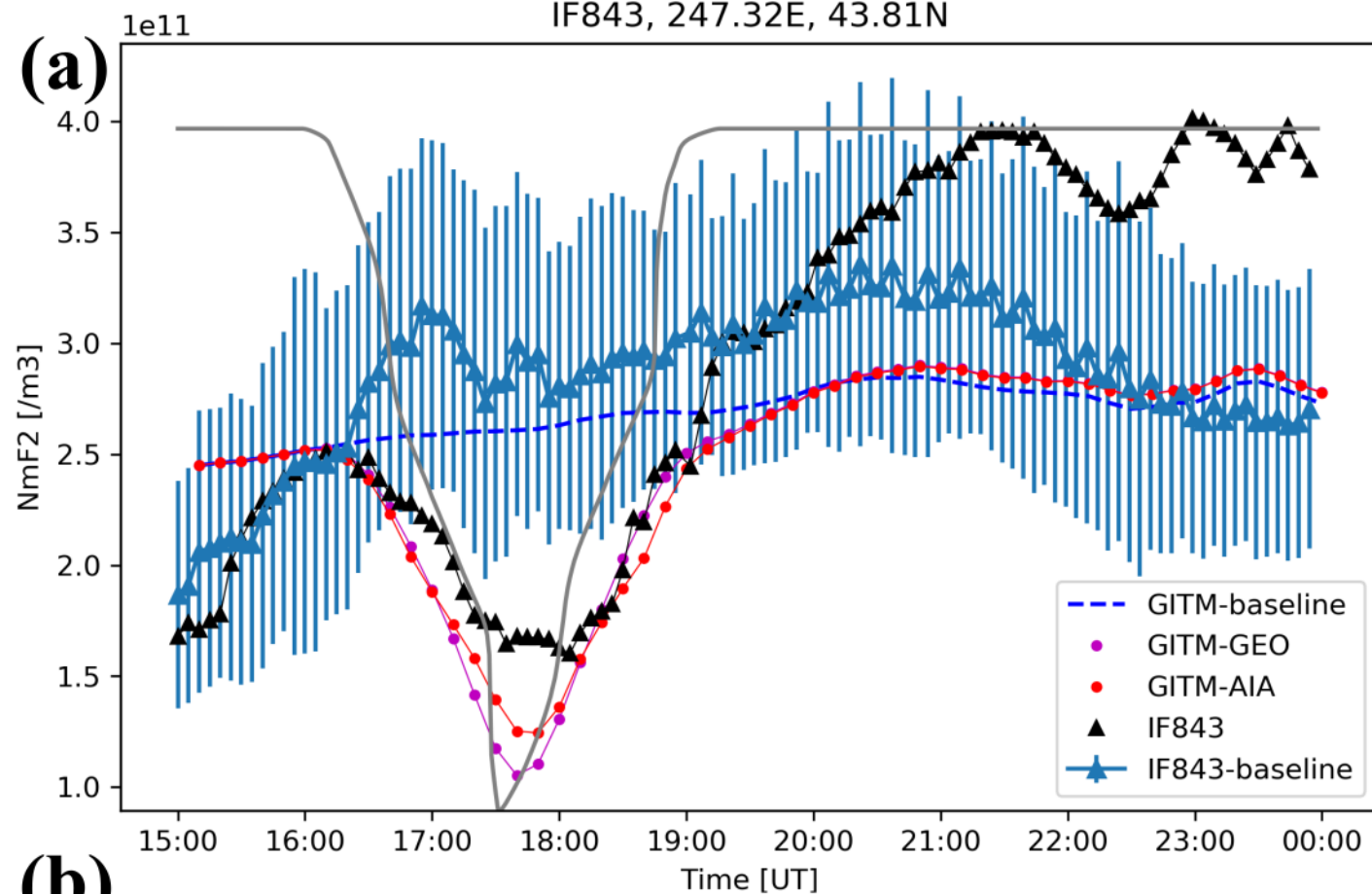
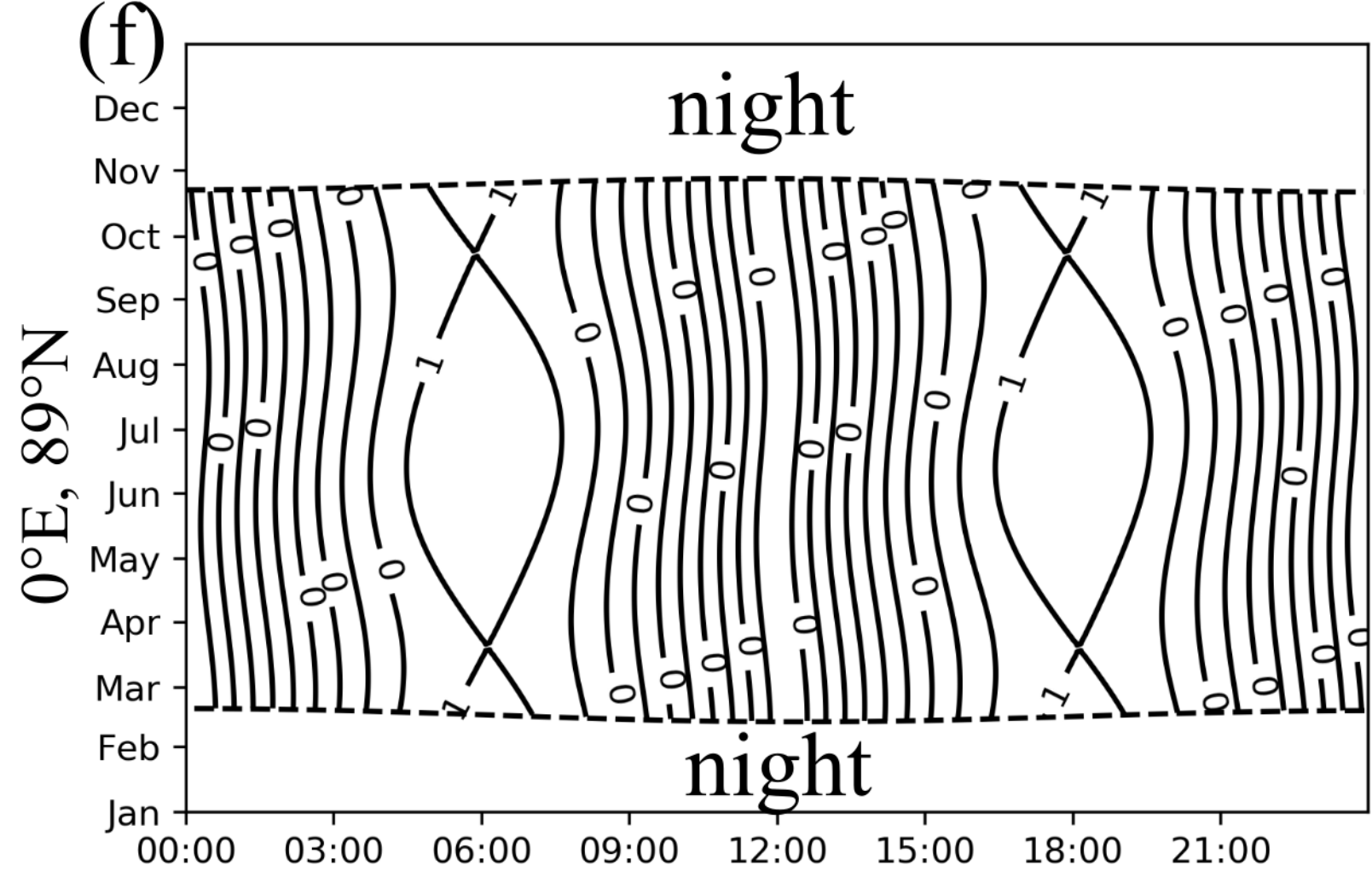
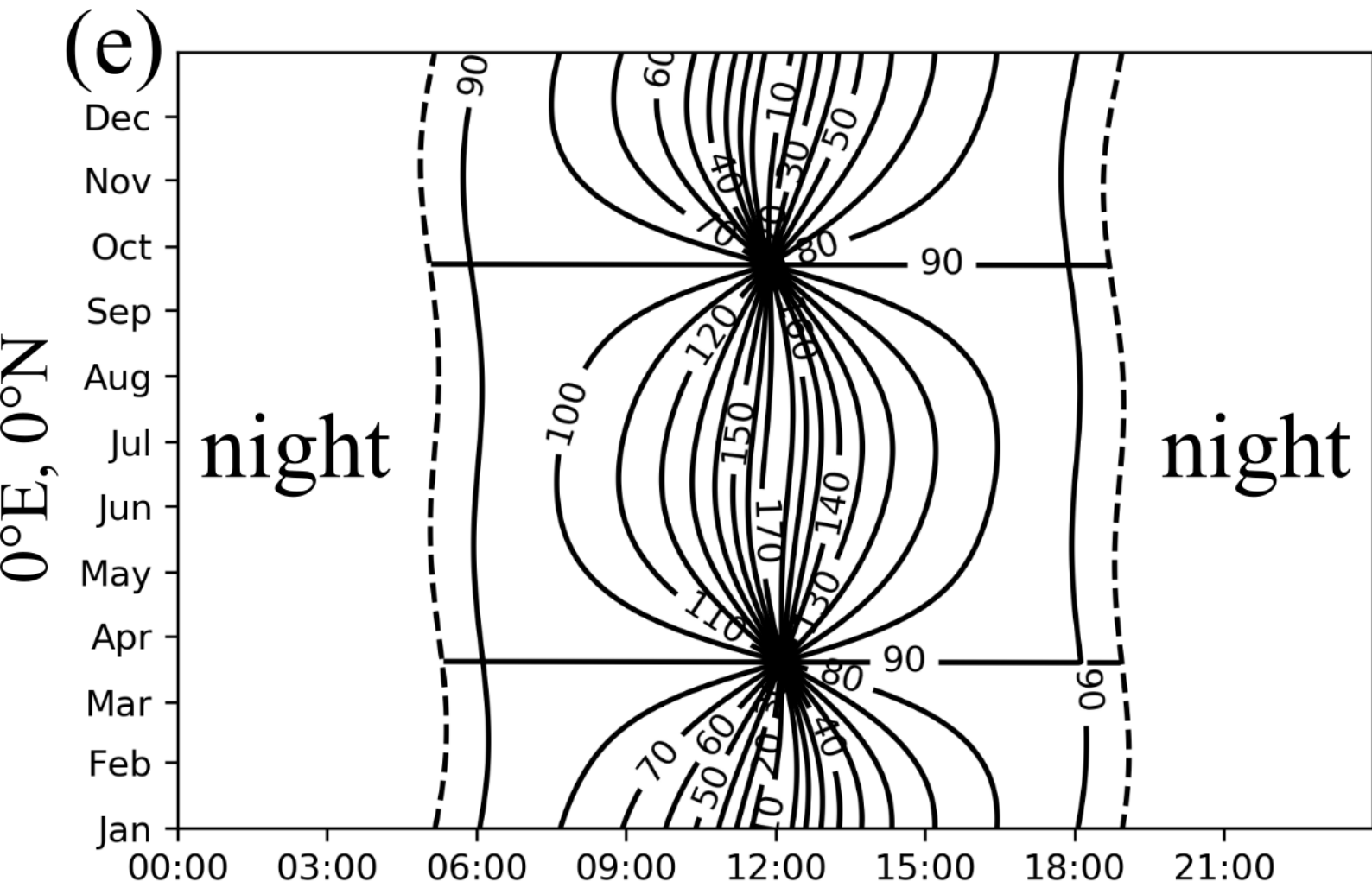
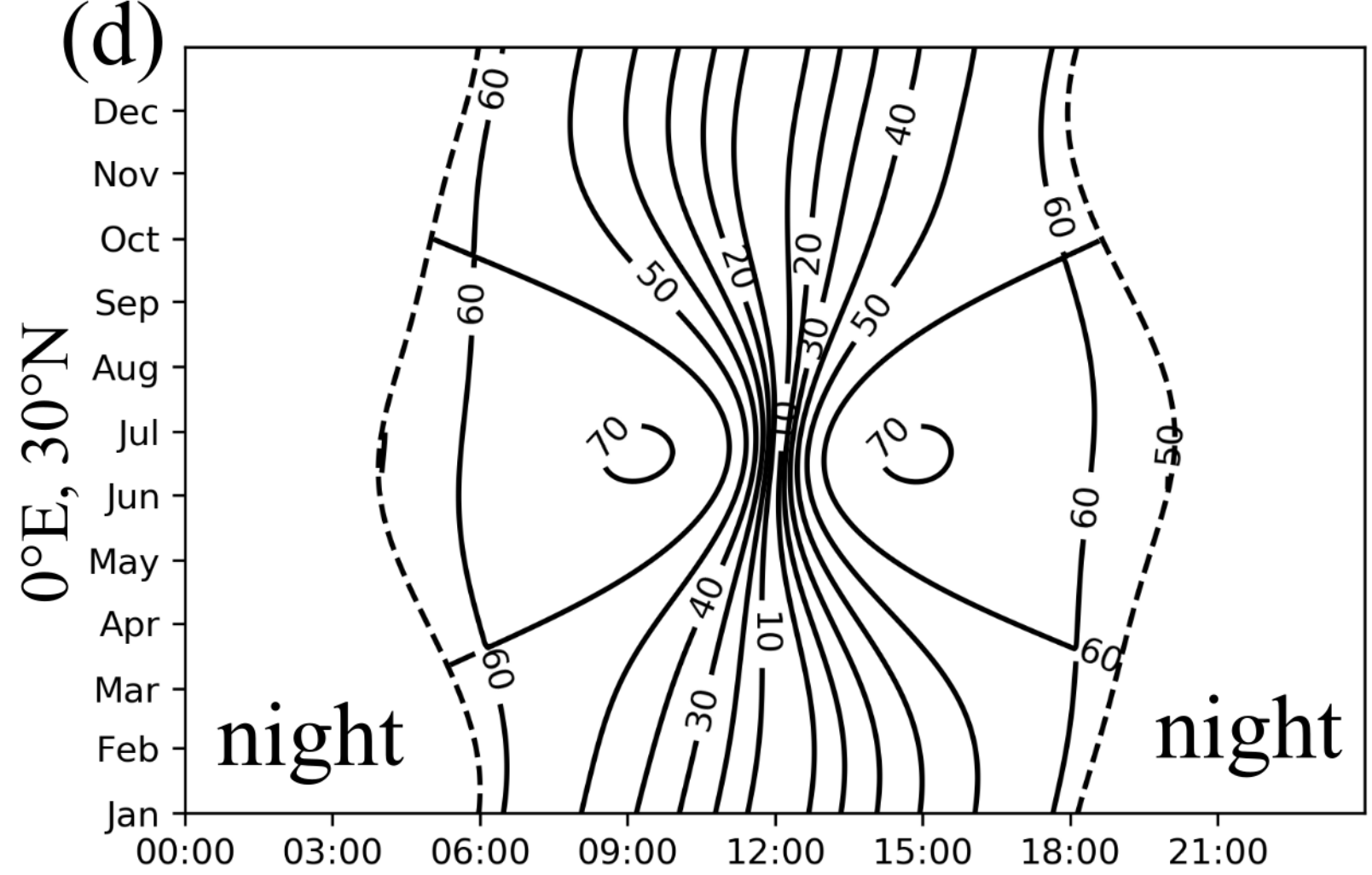
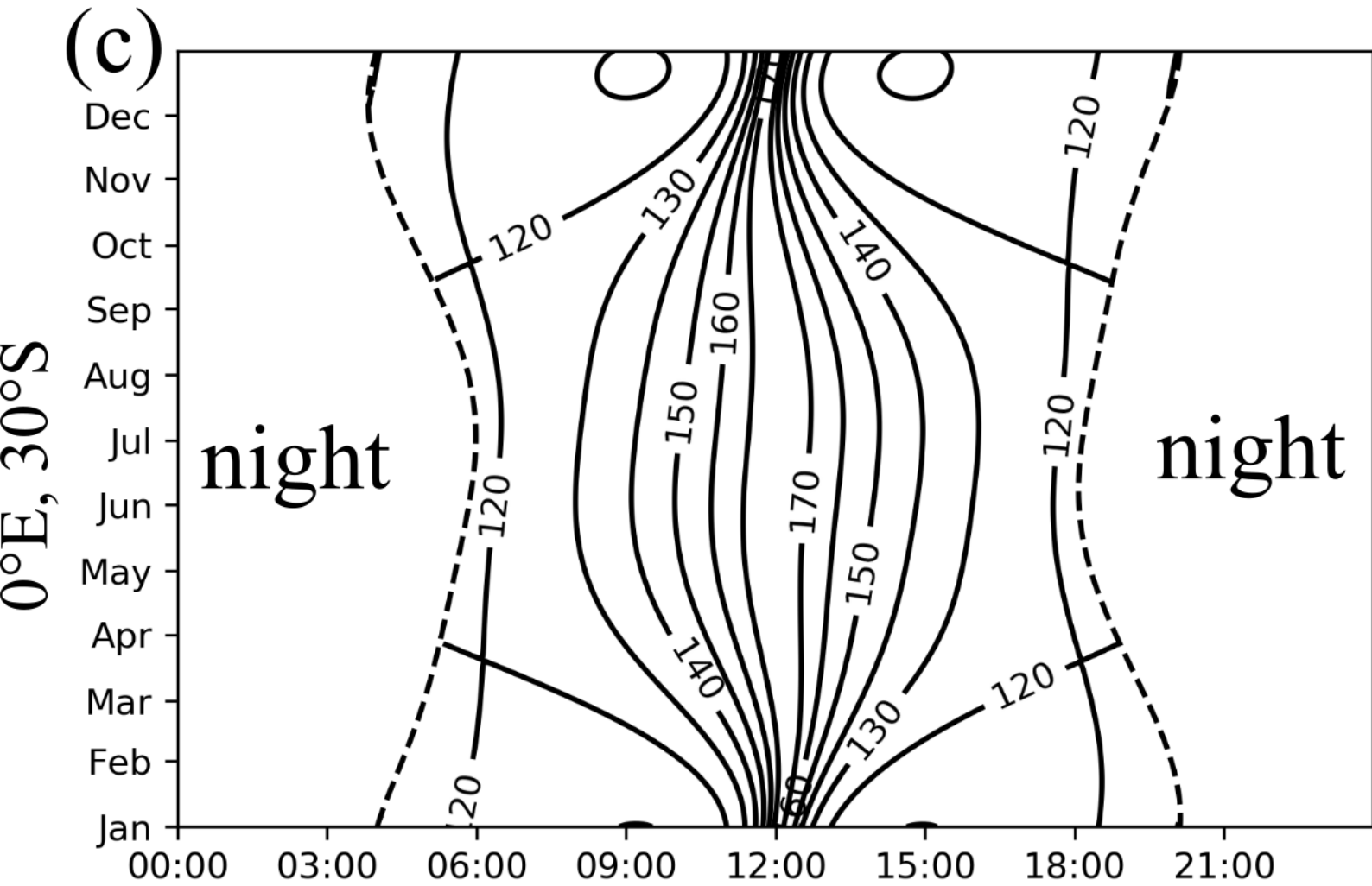
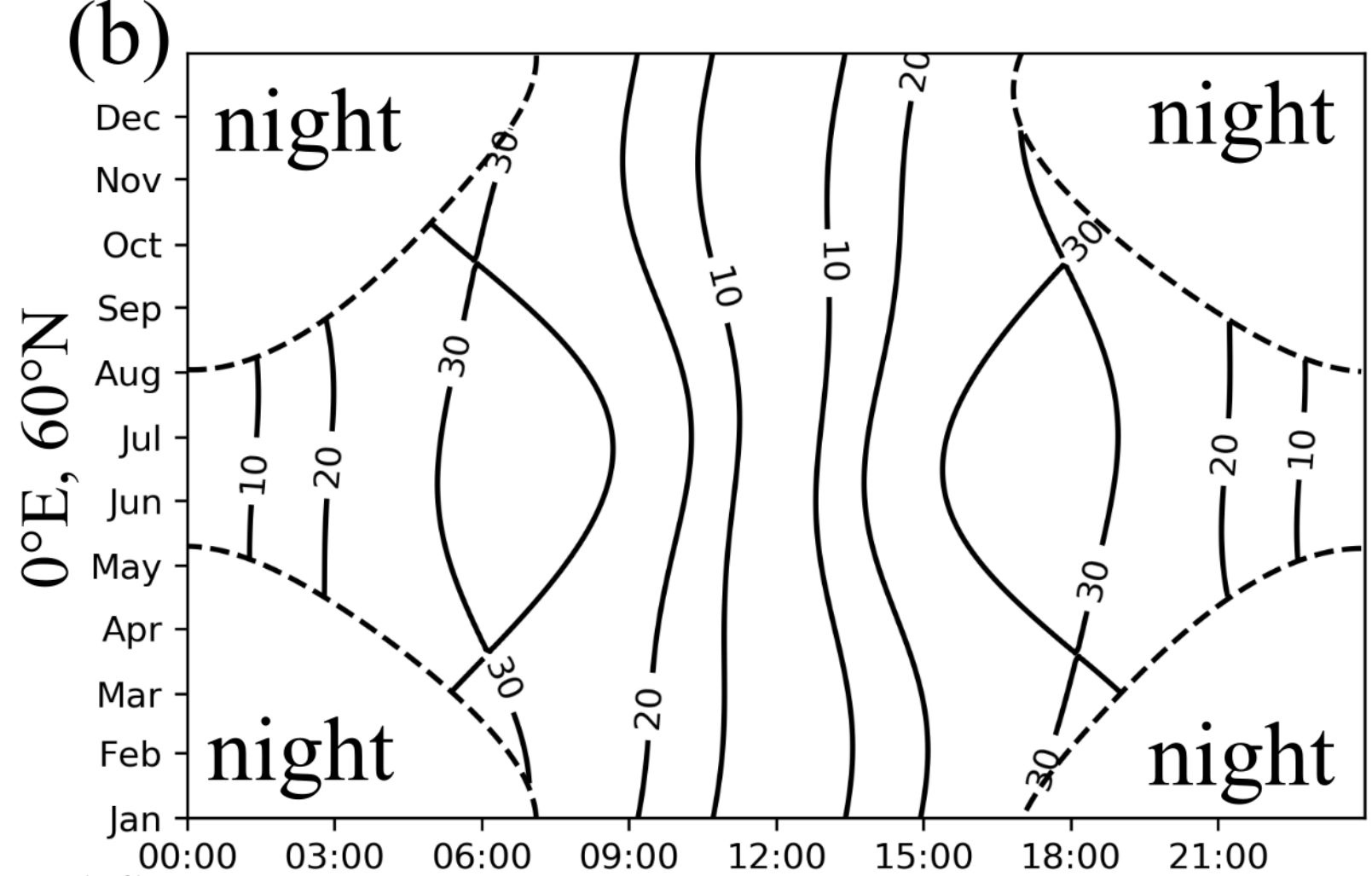
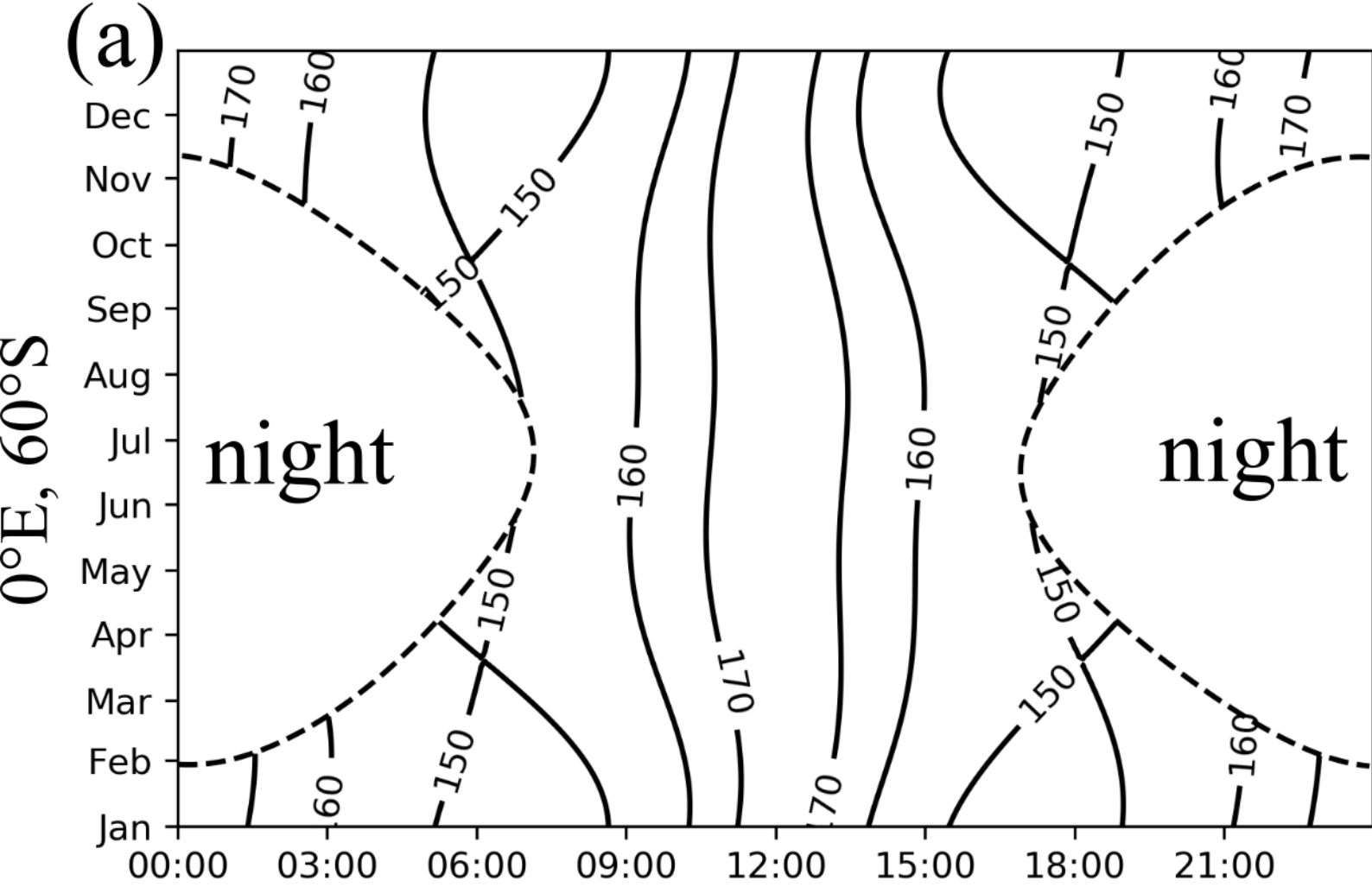


Figure A1.



(Universal) Time in day

(Universal) Time in day

Figure A2.

